TUM School of Natural Sciences

Computational Investigations of the Photocatalytic Reduction of CO_2

Sebastian Pios

Vollständiger Abdruck der von der
TUM School of Natural Sciences der Technischen Universität München
zur Erlangung des akademischen Grades eines
Doktors der Naturwissenschaften (Dr. rer. nat.)
genehmigten Dissertation.

Vorsitz:	Prof. Dr. Klaus Köhler
Prüfer der Dissertation:	Prof. Dr. Wolfgang Domcke
	Prof. Dr. Frank Ortmann

Die Dissertation wurde am 19. Oktober 2022 bei der Technischen Universität München eingereicht und durch die TUM School of Natural Sciences am 15.11.2022 angenommen.

Danksagung

Ich möchte mich hiermit bei Prof. Dr. W. Domcke und seiner Geduld bedanken, mir diese Promotion zu ermöglichen. Seine exzellente Betreuung hat mir geholfen diese nächste Stufe meiner Ausbildung zum Wissenschaftler zu erreichen.Natürlich gilt auch allen weiteren Mitgliedern des Lehrstuhls während meiner Anwesenheit mein Dank für die (fachliche) Unterstützung bei Fragen aller Art.

Selbstverständlich möchte ich auch meinen Eltern danken, welche mich bei meinem Studium immer unterstützen und mich hoffentlich bald als Doktor adressieren dürfen.

Zusätzlich möchte ich auch noch allen meinen Freunden danken, ohne deren Unterstützung ich weder diese Arbeit noch mein Studium so sehr genießen könnte. Vor allem bei Rückschlägen und Problemen hatten sie immer ein offenes Ohr und Verständnis oder eben auch ein hopfenbasiertes Kaltgetränk.

Keine Arbeitsstelle kann ohne eine ordentliche Verwaltung funktionieren. Daher möchte ich mich auch noch bei Ruth Mösch bedanken, die es mir ermöglicht hat sehr viel umständlichen Papierkram zu meiden und immer für eine gute Unterhaltung zur Verfügung stand.

„Every attempt to employ mathematical methods in the study of chemical questions must be considered profoundly irrational and contrary to the spirit of chemistry. If mathematical analysis should ever hold a prominent place in chemistry – an aberration which is happily almost impossible – it would occasion a rapid and widespread degeneration of that science.“

Auguste Comte, 1798-1857

Abstract

In this work, *ab initio* electronic-structure methods were employed to explore novel concepts for the photoinduced conversion of carbon dioxide to the hydroxyformyl (HOCO) radical. The heptazine (Hz) molecule, which is the building block of carbon nitrides (polymeric materials which have been widely employed in recent years as photocatalysts for the water splitting and carbon dioxide reduction reactions), has been chosen as the photocatalytic chromophore. The reduced Hz radical (HzH) is produced (together with OH radicals) by the photoinduced oxidation of water. The reaction of the photoexcited HzH radical with CO_2 has been explored in this work by the computation of reaction paths and their energy profiles in the hydrogen-bonded HzH-CO_2 complex. While the CO_2 reduction reaction in the electronic ground state is notoriously difficult due to a high reaction barrier, the H-atom transfer from photoexcited HzH to CO_2 is found to be nearly barrierless, revealing a novel pathway for activation of CO_2. As alternative to the direct photoreduction of CO_2 with HzH, the water-catalyzed transfer or electrons and protons from the HzH radical to the CO_2 molecule has been explored with *ab initio* computational methods. For these calculations, the aqueous environment was represented by finite-size water clusters. The mechanism of the photoinduced generation of the hydrated electron from reduced Hz species in water clusters was characterized by the computation of the potential-energy surfaces of the relevant electronic states as well as by *ab initio* on-the-fly nonadiabatic molecular dynamics simulations. While the quantum yield of the photoinduced generation of hydrated electrons from reduced Hz is found to be modest, the reduction of CO_2 to the HOCO radical by hydrated electrons in a dark reaction is predicted to be efficient (essentially diffusion limited), in agreement with recent experimental results. While the model systems considered in the present work are highly simplified, the first principles investigation of reaction mechanisms in such model systems with state-of-the-art electronic-structure methods can provide guidelines for the development of novel strategies for the conversion of CO_2 to clean fuels.

Zusammenfassung

In dieser Arbeit wurden *ab initio* Rechenmethoden verwendet, um neue Konzepte für die photoinduzierte Umwandlung von Kohlenstoffdioxid in das Hydroxyformyl (HOCO) Radikal zu erkunden. Als photokatalytischer Chromophor wurde das Heptazin (Hz)-Molekül gewählt, welches der Baustein von Kohlenstoffnitriden (polymere Materialien, die in den letzten Jahren in großem Umfang als Photokatalysatoren für die Wasserspaltung und Kohlenstoffdioxidreduktion eingesetzt wurden) ist. Das reduzierte Hz-Radikal (HzH) wird (zusammen mit OH-Radikalen) durch die photoinduzierte Oxidation von Wasser erzeugt. Die Reaktion des photoangeregten HzH-Radikals mit CO_2 wurde in dieser Arbeit durch die Berechnung der Reaktionswege und ihrer Energieprofile im wasserstoffgebundenen HzH-CO_2-Komplex untersucht. Während die CO_2-Reduktionsreaktion im elektronischen Grundzustand aufgrund einer hohen Reaktionsbarriere bekanntermaßen sehr schwierig ist, erweist sich der H-Atom-Transfer von photoangeregtem HzH zu CO_2 als nahezu barrierefrei, was einen neuen Weg zur Aktivierung von CO_2 aufzeigt. Als Alternative zur direkten Photoreduktion von CO_2 mit HzH wurde der wasser-katalysierte Transfer von Elektronen und Protonen vom HzH-Radikal auf das CO_2-Molekül mit *ab initio* Rechenmethoden untersucht. Für diese Berechnungen wurde die wässrige Umgebung durch Wassercluster in endlicher Größe angenähert. Der Mechanismus der photoinduzierten Erzeugung des hydratisierten Elektrons aus reduzierten Hz-Spezies in Wasserclustern wurde durch die Berechnung der Potentialhyperfläche der relevanten elektronischen Zustände sowie durch *ab initio* „on-the-fly“ nichtadiabatische Molekulardynamikssimulationen charakterisiert. Während die Quantenausbeute der photoinduzierten Erzeugung von hydratisierten Elektronen aus reduziertem Hz bescheiden ist, wird die Reduktion von CO_2 zum HOCO-Radikal durch hydratisierte Elektronen in einer Dunkelreaktion als effizient (im Wesentlichen diffusionsbegrenzt) vorhergesagt, was mit jüngsten experimentellen Ergebnissen übereinstimmt. Obwohl die in dieser Arbeit betrachteten Modellsysteme stark vereinfacht sind, kann die Untersuchung der Reaktionsmechanismen in solchen Modellsystemen mit modernen „first principles“ Rechenmethoden Leitlinien für die Entwicklung neuartiger Strategien für die Umwandlung von CO_2 in saubere Kraftstoffe liefern.

Contents

1 Introduction

Evergrowing demand of fossil fuels has increased the interest in and need of renewable energies and the research on closed carbon cycles.[1–3] Examples of closed carbon cycles are CO_2-formic acid and CO_2-methanol couples. Although closed carbon cycles are already technologically possible, the required transformations to substances like formic acid or methanol are very energy-demanding.[4, 5] Multiple concepts have been investigated over the past decades to overcome these challenges. Examples of concepts are discussed below.

The most simplistic approach to CO_2 reduction are hydrogenation reactions.[6–8] Here, CO_2 is brought to reaction with H_2 to form CO, methanol or formic acid. The reaction of CO_2 with H_2 to CO and H_2O is known as the water gas shift reaction and has been known for over 200 years.[9] The formed CO can then further be used in the Fischer-Tropsch process to form different alkanes.[10] Copper-based catalysts have been of large interest for these reactions as they exhibit selectivity and efficiency towards CO_2 hydrogenation.[4, 11] Leitner and coworkers reported a rhodium-based catalyst with close to 100% selectivity towards formic acid formation.[12] Ethanol formation also has been reported, although with low selectivity.[13] For the formation of higher hydrocarbons, hybrid catalysts and zeolites are commonly used.[4] Noyori and coworkers also investigated these reactions in supercritical CO_2 and found high efficiencies and formation of dimethylformamide.[14] Rather than synthesising hydrocarbons from just CO_2 and H_2, CO_2 is also used in the industrial synthesis of chemicals like urea, salicylic acid and cyclic carbonates. Most of the time, the CO_2 is inserted into an X-H bond (X=C, N...) with the difference being the extent to which CO_2 is reduced. Transition-metal based catalysts are commonly used for this purpose.[4]

The electrochemical reduction of CO_2 utilizing different metal electrodes also has attracted increasing attention in the past decades.[15–17] Copper electrodes have been found to reduce CO_2 to methane with an efficiency of 65%.[18] Remarkably, the evolution of CO from CO_2 has been reported to be observed rather than the thermodynamically favored hydrogen evolution reaction.[19, 20] In general, bulk metal electrodes can be categorized into multiple groups with respect to the main reaction product. Copper can be used to form hydorcarbons and alcohols. Gold, silver, zinc, palladium and gallium can be used to form carbon monoxide and lead, mercury, indium, tin, bismut, cadmium and tellurium for the formation of formic acid.[21, 22] The application of transition-metal complexes as catalysts allows for an increased selectivity with respect to the reaction product and results in lower operating potentials. These catalysts have the drawback of decreased stability with respect to bulk cathodes. The use of pyridine as a catalyst for the CO_2 reduction reaction at different bulk electrodes has been studied extensively theoretically[23–25]

and experimentally[26–30]. Hydride anions are also capable of reducing CO_2 to form HCO_2^- (deprotonated formic acid).[31, 32] In this reaction, two electrons and one proton are transferred to the CO_2 molecule at mild potentials.

The photocatalytic CO_2 reduction using heterogenous catalysts and water to generate solar fuels has recieved a lot of attention, see [33–41] and references therein. The goal is to mimic photosynthesis and produce high value chemicals from CO_2 in a sustainable manner. In 1978, the photoelectric reduction of CO_2 on p-type gallium phosphide was first resported.[42] One year later, Inoue *et al.* reported the photoelectric reduction of CO_2 using a number of different semiconductors.[43] These two publications mark the start of publications in this area, the number of which increases each year. Ruthenium based compounds (e.g. Ru(2,2′-bipyridine)$_3^{2+}$) can be named as examples of photosensitizers and catalysts which can fulfill multiple roles in the reaction.[34] Besides the vast number of possible photocatalysts, each one can be modified with respect to the energy band-gap, cocatalysts (e.g. platinum) and surface defects in order to increase activity and selectivity. Similarly to the case of electrochemical CO_2 reduction, the hydrogen evolution reaction competes with the CO_2 reduction reaction, posing an additional challenge. In more recent studies, organic materials like polymeric carbon nitrides (PCNs)[44, 45] with TM complexes as co-catalysts were found to promote the photoinduced reduction of CO_2 to CO or formate in the presence of sacrifical electron donors.[46–50]

In 2014, Hamers and coworkers reported a different approach to CO_2 reduction, the photoelectrochemical reduction of aqueous CO_2 to CO by solvated electrons.[51] In this study, diamonds were irradiated with UV light to emit electrons into water.[51] A remarkable result of this study was the reaction's high selectivity of 90% with minimal H_2 formation.

Hydrated electrons are metastable defects in liquid water, which are generated by ionizing radiation or by the photodetachment of electrons from anions.[52–57] The hydrated electron is defined by its characteristc intense and broad absorption spectrum which peaks at 720 nm.[52] At room temperature, its lifetime is about 1 μs in ultrapure water.[53] Its reduction potential of 2.9 eV is one of the highest in chemistry.[54] The atomistic structure of the hydrated electron has been the subject of intense debates since decades and is still not definitely clarified.[58–65] The mainstream opinion currently favors the cavity model, in which a localized electron cloud is confined in a cavity within the hydrogen bonded network of water molecules.[56–58, 63, 66, 67] Alternatives to this model, with a more molecular touch like a H_3O–OH^- complex, have been proposed by Robinson and coworkers[68] and Tuttle and Golden.[69] More recently, the hydrated hydronium model, $H_3O(H_2O)_n$, of the solvated electron has been proposed based on *ab initio* calculations for finite-size clusters.[70, 71] It was observed that the hydrated H_3O radical's absorption spectra converge to the characteristic absorption spectrum of the hydrated electron with increasing clus-

ter size.[70] As these clusters undergo spontaneous charge separation resulting in a H_3O^+ cation loosely bonded with a solvated electron cloud, this model is not fundamentally different from the traditional cavity model.[57, 70, 71] Additionally, recent studies of hydrated electron formation in water clusters using XUV-induced radiolysis provided strong evidence for the hydrated hydronium model.[72] In the present work, the hydrated hydronium model is invoked as a finite size model for the hydrated electron.

In 2017, Domcke and coworkers proposed a mechanism for water oxidation and hydrogen evolution with heptazine (Hz).[73] Hz is the building block of PCNs.[44, 45] It has been predicted by *ab initio* calculations that Hz photoexcited to the bright $^1\pi\pi^*$ state can abstract a hydrogen atom from water in $Hz\cdots(H_2O)_n$ complexes (the dots denote a hydrogen bond) via a proton coupled electron transfer (PCET) reaction, yielding heptazinyl (HzH) and OH radicals.[73] The corresponding reaction is shown in Eq. 1.

$$Hz + (H_2O)_n \xrightarrow{h\nu} HzH + OH(H_2O)_{n-1} \tag{1}$$

The formation of OH radicals was confirmed experimentally with a chemically stable derivative of Hz, trianisole-heptazine (TAHz), in aqueous solution[74] which indirectly confirms the formation of the TAHzH radical. Recently, the formation of the TAHzH radical has also been reported.[75] Calculations predict that the low-lying bound $^2\pi\pi^*$ states of the HzH radical are predissociated by $^2\pi\sigma^*$ states which are repulsive with respect to the NH bond length, like in the pyridinyl (PyH) and pyrimidinyl (PmH) radicals.[76, 77] The excess H atom may be transferred to a suitable acceptor with an additional photon. The absorption spectra of Hz as well as of the HzH radical can be tuned into the visible by suitable substituents.[78] Taken together, the theoretical results for the water-oxidation processes by Domcke and coworkers and the experimental results for the CO_2 reduction process by Maeda and coworkers suggest that the combination of photoinduced HzH formation from water with the photoreduction of CO_2 may be a mechanism for the generation of liquid fuels directly from CO_2 and water using Hz as a photocatalyst.

Using the HzH radical generated in the water-splitting cycle with photons to transfer a hydrogen atom in a photoinduced PCET reaction from HzH to CO_2 in a hydrogen-bonded $HzH\cdots OCO$ complex, thus reducing CO_2 to HOCO, is the first approach taken in this work. This way the Hz molecule is recoverd and can be fed back into the water-splitting cycle. This direct mechanism of the reduction of CO_2 is investigated in a static computational study in Section **3**. The reaction mechanism is described by Eq. 1 and Eq. 2.

$$HzH + CO_2 \xrightarrow{h\nu} Hz + HOCO \tag{2}$$

As the solubility of CO_2 in water under ambient conditions is low[79], the concentration of $HzH\cdots OCO$ complexes may be low. The concentration of $HzH\cdots(H_2O)_n$ clusters is likely much higher. In $HzH\cdots(H_2O)_n$ clusters, a photon can induce a PCET reaction from the HzH radical to the hydrogen-bonded water cluster, forming $H_3O(H_2O)_{n\text{-}1}$ radicals. This reaction is summarized in Eq. 3.

$$HzH + (H_2O)_n \xrightarrow{h\nu} Hz + H_3O(H_2O)_{n-1} \tag{3}$$

As discussed above, the $H_3O(H_2O)_n$ cluster is considered as a finite-size model for the hydrated electron. Again, the Hz molecule is recovered by the formation of $H_3O(H_2O)_n$ radicals and can be fed back to the water-splitting cycle. A static computational study of the $HzH\cdots(H_2O)_n$ complexes (n=0,1,4) is presented in Section **4**.

The ground-state reaction of $H_3O(H_2O)_n$ clusters (n=0,3,6) with a CO_2 molecule is investigated in a static computational study in Section **5**. This may give additional insight into the mechanism as the experimental focus was mainly on the yield of the reaction. Eq. 4 depicts the reaction equation.

$$H_3O(H_2O)_{n-1} + CO_2 \rightarrow HOCO + (H_2O)_n \tag{4}$$

In contrast to the previous two reactions, no photons are involved in this reaction. The reaction products are water-clusters and HOCO.

Finally, a nonadiabatic excited state dynamics study of the $HzH_2\cdots(H_2O)_4$ complex has been performed to evaluate the quantum yield and the timescale of the formation of $H_3O(H_2O)_3$ radicals. This study is described in Section **6**.

A short introduction can be found at the beginning of each section. The sequence of these reactions, in combination with the water-splitting cycle, uses H atoms from water to reduce CO_2 either directly (in the $HzH\cdots OCO$ complex) or indirectly (via $H_3O(H_2O)_n$ radicals). A sucessfull experimental realization of these reactions would open a new pathway of combining the water-splitting cycle with solar photons with the reduction of CO_2 to generate solar fuels, thus closing the carbon cycle.

Unlike many computational studies in this field, the present study of these reactions focusses on finite-size molecular complexes rather than on condensed-phase systems with perodic boundary conditions. This allows the use of high-level electronic-structure methods which are not applicable for very large systems. The drawback of this approach is the lack of description of solvation effects.

2 Theoretical Background

2.1 Electronic-Structure Methods

2.1.1 Hartree-Fock Approximation

Since its formulation dating back as far as the 1920s, the Hartree-Fock (HF) approximation has been one of the cornerstones of *ab initio* methods used to describe quantum chemical problems.[80–82] In this approximation, the common, and often sufficient, picture of electrons occupying orbitals is used.[83] Although it became uncommon to use results from HF theory in modern publications, HF theory forms the basis for a manifold of semi-empirical and *ab initio* methods like the Møller-Plesset perturbation theory as discussed in Section **2.1.2** and the complete-active-space self-consistent-field (CASSCF) method as discussed in Section **2.1.4**.
The Hartree-Fock equation is

$$f(1)\chi_a(1) = \left[h(1) + \sum_b J_b(1) - K_b(1)\right]\chi_a(1) = \epsilon_a\chi_a(1). \tag{5}$$

The operator *h* describes the kinetic energy of one electron in the field of the bare nuclei. The other two operators are called Coulomb (J_b) and exchange (K_b) operators. The Coulomb operator describes the averaged potential of *N-1* electrons acting on the electron in orbital χ_a. The Coulomb operator is uniquely defined for each point in space and therefore a local operator. The exchange operator arises from the antisymmetric nature of the determinant and has no classical counterpart. Unlike the Coulomb operator, the exchange operator is not uniquely defined for each point in space as it depends on the orbital χ_a and is therefore a non-local operator.
According to Koopman's theorem, the orbital energies ϵ_a can be interpreted as ionization potentials or electron affinities of the respective orbitals depending on the occupancy.[84]
The Roothaan-Hall equations (also commonly referred to as Roothaan equations) in combination with the iterative self-consistent-field (SCF) approach reduce the solution of the eigenvalue problem of the HF equations for closed-shell systems, i.e. all electrons are paired, to a linear algebra problem.[85, 86] The orbital χ_i is represented as a linear expansion of *K* atomic basis functions $\phi_\mu(\mathbf{r})$ with coefficients $C_{\mu i}$. Using this, the Fock matrix **F** and the overlap matrix **S** are given by:

$$F_{\mu\nu} = \int d\mathbf{r}_1 \phi_\mu^*(1) f(1) \phi_\nu(1) \tag{6}$$

$$S_{\mu\nu} = \int d\mathbf{r}_1 \phi_\mu^*(1) \phi_\nu(1). \tag{7}$$

The Roothaan equations are given in matrix form as:

$$\mathbf{FC} = \mathbf{SC}\epsilon. \tag{8}$$

A set of orthonormal spin orbitals $\{\chi_a\}$ is sought to form a single determinant Ψ_0, which minimizes the energy E_0 of the electronic ground-state of an *N*-electron system. The energy E_0 is defined as:

$$E_0 = \langle\Psi_0|H|\Psi_0\rangle = \sum_a \langle a|h|a\rangle + \frac{1}{2}\sum_{ab}\langle ab||ab\rangle = \sum_a \underbrace{\langle a|h|a\rangle}_{\mathsf{h}} + \frac{1}{2}\sum_{ab}\underbrace{[aa|bb]}_{J_{b\chi_a}} - \underbrace{[ab|ba]}_{K_{b\chi_a}}. \tag{9}$$

The integrals $\langle aa|bb\rangle$ and $\langle ab|ba\rangle$ in Eq. 9 are the Coulomb and exchange integrals, respectively. Their definitons are:

$$\langle\chi_a(1)|J_b(1)|\chi_a(1)\rangle = \int dx_1 dx_2 \chi_a^*(1)\chi_a(1) r_{12}^{-1}\chi_b^*(2)\chi_b(2) = [aa|bb] \tag{10}$$

$$\langle\chi_a(1)|K_b(1)|\chi_a(1)\rangle = \int dx_1 dx_2 \chi_a^*(1)\chi_b(1) r_{12}^{-1}\chi_b^*(2)\chi_a(2) = [ab|ba]\,. \tag{11}$$

The above derivations are valid for closed-shell systems and correspond to the restricted HF (RHF) theory. For open-shell systems, i. e. systems with unpaired electrons, the formalism has to be extended. While in RHF theory the orbital χ_a describes a spatial orbital for both α and β spin, this restriction is lifted in unrestricted HF (UHF) theory. Therefore a orbital χ_a is replaced by spin orbitals ψ_a^α and ψ_a^β, which do not have to have the same spatial functions. Inserting these spin orbitals in the equations above leads to the respective unrestriced formalism, the Pople-Nesbet equations, which are the unrestricted equivalent to the Roothaan-Hall equations.[87]
While recovering most of the energy of the electronic system, by construction, HF theory does not describe electron correlation effects. Electron correlation can be treated using perturbation theory as described in Section **2.1.2**. So-called static correlation can be treated using a multireference approach as described in Section **2.1.4**.

2.1.2 Møller-Plesset Perturbation Theory

Perturbation theory can be used to recover the electronic correlation energy. In perturbation theory, the problem is divided into a unperturbed part and a small perturbation. In Møller-Plesset perturbation theory to *n*-th order (MP*n*), the unperturbed Hamiltonian is the sum of Fock operators. As is apparent from Eq. 5, this leads to counting the electron-electron repulsion $\langle V_{ee}\rangle$ twice.

Therefore, the perturbation is the operator for the electron-electron interaction (V_{ee}) minus twice the average electron-electron repulsion ($\langle V_{ee} \rangle$)

$$H' = H - H_0 = V_{ee} - 2\langle V_{ee} \rangle. \tag{12}$$

Contrary to the assumption of perturbation theory, this perturbation is not necessarily small, demanding caution in the application of perturbation theory. Combining the zeroth order energy, which is the sum of the energies of all occupied orbitals, and the first order energy of MP*n* perturbation theory, which is the expectation value of the two-electron part of the Fock operator, the Fock energy is obtained. Dynamic correlation is recovered in higher order treatments starting at the second order. This is done by evaluating the matrix elements of H' between the HF wave-function and all possible excited states. Excited state wave-functions are constructed by exciting electrons from occupied orbitals (i,j,...) to virtual orbitals (a,b,...). Due to Brillouin's theorem matrix elements with singly excited states vanish.[88] Furthermore, matrix elements with more than two excitations vanish as well because the perturbation operator is a two-particle operator. An overview of the contributions to the energy correction in second order is given in Table 1.

Table 1: Zeroth, first and second order correction terms for the Møller-Plesset perturbation theory.[89]

Corrections (MPn)	Expression for energy correction
zeroth order (MP0)	$\sum_{i=1}^{N} \epsilon_i$
first order (MP1)	$\langle V_{ee} \rangle$
second order (MP2)	$\sum_{i<j}^{occ.} \sum_{a<b}^{virt.} \frac{[\langle \phi_i \phi_j \vert \phi_a \phi_b \rangle - \langle \phi_i \phi_j \vert \phi_b \phi_a \rangle]}{\epsilon_i + \epsilon_j - \epsilon_a - \epsilon_b}$

Unlike other methods that can be used to recover dynamic correlation, like the configuration interaction methods, MP*n* is not variational. Higher-order correction to the energy may oscillate around the correct value. Another limitation of MP2 are systems with low HOMO-LUMO gaps, as is apparent from the second order correction. Small energy-gaps may lead to unphysical values for this correction. Advantages of MP2 are its low computational cost with a scaling proportional to N^5 and its size consistency.

A significant limitation of MP2 (or MP*n* in general) has until now been ignored: It is a single-reference method and does not account for non-dynamic (static) correlation. It also breaks down when describing dissociation. For the description of open-shell system th UHF wave-function is used resulting in the unrestricted MP2 (UMP2) method.[90]

2.1.3 Algebraic Diagramatic Construction Scheme through Second Order for the Polarization Propagator

Until now, the presented methods taget the electronic ground-state of a given system. As photochemical reactions depend on the properties of excited states, appropiate methods for excited states are required.

The algebraic diagrammatic construction scheme (ADC(*n*)) is an appoximation for the polarization propagator.[91] The polarization propagator contains information about the excitation spectrum of the system[92]

$$\Pi_{pq,rs}(\omega) = \sum_{n\neq 0} \frac{\langle\psi_0|c_q^\dagger c_p|\psi_n\rangle\langle\psi_n|c_r^\dagger c_s|\psi_0\rangle}{\omega + E_0^N - E_n^N} + \sum_{n\neq 0} \frac{\langle\psi_0|c_r^\dagger c_s|\psi_n\rangle\langle\psi_n|c_q^\dagger c_p|\psi_0\rangle}{-\omega + E_0^N - E_n^N}. \tag{13}$$

In Eq. 13, ψ_0 and E_0^N are the electronic ground-state wave-function and the corresponding energy. $c_q^\dagger$ and c_p represent electronic creation and annihilation operators. ψ_n and E_n^N are excited state wavefunctions and the corresponding energies. Since both terms contain the same information, only one needs to be evaluated. For $\omega = E_0^N - E_n^N$ the propagator exhibits poles which represent the excitation energies of the system.

The ADC(*n*) expression for the polarization propagator can be derived by introducing the intermediate state representation (ISR).[93] The excited-state wave function $\tilde{\Psi}_J$ can be constructed by acting the excitation operators $\{\hat{C}_J\} = \{\hat{c}_a^\dagger\hat{c}_k, \hat{c}_a^\dagger\hat{c}_b^\dagger\hat{c}_k\hat{c}_l, ...\}$ on the ground state wave-function until the required level of excitation is reached. In the ADC(2) method, single and double excitations from the HF reference state are taken into account. In the intermediate state basis $\{\tilde{\Psi}_J\}$ the excitation energies and other properties can be calculated.[94]

Although ADC(2) is a powerfull method, it has its limits due to the single-reference ground-state wave-function. Furthermore, the weaknesses of MP2 are also carried over to ADC(2). Like MP2, the computational effort of ADC(2) scales as N^5, it is size-consistent and non-variational. A significant adventage of ADC(*n*) methods over commonly used coupled-cluster (CC) methods is its hermitian structure, which allows for a qualitatively correct description of conical intersections of excited states. For open-shell systems, the unrestricted ADC(2) (UADC(2)) method uses the UMP2 wave function as a reference state.

2.1.4 Complete-Active-Space Self-Consistent-Field Method

While the MP2 and ADC(2) methods often return accurate results, they are based on a single-reference wave function and exhibit additional limitations for open-shell systems. A more general

approach is the use of weighted contributions of a number of Slater determinants as a variational ansatz instead of RHF. This approach leads to the multi-configuration SCF (MCSCF) method. Consider a system with two degenerate orbitals ϕ_1 and ϕ_2, in which only ϕ_1 is occupied. When the orbitals are optimized (using a single reference method) the energy of ϕ_1 is lower than the energy of ϕ_2 although ϕ_1 and ϕ_2 were initially degenerate. This suggests to construct a wave-function consisting of a linear combination of Ψ_1 (with ϕ_1 occupied) and Ψ_2 (with ϕ_2 occupied):

$$\Psi_{MCSCF} = a_1|\Psi_1\rangle + a_2|\Psi_2\rangle. \tag{14}$$

The coefficients a_i in Eq. 14 are normalized weighting factors for the different configurations. Naturally, the MCSCF ansatz can be extended by additional configurations as required by the investigated problem. Unlike the previously discussed methods, the MCSCF method cannot be used as a „blackbox“ method, since the relevant configurations have to be selected by hand, which requires chemical insight.

Expanding the wave function by allowing all possible configurations for *m* electrons in *n* orbitals (short notation: (*m*,*n*)) leads to the complete-active-space SCF (CASSCF) method. The number of CSFs in the CASSCF method can be calculated using the formula:

$$N = \frac{n!(n+1)!}{(\frac{m}{2})!(\frac{m}{2}+1)!(n-\frac{m}{2})!(n-\frac{m}{2}+1)!}. \tag{15}$$

As is apparent from Eq. 15, the number of CSFs grows factorially with the size of the active space. Inclusion of all orbitals (and therefore also all electrons) in the active space is the full configuration interaction method.

A superposition of the CSFs $|\mu\rangle$ generates the CAS wavefunction $|0\rangle$[95]

$$|0\rangle = \sum_{\mu=1}^{M} C_{\mu}^{(0)}|\mu\rangle. \tag{16}$$

With $\hat{E}_{ij}$ as as spin-averaged excitation operators, h_{pq} as one- and $(pq|rs)$ two-electron integrals, the Hamiltonian is given as

$$\hat{H} = \sum_{p,q} H_{pq}\hat{E}_{pq} + \frac{1}{2}\sum_{p,q,r,s}(pq|rs)\left(\hat{E}_{pq}\hat{E}_{rs} - \delta\hat{E}_{ps}\right). \tag{17}$$

The energy of the system is, analogous to HF theory, given as

$$E_0 = \frac{\langle 0|\hat{H}|0\rangle}{\langle 0|0\rangle}. \tag{18}$$

With $|0\rangle$ normalized to unity and $D_{pq}^{(00)}$ and $P_{pqrs}^{(00)}$ as the first- and second-order reduced density matrices, the energy expression can be obtained as

$$E_0 = \sum_{p,q} h_{pq} D_{pq}^{(00)} + \sum_{p,q,r,s} (pq|rs)\, P_{pqrs}^{(00)}. \tag{19}$$

Configuration interaction expansion coefficients are contained in the density matrix elements in Eq. 19. As the configuration interaction coefficients are varied in a CASSCF optimization, a orthogonal complement to $|0\rangle$, $|K\rangle$, is constructed to describe the variations:

$$|K\rangle = \sum_{\mu=1} C_{\mu}^{(K)} |K\rangle. \tag{20}$$

The CAS wavefunction can be varied as described by a unitary operator $exp(\hat{S})$. Orbital rotations are described by a unitary operator $exp(\hat{T})$. Stationary points for the energy fulfill the criterion (with $K \neq 0$)

$$\langle 0|\hat{H}|K\rangle = \langle 0|\hat{H}\left(\hat{E}_{pq} - \hat{E}_{qp}\right)|0\rangle = 0. \tag{21}$$

The CASSCF method with restricted active spaces does not account for dynamical correlation effects. To recover this shortcoming, second-order perturbation theory based on a CASSCF reference state, the CASPT2 method, has been developed to treat dynamical correlation effects.

2.1.5 Second Order Perturbation Theory with the CASSCF Wavefunction

The second order perturbation theory with the CASSCF wavefunction (CASPT2) method can be viewed as the multi-reference counterpart to the MP2 method. The challenge at hand is finding a zero-order Hamiltonian, whose ground-state is the multiconfigurational wavefunction. In the following, the focus will be on the perturbative expansion with respect to a CASSCF wavefunction. As MP*n* perturbation theory can be used as a sucessfull example of perturbation theory for the description singleconfigurational systems, it is reasonable to extend the formalism to multiconfigurational systems and use the Fock operator as the zero-order Hamiltonian. The CASSCF Fock

operator $\hat{f}$ is given by

$$\hat{f} = \sum_{pq} f_{pq} E_{pq} = \frac{1}{2} \sum_{pq} \sum_{\sigma} \langle 0| \left[a^{\dagger}_{q\sigma}, \left[a_{p\sigma}, \hat{H} \right] \right]_{+} |0\rangle E_{pq}. \tag{22}$$

$\hat{a}^{\dagger}_{q\sigma}$ and $\hat{a}_{p\sigma}$ represent creation and annihilation operators respectively. As $|0\rangle$ is not an eigenfunction of $\hat{f}$ and $\hat{H}_0$ must have $|0\rangle$ as an eigenstate, the zero-order Hamiltonian is chosen as

$$\hat{H}_0 = E^{(0)} |0\rangle\langle 0| + \hat{P}\hat{f}\hat{P}. \tag{23}$$

$\hat{P}$ is the projector $\hat{P} = 1 - |0\rangle\langle 0|$ and $E^{(0)}$ the zero-order energy given by

$$E^{(0)} = \langle 0|\hat{f}|0\rangle. \tag{24}$$

If the $|0\rangle$ is a single-determinant closed-shell state, the zero-order Hamiltonian in Eq. 23 reduces to the Møller-Plesset Fock operator.[96] The structure of the CASSCF Fock matrix of an optimized CASSCF state is illustrated in Table 2. The three diagonal blocks are diagonal. The inactive-secondary elements (f_{ai}) vanish at stationary points. The block coupling inactive and secondary orbitals is zero.

Table 2: The structure of the CASSCF Fock matrix of an optimized CASSCF state.[96]

	inactive	active	secondary
inactive	f_{ii}	f_{iv}	0
active	f_{vi}	f_{vv}	f_{va}
secondary	0	f_{av}	f_{aa}

For simplicity, the following matrices and vectors are defined: $(H_0)_{ij} = \langle i|\hat{H}_0|j\rangle$, $S_{ij} = \langle i|j\rangle$ and $V_i = \langle i|\hat{H}|0\rangle$ for $i, j = 1, ..., M$. *M* is the number of double replacement states. With $\Lambda_S = \mathbf{U}^{\dagger}\mathbf{S}\mathbf{U}$, the second order energy can be formulated as

$$E^{(2)} = -\left(\Lambda_S^{-\frac{1}{2}}\mathbf{U}^{\dagger}\mathbf{V}\right)^{\dagger} \left[\left(\mathbf{U}\Lambda_S^{-\frac{1}{2}}\right)^{\dagger} \mathbf{H}_0 \left(\mathbf{U}\Lambda_S^{-\frac{1}{2}}\right) - E_0\mathbf{1} \right]^{-1} \left(\Lambda_S^{-\frac{1}{2}}\mathbf{U}^{\dagger}\mathbf{V}\right). \tag{25}$$

2.2 Born-Oppenheimer approximations, Potential Energy Surfaces and Chemical Reaction Paths

The wavefunction $\Psi_{m\nu}$ of a system with the quantum number m for the light particles (electrons) and ν for heavy particles (nuclei) reduces in the adiabatic approximation to a simple product[97]

$$\Psi_{mv} = \phi_m\left(\mathbf{r}, \mathbf{R}\right) \chi^0_{mv}\left(\mathbf{R}\right). \tag{26}$$

$\phi\left(\mathbf{r}, \mathbf{R}\right)$ represents the wavefunction of the electrons and $\chi\left(\mathbf{R}\right)$ the wavefunction of the nuclei depending on the set of all electron coordinates **r** and all nuclear coordinates **R**. Eq. 26 is also referred to as the Born-Oppenheimer (BO) approximation.[98] Inserting $\Psi_{m\nu}$ into the Schrödinger equation, multiplying by $\phi^*_m\left(\mathbf{r}, \mathbf{R}\right)$ and integrating over **r** generates a set of independent equations

$$\left[\hat{T}_n + \epsilon_m(\mathbf{R})\right] \chi^0_{m\nu}(\mathbf{R}) = E^0_{m\nu}\chi^0_{m\nu}(\mathbf{R}). \tag{27}$$

$\hat{T}_n$ is the kinetic energy operator of the nuclei. The potential energy $\epsilon_m(\mathbf{R})$ of the electrons in the state m in Eq. 27 thus characterizes the motion of the nuclei.

With the BO approximation it is possible to construct electronic potential energy (PE) surfaces which are functions of all nuclear coordiantes **R**. As each nucleus can be displaced along the three Cartesian coordinates, these PE surfaces have 3*N* dimensions, *N* being the number of nuclei. As the displacement and rotation of the entire system do not contribute to the energy, the use of internal coordinates is appropiate. This reduces the dimensionality of the PE surface by 6 (5 for linear systems).

On these PE surfaces stationary points, which correspond to maxima, minima and saddle points-geometries can be identified. Equilibrium geometries correspond to local minima, whereas transition states are first-order saddle points. By connecting equilibrium geometries by following the steepest descent from a transition state, minimum-energy paths (MEP) are obtained.[99] Local gradients of the PE surface can be interpreted as forces, which in turn can be employed to solve Newton's equation of motion to describe nuclear motion on a given PE surface.[100, 101] Barriers on a given PE surface can be overcome if the total available energy is higher than the energy of the barrier.

The adiabatic representation of the wavefunction and the Schrödinger equation have their limits, as they neglect the coupling between PE surfaces of two adiabatic states. To account for nonadiabatic effects, the wavefunction from Eq. 26 can be rewritten in a more general form. This is

known as the Born-Huang expansion.[102]

$$\Psi\left(\mathbf{r},\mathbf{R}\right)=\sum_{i}\phi_{i}\left(\mathbf{r},\mathbf{R}\right)\chi_{i}\left(\mathbf{R}\right). \tag{28}$$

As the set $\{\phi_i(\mathbf{r},\mathbf{R})\}$ with the electronic coordinates **r** and nuclear coordinates **R** is complete, formally Eq. 28 is exact. $\Psi(\mathbf{r},\mathbf{R})$ thus is a reasonable ansatz to describe a bound state solution of the Schrödinger equation

$$H\Psi(\mathbf{r},\mathbf{R})=E\Psi(\mathbf{r},\mathbf{R}). \tag{29}$$

Inserting Eq. 28 into Eq. 29, multiplying from the left by ϕ^*, integrating over the electronic coordinates one arrives at the coupled equations as shown in Eq. 30.[103]

$$\left[T_n+V_j(\mathbf{R})\right]\chi_j(\mathbf{R})-\sum_i\Lambda_{ji}\chi_i(\mathbf{R})=E\chi_j(\mathbf{R}). \tag{30}$$

T_n is the kinetic energy operator of the nuclei and Λ is the so-called nonadiabatic coupling describing dynamical interaction between the electronic and nuclear motion. Its elements are given by

$$\Lambda_{ji}=\delta_{ji}T_n-\langle j(\mathbf{R})|T_n|i(\mathbf{R})\rangle=\frac{1}{2M}\left[2\mathbf{F}_{ji}\cdot\nabla+G_{ji}\right]. \tag{31}$$

The formulation in Eq. 31 contains the nonadiabatic derivative coupling elements $\mathbf{F}_{ji}$ and the nonadiabatic scalar couplings G_{ji}. These elements are defined as

$$\begin{aligned}\mathbf{F}_{ji}(\mathbf{R})&=\langle j(\mathbf{R})|\nabla i(\mathbf{R})\rangle\\ G_{ji}(\mathbf{R})&=\langle j(\mathbf{R})|\nabla^2 i(\mathbf{R})\rangle.\end{aligned} \tag{32}$$

Using these results Eq. 30 can be rewritten as shown in Eq. 33.[104]

$$\left[-\frac{1}{2M}\left(\nabla+\mathbf{F}_{ji}(\mathbf{R})\right)^2+V_j(\mathbf{R})-E\right]\chi_j=0. \tag{33}$$

This representation shows that to study the coupled motion of the electrons and nuclei only the nuclear motion in the matrix potential **V** is needed.[103] For well separated electronic states Λ decreases. Neglect of Λ leads to the BO adiabatic approximation as shown in Eq. 30 above.[105] To understand the breakdown of the BO adiabatic approximation, it is instructive to take a closer look at the derivative coupling $\mathbf{F}_{ji}$. The derivative coupling $\mathbf{F}_{ji}$ between two different states *i* and *j*

can be presented in the form given in Eq. 34.

$$\mathbf{F}_{ji}(\mathbf{R}) = \frac{\langle j(\mathbf{R})|(\nabla H_e)|i(\mathbf{R})\rangle}{V_i(\mathbf{R}) - V_j(\mathbf{R})}. \tag{34}$$

It can be seen that for energetically close states *i* and *j* the derivative coupling becomes very large. At conical intersections it becomes infinite rendering the adiabatic approximation unapplicable.[106] Exception for this breakdown exists, e.g. where the numerator vanishes due to a spatial symmetry.

2.3 Quasi-classical nonadiabatic excited-state dynamics

When the BO approximation breaks down, the nuclear motion must be treated on multiple coupled PE surfaces. The reason for this is often the existence of conical intersections, in which two or more states become degenerate and efficient population transfer between different PE surfaces is possible.[103, 107–110] In order to take these nonadiabatic into account, multiple approaches with different advantages and limitations have been developed.[111, 112] They can be divided into quantum dynamical and quasi-classical approaches, according to the underlying principle. The multi-configuration time-dependent Hartree (MCTDH) method can be named as a well established quantum dynamical approach.[107, 113–116] It requires the calculation of the PE surface prior to the investigation of the excited-state dynamics rendering its application cost-intensive. A quasi-classical approach to investigate nonadiabatic dynamics are the trajectory surface hopping (TSH) methods. Here, trajectories are propagated independently from each other in a given adiabatic electronic state.
The procedure of TSH methods for photoinduced processes can be summarized by four simple steps:

1. Generation of initial geometries and momenta and assignment of an initial electronic state.

2. Solve Newton's equation of motion for a short time interval Δt in the assigned electronic state.

3. Calculate switching probabilities (see below) from the current state to all other states.

4. By Monte Carlo sampling, continue in the active electronic state or change the electronic

state to a new state and continue from step 2.

Two of these TSH methods will be discussed in the following. In 1990, Tully introduced the „fewest switches“ surface hopping (FSSH) algorithm to treat non-adiabatic effects in molecular dynamics.[117] In this algorithm electronic transitions are treated by surface hopping, while other quantum effects are ignored. The time-derivative nonadiabatic coupling σ_{LJ}^{NAC} is given as

$$\sigma_{LJ}^{NAC} = \langle \Psi_L | \frac{\partial \Psi_J}{\partial t} \rangle. \tag{35}$$

It is a product of the nonadiabatic coupling vector $\mathbf{d}_{LJ} \equiv \langle \Psi_L | \nabla \Psi_J \rangle$ and the classical nuclear velocity **v**. The electronic wavefunction is propagated in time according to the time-dependent Schrödinger equation (TDSE). In Tully's algorithm a trajectory is propagated on a single PE surface and switches between states occur instantaneously from the initial to the final state. The transition probability between two states L and J is calculated as:

$$P_{L\to J}^{FSSH} = max\left[0, \frac{2\Delta t}{\rho_{LL}}\left(\hbar^{-1} Im(H_{LJ}\rho_{JL}) - Re(\sigma_{LJ}^{NAC}\rho_{JL})\right)\right]. \tag{36}$$

In Eq. 36 H_{LJ} denotes the element of the electronic Hamiltonian between the states L and J, ρ describes the densitiy matrix. The density matrix ρ is constructed by the coefficients of the electronic states which form a linear combination of the electronic wavefunction. Whether or not a hopping event occurs is estimated based on the inequality given in Eq. 37, where r_i is a randomly generated number.[112]

$$\Sigma_{K=1}^{J-1} P_{L\to K}^{FSSH} < r_i \leq \Sigma_{K=1}^{J} P_{L\to J}^{FSSH} \tag{37}$$

Switches from a state L to all states J are possible which requires the calculation of all $P_{L\to J}^{FSSH}$ throughout the calculation. Especially for long simulation times and systems including a large number of states this procedure can become very cost intensive.
The couplings near avoided crossings and conical intersections strongly vary in Tully's approach. A contrast to that is the Landau-Zener (LZ) formalism, in which the transition probability between electronic states is directly determined from the topography of the adiabatic potentials in energy-crossing regions. The TDSE does not have to be solved within this framework.
In 2011 Belyaev and Lebedev proposed a formula for the calculation of transition probabilities, using the LZ model.[118] Within the LZ model the adiabatic energy gap $Z_{jk} = |U_j - U_k|$ is calculated with $U_j(R)$ and $U_k(R)$ being adiabatic potentials for the states *j* and *k*. The nonadiabatic transition probability within the LZ model at the minimum of the energy gap is calculated as (primes

denote derivatives with respect to the distance R, dots represent derivatives with respect to time):

$$p_{jk} = exp\left(-\frac{\pi}{2\hbar\nu}\sqrt{\frac{Z_{jk}^3}{Z_{jk}''}}\right) = exp\left(-\frac{\pi}{2\hbar}\sqrt{\frac{Z_{jk}^3}{\ddot{Z}_{jk}}}\right) \tag{38}$$

In this LZ model only transitions between neighboring adiabatic states are possible. Furthermore, the calculation of hopping probabilities is only conducted in nonadiabatic regions, which lowers the computationl cost.

3 Photoinduced Reduction of CO_2 with the Heptazinyl Radical

3.1 Introduction

In a recent computational study, Wu *et al.* made an attempt to simulate the joint processes of water oxidation and carbon dioxide activation via a carbamate complex for a model of heptazine-based graphitic carbon nitride (g-C_3N_4).[119] The ground-state PE landscape of heptazine-CO_2-H_2O complexes was explored with density functional theory calculations with periodic boundary conditions. In the electronic ground-state, however, both water oxidation and CO_2 activation exhibit high energy barriers and a convincing reaction mechanism could not be identified.[119] In the present work, the possibility of using the HzH radical (generated via the photo-oxidation of water) for the reduction of CO_2 is investigated. While the reducing power of the HzH radical in the electronic ground-state is insuffcient for the activation of CO_2, it will be shown that the photoexcited HzH radical can reduce CO_2 to the hydroxy-formyl (HOCO) radical in a nearly barrierless excited-state PCET reaction. Because the reduction of CO_2 requires the breaking of a C=O double bond, multi-configuration multi-reference electronic-structure methods are indispensable for an accurate description. While such sophisticated electronic-structure calculations are impossible for extended (periodic or polymeric) systems, they are feasible for complexes of the molecular building blocks of PCNs with substrate molecules.

3.2 Computational Methods

The CASSCF[95] and CASPT2[120] methods were used in this work. The active space for the CASSCF calculations was selected as follows. For the planar HzH$\cdots$OCO complex (C_s symmetry), the four highest π orbitals and the four lowest π^* orbitals of HzH were included in the active space. These orbitals were found to have occupation numbers between 0.02 and 1.98 in an UHF calculation. The singly occupied molecular orbital (SOMO) is a π orbital. In addition, the lowest unoccupied molecular orbital (LUMO) of HzH, which is a σ^* orbital localized on the NH group, was included in the active space to be able to accurately describe the $^2\pi\sigma^*$ excited state. Orbitals of CO_2 were not included in the active space because they are too low in energy to be of relevance. The active space thus consisted of seven electrons distributed in nine orbitals, denoted as (7,9). Calculations with the same active space were performed for the product geometry (Hz$\cdots$HOCO) and for the transition state of the PCET reaction. At these three geometries (educt, transition state, and product), calculations with a (11,13) active space were performed.The (7,9) active space represents a good compromise between accuracy and computational cost. With

respect to computational cost and stability, a compact active space is to be preferred for calculations of PE surfaces over a wide range of internal nuclear coordinates, as is required for the present study. For the calculation of the energies of the higher excited $^2\pi\pi^*$ states (D_4, D_5), the (7,9) active space was extended by an additional π orbital and an additional π^* orbital.

For the states of A″ symmetry (ground state and $^2\pi\pi^*$ excited states of HzH$\cdots$OCO), the CASSCF functional was averaged over the ground state (D_0) and the two lowest $^2\pi\pi^*$ excited states (D_1, D_2). For the calculation of the energy of the D_4 and D_5 states, the CASSCF functional was averaged over the D_0, D_4, and D_5 states. In geometry optimizations, no state-averaging was employed.

Dunning's augmented correlation-consistent polarized valence-split double-ζ (aug-cc-pVDZ) basis set[121] was employed on all atoms. The augmentation is necessary to account for the diffuse Rydberg character of the σ^* orbital in the vicinity of the HzH$\cdots$OCO ground-state equilibrium geometry. Due to the high computational cost of this basis set, a partially augmented basis set was constructed, in which the aug-cc-pVDZ basis was employed on the frontier atoms of the HzH radical as well as the CO_2 molecule, whereas the standard cc-pVDZ basis was employed on the remaining atoms. While the reduction in computational cost is significant, the effect on the energies is minor (ΔE < 0.1 eV). The definition of the partially augmented basis for the HzH$\cdots$OCO complex is illustrated in Figure 1. The augmented cc-pVDZ basis is employed for the atoms marked in red, whereas the nonaugmented cc-pVDZ basis is used for the atoms marked in black in Figure 1.

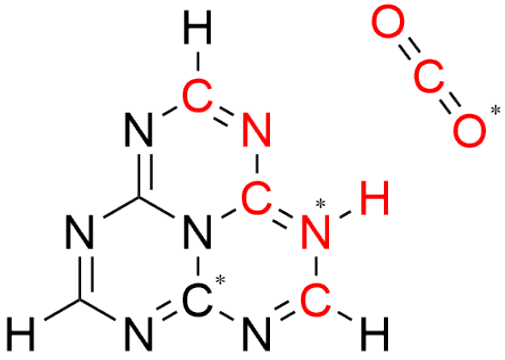

Figure 1: Definition of the partially augmented basis set applied in the calculations. The aug-cc-pVDZ basis was employed on the atoms marked red, while the standard cc-pVDZ basis was employed on the atoms marked black. The angle defined by the atoms marked with an asterisk was fixed at 180°.

Because the HzH$\cdots$OCO hydrogen bond is rather weak and the PE surface is rather flat with respect to the location and orientation of the CO_2 molecule, it was found helpful to impose a constraint on the location of the CO_2 molecule. The C, N, and O atoms marked with an asterisk

in Figure 1 were constrained to lie on a line. The position of the reactive hydrogen atom is not included in this constraint.

The saddle point (transition state) of the PCET reaction was optimized with the CASSCF method on the PE surface of the $^2\pi\sigma^*$ state (D_3 state) with C_s symmetry constraint. It was verified that it is a first-order saddle point by the calculation of the Hessian at this geometry.

A one-dimensional relaxed scan of the PE surface of the $^2\pi\sigma^*$ state of the HzH$\cdots$OCO complex, which is diabatically connected with the electronic ground-state of Hz$\cdots$HOCO, was constructed as a function of the OCO-bending angle. For a fixed OCO angle, the energy of the $^2\pi\sigma^*$ state was optimized with respect to all other internal degrees of freedom at the CASSCF level. The energies of the $^2\pi\sigma^*$ state and the other electronic states were determined by single-point CASPT2 calculations at the $^2\pi\sigma^*$-optimized geometries.

Furthermore, three two-dimensional relaxed PE surfaces of the $^2\pi\sigma^*$ state of HzH$\cdots$OCO were constructed as functions of the NH distance, the NO distance, and the OCO-bending angle. Two of these three internal coordinates were fixed, while the energy of the $^2\pi\sigma^*$ state was minimized with respect to all other internal coordinates of the complex at the CASSCF level. Single-point energy calculations were performed at these optimized geometries with the CASPT2 method. An imaginary level shift parameter of 0.15 Hartree was used to mitigate the effect of intruder states. The combination of CASSCF-optimized geometries and CASPT2 single-point energies is designated as CASSCF//CASPT2 in what follows. Cubic spline functions were used to interpolate the CASPT2 data. The CASSCF and CASPT2 calculations were performed with the OpenMolcas program package (V18.09).[122]

3.3 Results

3.3.1 Educt Equilibrium Geometry and Vertical Excitation Energies

The ground-state equilibrium geometry of the HzH$\cdots$OCO complex (the educt of the PCET reaction) optimized at the CASSCF level with C_s symmetry constraint is displayed in Figure 2 (a). This geometry agrees well with the geometry determined with the UMP2 method.

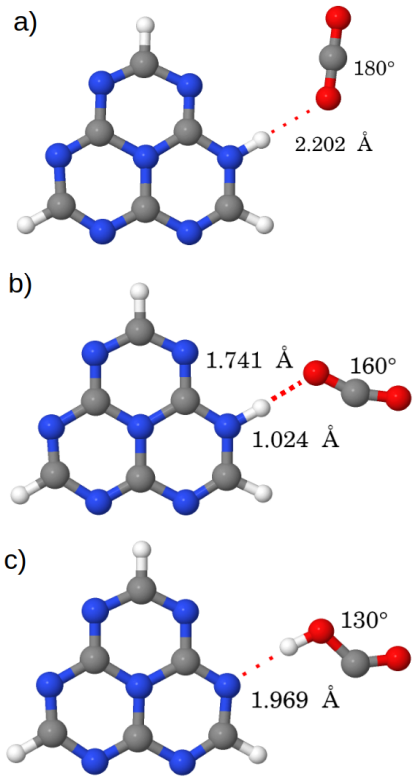

Figure 2: (a) Ground-state equilibrium structure of the HzH$\cdots$OCO complex. (b) Structure of the transition state. (c) Ground-state equilibrium structure of the complex of Hz with the *trans* conformer of HOCO.

The five lowest vertical excitation energies of the HzH radical and the HzH$\cdots$OCO complex and the corresponding oscillator strengths, calculated with the CASSCF and CASPT2 methods, are listed in Table 3. The D_1, D_2, D_4, and D_5 states are locally excited $^2\pi\pi^*$ states of HzH. The D_3 state is the photochemically reactive $^2\pi\sigma^*$ state. The $^2\pi\pi^* \leftarrow D_0$ transitions are allowed with relatively low oscillator strengths. The $^2\pi\sigma^* \leftarrow D_0$ transition has zero oscillator strength. The inclusion of dynamical electron correlation with the CASPT2 method lowers the energies of the $^2\pi\pi^*$ states significantly (up to 0.8 eV), while the energy of the $^2\pi\sigma^*$ state is increased by 0.3–0.4 eV. The complexation of HzH with CO_2 leads to a slight blue shift of the $^2\pi\pi^*$ excitation energies of the

Table 3: Vertical excitation energies (in eV) and oscillator strengths of the HzH radical and the HzH$\cdots$OCO complex at CASSCF and CASPT2 levels.

state	HzH			HzH$\cdots$OCO		
	CASSCF	CASPT2	osc. strength	CASSCF	CASPT2	osc. strength
D_1 ($^2\pi\pi^*$)	1.88	1.29	0.025	2.00	1.41	0.027
D_2 ($^2\pi\pi^*$)	2.23	1.50	0.013	2.48	1.58	0.011
D_3 ($^2\pi\sigma^*$)	2.89	3.34	0.000	3.17	3.38	0.000
D_4 ($^2\pi\pi^*$)	4.10	3.47	0.014	4.44	3.82	0.013
D_5 ($^2\pi\pi^*$)	4.96	4.19	0.110	4.70	4.37	0.004

order of 0.2 eV, while the excitation energy of the $D_3(^2\pi\sigma^*)$ state is essentially unaffected.
The results of the benchmark calculations at three stationary point of this reaction are listed in Table 4. The results obtained with the extended (11,13) active space are in good agreement with the results obtained with the chosen (7,9) active space.

Table 4: CASPT2 vertical excitation energies (in eV) at the educt, transition state and product geometries. Excitation energies obtained with the (11,13) active space (+1σ, +1σ^*, +1π, +1π^*) are compared with the excitation energies obtained with the (7,9) active space.

state	educt (11,13)	educt (7,9)	TS (11,13)	TS (7,9)	product (11,13)	product (7,9)
D_1 ($^2\pi\pi^*$)	1.35	1.41	0.73	0.71	0.13	0.12
D_2 ($^2\pi\pi^*$)	1.57	1.58	0.97	0.99	0.93	0.88
D_3 ($^2\pi\sigma^*$)	3.33	3.38	2.61	2.67	-3.94	-3.98
D_4 ($^2\pi\pi^*$)	3.85	3.82	3.52	3.46	—	—
D_5 ($^2\pi\pi^*$)	4.39	4.37	3.89	3.91	—	—

3.3.2 Transition-State Geometry and Product Equilibrium Geometry

The product of the excited-state PCET reaction, the Hz$\cdots$HOCO complex, exhibits four coplanar conformers of similar energies. The HOCO radical exists in the *trans* and *cis* conformations, and it can twist around the N$\cdots$H-O hydrogen bond. The four product conformers as well as their energies relative to the educt energy are shown in Figure 3. The *cis* configurations are slightly higher in energy than the *trans* configurations. Herein, the PE surfaces of the PCET reaction will be discussed for the lowest-energy *trans* product conformer shown in Figure 2 (c). The analogous discussion of the PE surfaces for one of the *cis* conformers of Hz$\cdots$HOCO is given in appendix **A.1**.
The structure of the transition state of the excited-state PCET reaction is shown in Figure 2 (b). The length of the N-H$\cdots$O hydrogen bond at the saddle point is 1.741 Å and thus much shorter

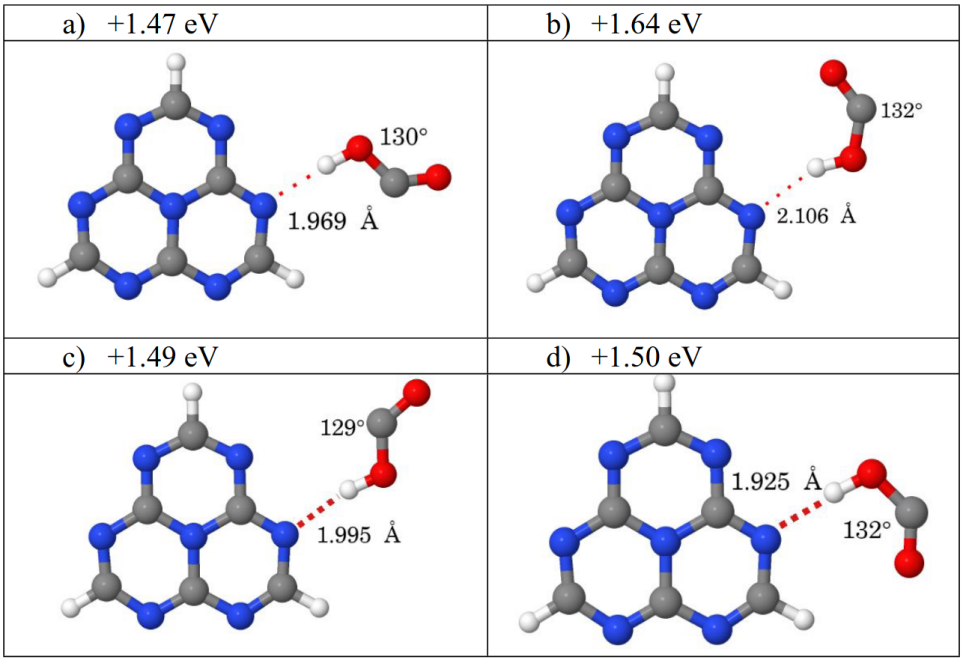

Figure 3: Geometries of the four possible reaction products and their energies relative to the educt energy.

than the hydrogen bond length at the educt geometry. The OCO angle is reduced by about 20°, while the extension of the NH bond length is minor (1.024 Å).

The ground-state equilibrium geometry of the Hz···HOCO product is shown in Figure 2 (c). The hydrogen bond length of 1.969 Å indicates a hydrogen bond which is slightly stronger than the hydrogen bond of the educt. The OCO bond angle is 130°, which is close to the bond angle of 138° of the CO_2^- anion.[123, 124]

The relative energies of the three stationary points (educt, transition state, and product) are sketched in Figure 4. On the left side, the optimized energy of the local minimum of the D_3 state in the Franck–Condon region is shown, which is 3.35 eV above the ground-state equilibrium geometry of HzH···OCO and 0.03 eV below the vertical excitation energy. The energy of the transition state is 0.08 eV below the vertical excitation energy and 0.05 eV below the energy minimum of the D_3 state. The ground-state energy of the Hz···HOCO product is 1.47 eV above the ground-state energy of the educt and 1.91 eV below the vertical excitation energy of the $D_3(^2\pi\sigma^*)$ state. The Hz···HOCO complex is thus a metastable species which is energetically accessible upon photoexcitation to the $D_3(^2\pi\sigma^*)$ state of the HzH···OCO complex. It should be noted that the wave function of the $D_3(^2\pi\sigma^*)$ state of HzH···OCO is diabatically connected with the wave function of the electronic ground-state of Hz···HOCO. This wave function is of A′ symmetry and is decoupled from the wave functions of the D_0 and $^2\pi\pi^*$ states of HzH···OCO as

long as the system remains planar.

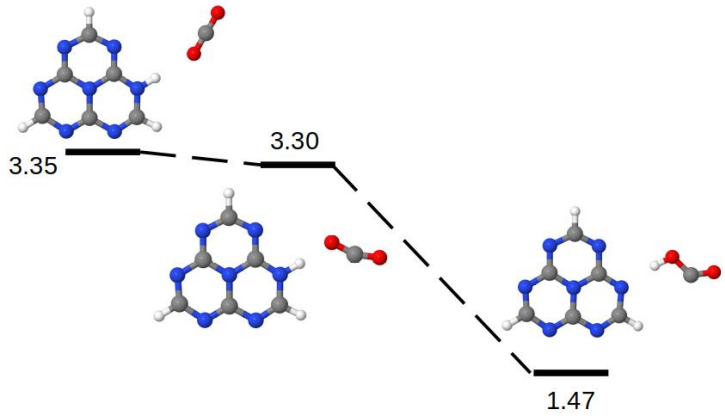

Figure 4: Energy levels of the three stationary points of the excited-state PCET reaction in the HzH$\cdots$OCO complex. The energies (in eV) are given relative to the ground-state energy of HzH$\cdots$OCO. The depicted structures represent the equilibrium geometry of the D_3 excited state (left), the structure of the transition state (middle), and the structure of the product (right).

3.3.3 Orbitals

It is instructive to consider first the orbitals of the isolated HzH radical. We show CASSCF orbitals which are essentially identical with UHF orbitals. The SOMO and the LUMO of the isolated HzH radical at its ground-state equilibrium geometry are displayed in Figure 5 (a) and (b), respectively. The SOMO is a nondegenerate π orbital. The LUMO is of very different character. It is a diffuse Rydberg orbital which is located mostly outside the Hz frame and is anti-bonding with respect to the NH bond (note the nodal plane across the NH bond). The role of the σ^* orbital for the H-atom photodetachment reaction of the HzH radical has been discussed in an earlier study.[73] The NH anti-bonding character of the σ^* orbital renders the PE function of the $^2\pi\sigma^*$ state repulsive along the NH stretching coordinate(see Section **4.3.1**). The σ^* orbital plays an essential role for the excited-state H-atom transfer reaction in the HzH$\cdots$OCO complex. The center of its charge distribution is shifted toward the CO_2 molecule when the latter attaches via a hydrogen

bond to the NH group of HzH. The SOMO and the LUMO of the HzH$\cdots$OCO complex at its

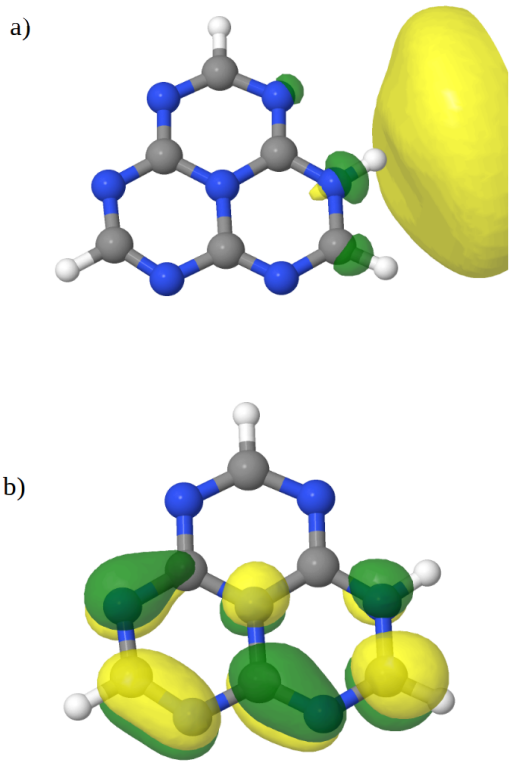

Figure 5: LUMO (a) and SOMO (b) of the HzH radical at its ground-state equilibrium structure.

ground-state equilibrium geometry are displayed in Figure 4. The SOMO (Figure 6 (a)) is virtually unaffected by the complexation with the CO_2 molecule (compare Figure 6 (a) with Figure Figure 5 (b)). The diffuse LUMO of the complex, on the other hand, is very different from the LUMO of isolated HzH. It is shown in Figure 6 (b), (c) in top and side views, respectively. The Pauli repulsion with the charge distribution of HzH splits the LUMO into two lobes above and below the molecular plane. This shape is reminiscent of a „sandwich“ enveloping the heptazinyl radical. Note that it nevertheless is a σ orbital, that is, both lobes have the same sign (encoded by the color). The shape of the fluxional σ^* orbital is extremely sensitive to the NH distance of HzH (the proton transfer coordinate), the NO distance (the donor–acceptor distance of the N$\cdots$H$\cdots$O hydrogen bond), and the OCO bending angle. Snapshots of the σ^* orbital at three selected geometries of the PCET reaction are shown in Figure 6 (b), (c) (educt geometry) and in Figure 7 for selected geometries along the H-atom transfer reaction path. Upon elongation of the NH bond and decrease of the NO distance (by 0.25 Å), the σ^* orbital locates on the CO_2 molecule, as shown in top and side views in Figure 7 (a), (b). At the geometry of the transition state of the PCET reaction (Figure 7 (c)), the orbital is localized on the CO_2 molecule, forming a diffuse lobe on the C atom. At the product geometry (Figure 7 (d)), the orbital has contracted and is

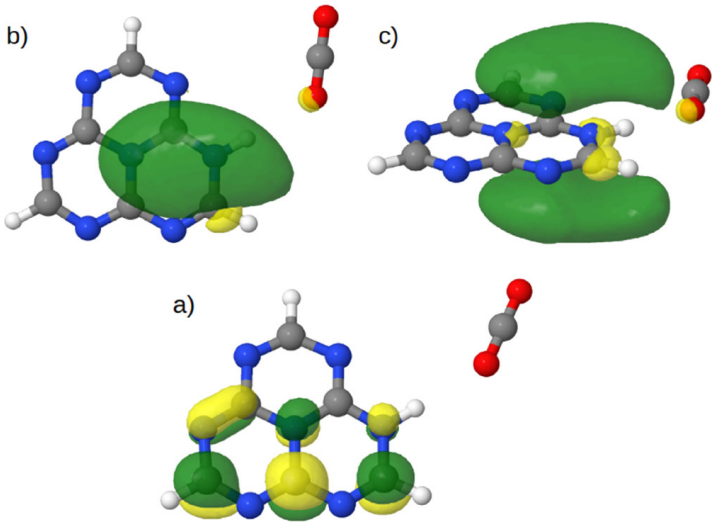

Figure 6: SOMO (a) and top view (b) and side view (c) of the LUMO of the HzH$\cdots$OCO complex at its ground-state equilibrium structure.

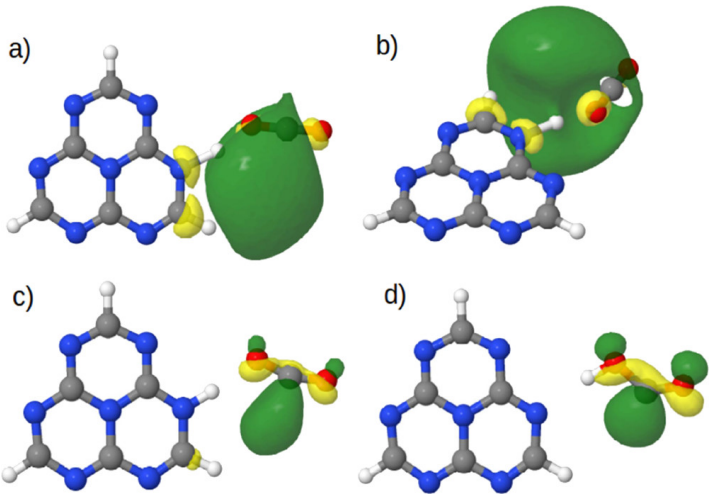

Figure 7: Snapshots of the σ^* orbital at three selected geometries of the PCET reaction. Top view (a) and side view (b) at an extension of the NH distance by 0.25 Å, at the transition-state (c) and at the ground-state equilibrium geometry of the Hz$\cdots$HOCO complex (d).

fully localized on the CO_2 molecule. These figures nicely illustrate the electronic mechanism of the PCET reaction: the electron in the σ^* orbital is providing the driving force for the bending of the CO_2 molecule and the proton transfer from HzH to CO_2 and its density distribution in turn is localized on the HOCO radical by the bending of CO_2 and the transfer of the proton.

3.3.4 Relaxed Scan for H-Atom Transfer

It is clear from the structures of educt and product complexes that at least three reaction coordinates are needed for the description of the carbon dioxide reduction reaction in the HzH$\cdots$OCO complex: (i) the proton transfer coordinate (NH or OH distance), (ii) the distance of the donor and acceptor of the proton (NO distance), and (iii) the bending angle of the CO_2 molecule. This fact illustrates that the theoretical description of the carbon dioxide reduction reaction is considerably more challenging than the description of the water oxidation reaction. The latter involves the breaking of an OH single bond and can be characterized by two reaction coordinates (proton transfer coordinate and donor-acceptor distance). Moreover, single-reference electronic-structure methods are sufficient to describe the breaking of a single bond, while the breaking of a double bond in the reduction of carbon dioxide necessarily requires multi-configuration methods.
As can be seen from the inspection of Figure 6 and Figure 7, the OCO angle plays a decisive role in the excited-state CO_2 reduction reaction because it controls the localization of the transferred electron on the CO_2 molecule. We therefore constructed a relaxed scan on the PE surface of the $^2\pi\sigma^*$ excited state, taking the OCO bending angle as the driving coordinate (see section **3.2**). The CASSCF//CASPT2 PE profiles along this relaxed scan are shown in Figure 8. The blue line with full dots represents the energy of the $^2\pi\sigma^*$ state which was minimized for a fixed OCO bending angle with respect to all other nuclear coordinates. The energies of the $^2\pi\pi^*$ states calculated at the same geometries are depicted by green open dots and the energy of the D_0 state is represented by black open dots. The two insets display the geometries at OCO angles of 160° (left) and 159° (right). Bending the CO_2 molecule from 180° to 160° causes a small increase of the energy of the $^2\pi\sigma^*$ state by less than 0.2 eV. The D_0 and $^2\pi\pi^*$ energies also increase in a parallel manner. As shown by the left inset, the reactive H atom still resides on Hz at an OCO angle of 160°. Inspection of the σ^* orbital at this geometry (not shown) reveals that the electron is transferred to the CO_2 molecule, where it occupies a diffuse lobe located on the carbon atom. Decreasing the OCO angle from 160° to 159° leads to the transfer of the proton from HzH to CO_2 in the relaxed scan. The proton transfer causes the significant drop in the energy of the $^2\pi\sigma^*$ state and the strong increase of the energies of the D_0 and $^2\pi\pi^*$ states, as shown in Figure 8. The seemingly discontinuous changes of the energies of the D_0, $^2\pi\pi^*$, and $^2\pi\sigma^*$ states are not

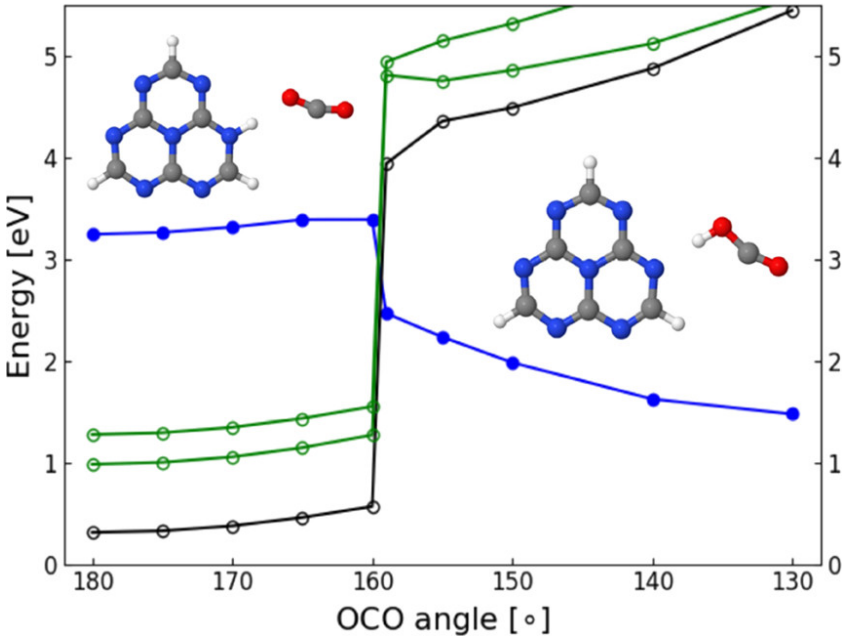

Figure 8: Energy profiles of the relaxed scan of the HzH···OCO complex along the OCO-bending angle. Black: electronic ground-state; green: $^2\pi\pi^*$ states; blue: $^2\pi\sigma^*$ state. Full circles indicate that the reaction path geometry was optimized in this state; open circles indicate that the geometry was optimized in a different state. The insets depict the geometries at OCO angles of 160° (left) and 159° (right). The energies are given relative to the energy minimum of the electronic ground-state of the HzH···OCO complex.

a computational artifact, but reflect the spontaneous transfer of the proton at this critical bending angle. The apparent discontinuity of the energies disappears when the NH distance (the proton transfer coordinate) is fixed. The OCO angle at the transition state is 159.6° and thus midway between the two geometries shown in the insets in Figure 8. Further decrease of the OCO angle toward the equilibrium value of the HOCO radical causes further stabilization of the energy of the $^2\pi\sigma^*$ state, while the energies of the other three states gradually increase.

3.3.5 Two-Dimensional Relaxed PE Surfaces

The electron/proton transfer reaction in the HzH···OCO complex is not well characterized by one-dimensional relaxed scans along either the proton transfer coordinate or the OCO bending angle. To obtain a meaningful picture in terms of reaction coordinates, it is necessary to extend the description to two-dimensional relaxed scans, combining (i) the NH distance with the OCO angle, (ii) the NO distance with the OCO angle, and (iii) the NH distance with the NO distance. While the latter representation is the standard choice for PCET reactions, [125, 126] it will be

seen that this representation has pathological features for the CO_2 reduction reaction because the optimization of the energy with respect to the OCO angle for fixed NH and NO distances leads to discontinuities of the relaxed energy surface.

The two-dimensional relaxed scan of the PE surface of the electronic state of A′ symmetry ($^2\pi\sigma^*$ excited state at the educt geometry and ground state at the product geometry) calculated at the CASSCF//CASPT2 level as a function of the OCO angle and the NH distance is shown in Figure 9. The educt geometry (Figure 2 (a)) corresponds to the upper left corner. The bottom right

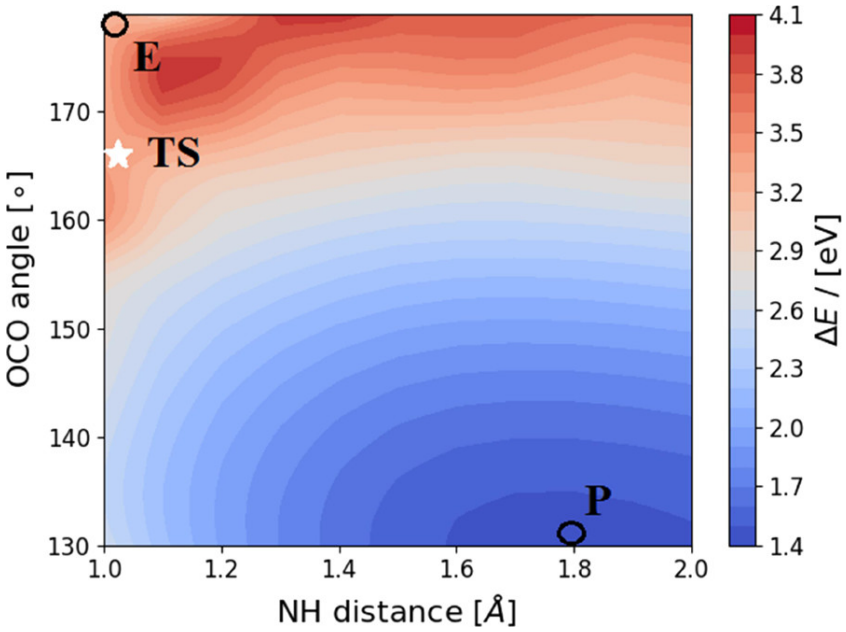

Figure 9: Two-dimensional relaxed PE surface of the $^2\pi\sigma^*$ excited state of the HzH$\cdots$OCO complex calculated at the CASSCF//CASPT2 level. The reaction coordinates are the NH distance of the HzH fragment and the OCO bending angle of CO_2. The color code gives the energy (in eV) relative to the energy minimum of the electronic ground-state of the HzH$\cdots$OCO complex. The educt (E) and product (P) geometries are marked by circles. The transition state (TS) is marked by the star.

area corresponds to the product geometry (Figure 2 (c)). The cut along the NH distance for an OCO angle of 180° (upper rim of Figure 9) reveals a barrier near an NH distance of 1.4 Å. The cut along the OCO angle for an NH distance of 1.0 Å (left rim of Figure 9) exhibits a barrier near an OCO angle of 162.5°. For OCO angles larger than about 165°, the CO_2 molecule remains neutral and protonation is energetically unfavorable. For OCO angles below 165°, the electron in the σ^* orbital is spontaneously transferred from HzH to the CO_2 molecule, forming the CO_2^- anion. Protonation of this anion is energetically favorable, which causes the deep well around the OCO angle of 130° and NH distance of 1.8 Å, as shown in Figure 9. The peak in the energy surface near an NH distance of 1.1 Å and an OCO angle of 175° is caused by the energy cost of

bending of the CO_2 molecule (which is not reduced at this geometry) as well as by a small barrier in the energy profile of the H-atom photodetachment from the HzH radical in the $^2\pi\sigma^*$ state. Both of these effects add up to generate this local maximum. It can be seen in Figure 9 that a low-barrier reaction path starting at the upper left corner exists which initially involves bending for a fixed NH distance, followed by concerted bending and NH stretching toward the deep minimum at the product geometry. The saddle point of the two-dimensional relaxed surface is located at an OCO angle of 167.5° and an NH distance of 1.05 Å. The barrier along the minimum energy reaction path in Figure 9 is estimated as 0.1 eV.

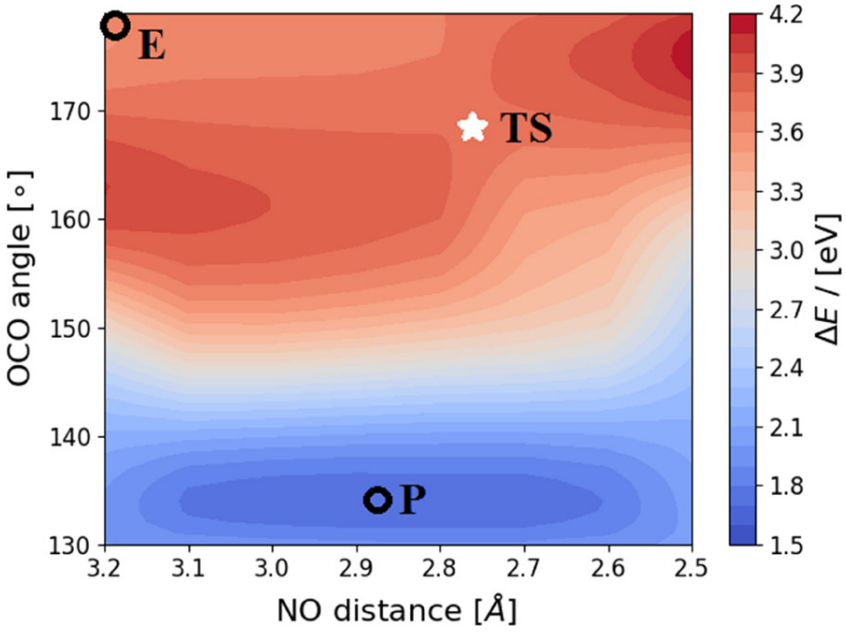

Figure 10: Two-dimensional relaxed PE surface of the $^2\pi\sigma^*$ excited state of the HzH···OCO complex calculated at the CASSCF//CASPT2 level. The reaction coordinates are the NO distance of the HzH···OCO and the OCO bending angle of CO_2. The color code gives the energy (in eV) relative to the energy minimum of the electronic ground-state of the HzH···OCO complex. The educt (E) and product (P) geometries are marked by circles. The transition state (TS) is marked by the star.

The two-dimensional relaxed PE surface of the A′ state of the HzH···OCO complex as a function of the OCO angle and the NO distance, calculated at the CASSCF//CASPT2 level, is displayed in Figure 10. The top left corner corresponds to the educt geometry (Figure 2 (a)). The stretched well in the bottom region of Figure 10 corresponds to the product geometry (Figure 2 (c)). The energy profile of the cut along the upper rim (variation of the NO distance for linear CO_2) is initially flat and then rises steeply, revealing the weak attraction of linear CO_2 by HzH along the NO distance, followed by strong repulsion at short distances. The energy profile of the cut along the left rim (variation of the OCO angle for a fixed NO distance of 3.2 Å) exhibits a barrier near an OCO

angle of 162°. The two-dimensional surface shows that a low-barrier reaction path exists. The minimum energy reaction path initially involves mainly a decrease of the NO distance, followed by bending for a nearly fixed NO distance. The saddle point corresponds to an OCO angle of 168° and an NO distance of 2.76 Å. The height of the barrier along this path is estimated as 0.1 eV. Figure 10 reveals that the contraction of the donor–acceptor distance plays an important role in the initiation of the reaction, as is typical for PCET reactions.

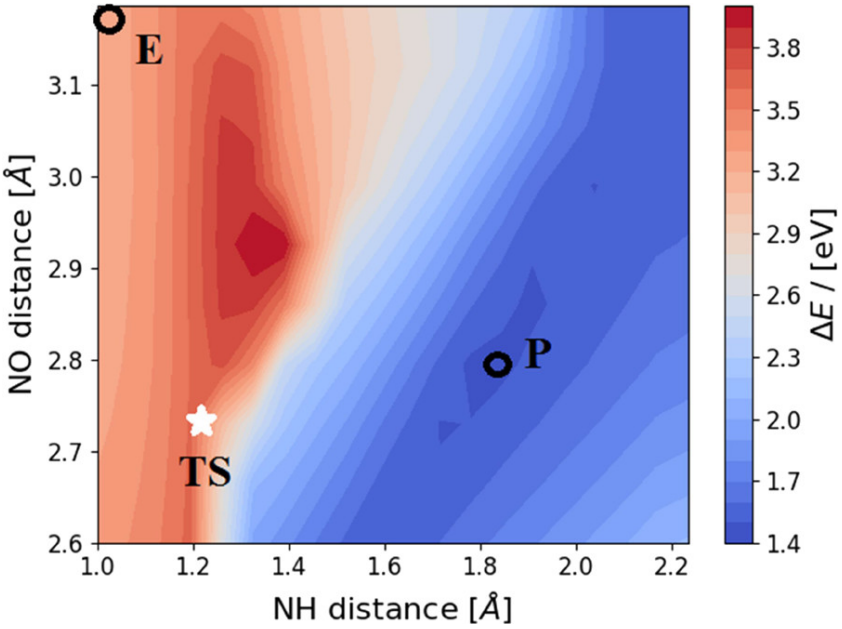

Figure 11: Two-dimensional relaxed PE surface of the $^2\pi\sigma^*$ excited state of the HzH···OCO complex calculated at the CASSCF//CASPT2 level. The reaction coordinates are the NO distance of Hz···OCO and the NH distance of the HzH fragment. The color code gives the energy (in eV) relative to the energy minimum of the electronic ground-state of the HzH···OCO complex. The educt (E) and product (P) geometries are marked by circles. The transition state (TS) is marked by the star.

For completeness, the two-dimensional relaxed PE surface of the A′ state of the HzH···OCO complex as a function of the NH distance and the NO distance, calculated at the CASSCF//CASPT2 level, is displayed in Figure 11. This PE surface exhibits two plateaus which differ in energy by about 2 eV and correspond to linear (red) and bent (blue) CO_2, respectively. The nearly discontinuous character of the relaxed surface reflects the sudden large energy gain by the bending of the CO_2 molecule as soon as it can catch the electron from the H-atom of HzH, as shown in Figure 8. The transition state is characterized by a strongly reduced NO distance (analogous to Figure 10) and a slightly extended NH distance.

3.4 Discussion

State-of-the-art electronic-structure calculations were employed in this work to shed light on the photochemistry of the hydrogen-bonded HzH$\cdots$OCO complex. The analysis of the frontier molecular orbitals reveals the detailed electronic mechanism of the photoinduced reduction and protonation of the CO_2 molecule. The HzH chromophore can be excited to the $D_3(^2\pi\sigma^*)$ electronic state either by a vibronically induced radiative transition or by excitation of a higher-lying allowed $^2\pi\pi^*$ state followed by internal conversion to the $^2\pi\sigma^*$ state. Efficient radiationless transitions in polyatomic molecules are usually driven by conical intersections.[103] The existence of a conical intersection of the PE surfaces of the $D_4(^2\pi\pi^*)$ and $D_3(^2\pi\sigma^*)$ states is confirmed by the linear scan shown in Figure 12.

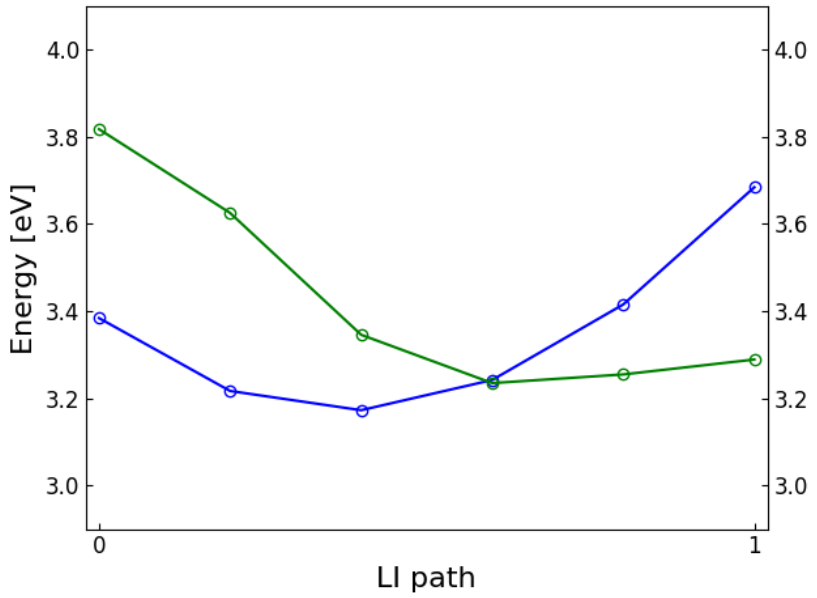

Figure 12: Energy profiles of the $D_3(^2\pi\sigma^*)$ state (blue) and the $D_4(^2\pi\pi^*)$ state (green) of the HzH$\cdots$OCO complex along a linearly interpolated scan from the ground-state equilibrium geometry of the educt (left) to the equilibrium geometry geometry of the D_4 state (right). The crossing of the energy profiles confirms the existence of a conical intersection.

In the photoexcited complex, a shortening of the length of the HzH$\cdots$OCO hydrogen bond by a thermal fluctuation is sufficient to induce the transfer of the diffuse σ^* orbital to the electron-deficient carbon atom of CO_2 (Figure 7 (a), (b)). Once the σ^* electron has been transferred, the energy of the excited state is strongly stabilized by the bending of the CO_2 molecule. As a result of the bending, the σ^* orbital contracts and localizes mainly on the carbon atom of CO_2 (Figure 7

(c)). The electronic charge separation in turn drives the transfer of a proton across the hydrogen bond of the complex, resulting in the formation of the HOCO radical (Figure 7 (d)).
The energetics of the photoreaction is characterized by the relaxed PE surfaces, as shown in Figure 9 and Figure 10. Taken together, these surfaces reveal the existence of a minimum energy reaction path from the photoexcited HzH$\cdots$OCO complex to the Hz$\cdots$HOCO complex which exhibits a very low reaction barrier ($\approx$ 0.1 eV). The minimum energy reaction path involves mainly a shortening of the NO distance toward 2.8 Å, combined with a bending of the OCO molecule (Figure 10).

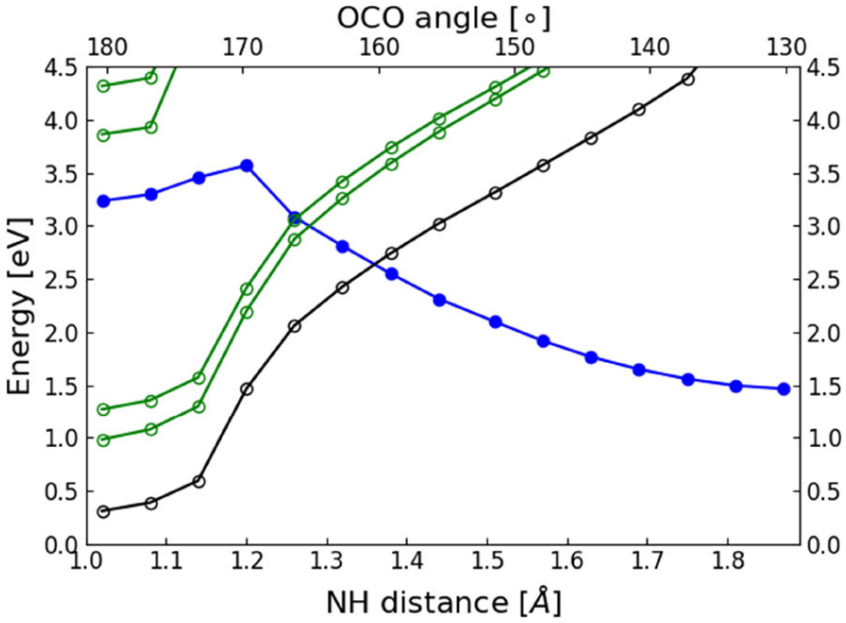

Figure 13: Energy profiles of the electronic ground-state of the HzH$\cdots$OCO complex (black), of four $^2\pi\pi^*$ excited states (green), and of the $^2\pi\sigma^*$ excited state (blue) along a linear cut from the ground-state equilibrium geometry of the HzH$\cdots$OCO educt complex to the equilibrium geometry of the *trans* Hz$\cdots$HOCO product complex.

Along the reaction path from the educt geometry to the product geometry, the energy profile of the $^2\pi\sigma^*$ state intersects the energy profiles of two low-lying $^2\pi\pi^*$ states and the energy profile of the D_0 ground state of the HzH$\cdots$OCO complex. This is illustrated in Figure 13, which shows the energy profiles along a linear cut from the upper left corner to the lower right corner of Figure 9. The variation of the OCO angle and the NH distance along this cut is shown at the top and the bottom of the figure, respectively. The left hand side of Figure 13 corresponds to the educt configuration (linear CO_2 which is hydrogen-bonded to HzH) and the right hand side to the product configuration (HOCO radical which is hydrogen-bonded to Hz). The filled blue circles represent the energy of the $^2\pi\sigma^*$ state of HzH$\cdots$OCO, which was minimized for the construction of the

relaxed surface shown in Figure 9. The green open circles in Figure 13 represent the energies of the $^2\pi\pi^*$ states, while the black open circles represent the energy of the ground state of the HzH$\cdots$OCO complex at the same geometries. It is seen that the energy of the $^2\pi\sigma^*$ excited state of the HzH$\cdots$OCO complex is diabatically connected to the electronic ground-state of the Hz$\cdots$HOCO complex. The $^2\pi\sigma^*$ energy profile exhibits a maximum about 0.34 eV above the energy of the educt geometry near an NH distance of 1.2 Å. The steep increase of the D_0, D_1, and D_2 energies near NH distances of 1.2 Å is caused by a strong decrease of the NO distance (and implicitly the OH distance).

For the planar complex, the intersections of the energy of the $^2\pi\sigma^*$ state of A′ symmetry with the energies of the $^2\pi\pi^*$ and D_0 states of A″ symmetry are symmetry-allowed intersections. They become conical intersections[103] when out-of-plane vibrational modes are taken into account. Figure 13 illustrates that the CO_2 reduction reaction in the electronic ground-state is endothermic by 1.5 eV and exhibits a high reaction barrier ($\approx$ 2.5 eV). The reaction in the $^2\pi\sigma^*$ excited state, on the other hand, is exothermic by 1.9 eV and is essentially barrierless (Figure 9 and Figure 10). The yield of the excited-state PCET reaction in the HzH$\cdots$OCO complex is thus not determined by the reaction barrier (which is lower than the zero-point energy of the H-atom transfer mode), but by the nonadiabatic dynamics at the conical intersections. Nonadiabatic quantum dynamics simulations are required for the estimation of the electronic branching ratios at these conical intersections and thus the reaction yield.

A drawback of the photochemical CO_2 reduction mechanism sketched herein is the short lifetime of the excited electronic states of the HzH radical due to internal conversion to the electronic ground-state as well as photodetachment of the excess H-atom. The latter process is analogous to the photochemistry of $^1\pi\sigma^*$ states in aromatic chromophores with acidic groups, such as pyrrole, indole, or phenol, in which an antibonding σ^* orbital drives rapid (nonstatistical) photodetachment of the H-atom from NH or OH groups.[127–130] The lifetime of the $^2\pi\sigma^*$ excited state of HzH very likely is too short to allow diffusion-controlled reactions with CO_2 molecules. The preassociation of the CO_2 molecule with the HzH chromophore therefore is an essential requirement for productive CO_2 reduction photochemistry. This requirement may possibly not be fulfilled in experiments due to the limited solubility of CO_2 in water.

On the other hand, excitation of the $^2\pi\sigma^*$ state of HzH in aqueous environments can lead to the formation of hydrated electrons. Recent calculations predict a barrierless reaction path devoid of conical intersections for the photoinduced formation of the $H_3O\cdots(H_2O)_{n-1}$ radical in $HzH\cdots(H_2O)_n$ clusters.[131] The hydrated H_3O radical is a convenient finite-size model of the hydrated electron in bulk water.[55, 70] The lifetime of the hydrated electron at ambient conditions is of the order of a microsecond,[53] which is sufficient for effective diffusion-controlled reactions.

Hydrated electrons are known to reduce CO_2 in a nearly diffusion-limited reaction.[51, 132, 133] A barrier of merely 0.16 eV (15.9 kJ/mol) and a rate constant of $1.53 \cdot 10^{11}$ M^{-1} s^{-1} at 300 K were determined by Lisovskaya and Bartels.[134] Interestingly, water acts as a catalyst in this scenario, mediating the transfer of electrons from photoexcited HzH radicals to CO_2 molecules. This section has been published, see [135].

4 Photogeneration of Hydrated H_3O Radicals with the Heptazinyl Radical

4.1 Introduction

The sustainable generation of hydrated electrons requires that the electrons are taken from an abundant chemical like water. Pyridine and Pyrimidine absorb in the far UV and generate OH radicals from water and the PyH and PmH radicals respectively. UV radiation is then required for the photodetachment of the excess H atom and generation of hydrated electrons. However, a larger N-heterocycle, Hz absorbs strongly in the near UV and weakly even in the visible range of the spectrum.[136, 137] Ehrmaier *et al.* described a water-splitting cylce using Hz and hydrogen-bonded water to transfer a H atom from water to Hz in a PCET reaction forming the HzH radical and a OH radical. The HzH radical can be taken and undergo a second photoinduced reaction. The calculations of Ehrmaier *et al.* predicted that the low-lying bound $^2\pi\pi^*$ states of the HzH radical are predissociated by $^2\pi\sigma^*$ states which are repulsive with respect to the NH bond length, like in the PyH and PmH radicals.[73] In the present work, we explored with electronic-structure calculations the possibility of the generation of hydrated hydronium radicals by the photodetachment of H-atoms from the HzH radical in water clusters.

4.2 Computational Methods

The ground-state equilibrium geometries of the HzH radical and the $HzH\cdots H_2O$ and $HzH\cdots(H_2O)_4$ complexes were optimized with the UMP2 method.[90] The UMP2 method is preferred here to the CASSCF method[95] for geometry optimization, because dynamic electron correlation effects, which are relevant for the description of weak long-range interactions such as hydrogen bonds, are taken into account in the former. The higher accuracy of the UMP2 geometries was confirmed by selected geometry optimizations for HzH and $HzH\cdots H_2O$ with the CASPT2 method.[138] The electronic ground-state wave-function of the HzH radical is of A'' symmetry in the C_s symmetry group, since the unpaired electron occupies a π orbital. The equilibrium geometries of the $HzH\cdots H_2O$ and $HzH\cdots(H_2O)_4$ complexes were optimized with C_s symmetry constraint. The H_2O molecule in the $HzH\cdots H_2O$ complex is constrained to lie perpendicular to the molecular plane of HzH and the H_2O molecules in the $HzH\cdots(H_2O)_4$ complex are arranged symmetrically to the HzH molecular plane. The C_s symmetry constraint is essential for geometry optimizations in excited electronic states (see below), because the symmetry constraint prevents

the collapse of the energy of the lowest A′ state to the energies of lower A″ states.
Vertical electronic excitation energies were calculated with the CASPT2 method. The active space for the CASSCF calculations for the HzH radical and its complexes with water consisted of seven active electrons distributed in nine orbitals (7,9), four π orbitals, four π^* orbitals and one σ^* orbital of HzH. In A″ symmetry, the CASSCF energy functional was averaged over the three lowest states of A″ symmetry. The energies of the lowest $^2\pi\pi^*$ states and $^2\pi\sigma^*$ states were found to be stable with respect to extensions of the active space. For the calculation of higher excited states of $^2\pi\pi^*$ character (D_4, D_5), the active space was extended by an additional π^* orbital and the D_1, D_2 states were not included in the state averaging. In the CASPT2 calculations, an imaginary denominator shift of 0.15 Hartree was chosen to mitigate intruder state problems. A default ionization potential-electron affinity (IPEA) shift of 0.25 Hartree was used in all CASPT2 calculations.[139] All CASPT2 calculations were performed with the multi-state CASPT2 (MS-CASPT2) method.[138]
For HzH and the HzH$\cdots H_2O$ complex, the aug-cc-pVDZ basis set[121] was employed. For geometry optimizations of the HzH$\cdots(H_2O)_4$ complex, a partially augmented basis set was used. The non-augmented cc-pVDZ basis was employed on the HzH chromophore, while the aug-cc-pVDZ basis was chosen for the $(H_2O)_4$ cluster. The partial augmentation lowered the cost of the geometry optimizations by around 70%. The fully augmented basis was used for single-point energy calculations for the HzH$\cdots(H_2O)_4$ complex. We tested the accuracy of the approximation of partial augmentation for selected optimized geometries. The differences of the geometries obtained with the partially augmented basis and the fully augmented basis were minimal.
The TURBOMOLE program package (V 6.3.1)[140] was employed for the UMP2 calculations, making use of the resolution-of-the-identity (RI) approximation. The OpenMolcas program package (V 18.09)[122] was used for the CASSCF and CASPT2 calculations.
The energy profiles for the photodissociation reaction of the HzH radical were computed along a rigid scan by stretching the NH bond length, keeping all other internal nuclear coordinates fixed at the UMP2-optimized ground-state equilibrium geometry. The photoinduced PCET reaction in the HzH$\cdots H_2O$ and HzH$\cdots(H_2O)_4$ complexes was characterized by the calculation of minimum-energy paths as relaxed scans in the lowest $^2\pi\sigma^*$ excited state at the UMP2 level. For a fixed NH distance of HzH, the $^2\pi\sigma^*$ energy was optimized with respect to all other internal degrees of freedom of the complexes. In addition, the ground-state equilibrium geometries of the H-atom-transferred structures, Hz$\cdots H_3O$ and Hz$\cdots H_3O(H_2O)_3$, were fully optimized at the UMP2 level. Single-point energy calculations at the UMP2-optimized geometries were performed with the CASPT2 method. Such energies are referred to as UMP2//CASPT2 in what follows.
In addition, macroscopic solvent effects were taken into account using a polarizable continuum

(PC) model described by Barone and Cossi and implemented in the OpenMolcas Package.[141, 142] To simulate the macroscopic water environment, the dielectric constant was set to ϵ=78.39. The continuum solvation shell was relaxed for the electronic ground-state.
Finally, the dissociation energies of the Hz$\cdots$H$_3$O and Hz$\cdots$H$_3$O(H$_2$O)$_3$ complexes into Hz+H$_3$O and Hz+H$_3$O(H$_2$O)$_3$, respectively, were computed at the UMP2//CASPT2 level.

4.3 Results

4.3.1 The HzH Radical

The excited states of the HzH radical and the potential energy functions for the H-atom photodetachment reaction from HzH were calculated by Ehrmaier *et al.*[73] with the UADC(2) method. Here, we briefly present results for the HzH photodissociation reaction obtained at the CASPT2 level as references for the H-atom transfer reactions in HzH-water complexes.
At the UMP2 level, the minimum energy configuration of the HzH radical exhibits a slight out-of-plane bending of the CH bond. The planar configuration (C_s symmetry) is a first-order saddle point. Since the stabilization of the ground-state energy by the slight out-of-plane bending of the NH group is minor, we choose the planar conformation as the reference geometry, because the excited-state calculations are greatly simplified by C_s symmetry. The NH bond length of planar HzH is 1.016 Å at the UMP2/aug-cc-pVDZ level. Since the singly occupied orbital (SOMO) is a π orbital of A$''$ symmetry, the electronic ground-state of HzH is of A$''$ symmetry. The lowest unoccupied molecular orbital (LUMO) is a diffuse σ^* orbital of A$'$ symmetry and the $^2\pi\sigma^*$ excited state therefore is of A$'$ symmetry. The SOMO and the LUMO of HzH are displayed in Figure 5 (b) and Figure 5 (a), respectively.
Whereas the highest occupied molecular orbital (HOMO) of Hz is localized on the peripheral N-atoms and the LUMO of Hz is located on the peripheral C-atoms as well as the central N-atom,[73] the SOMO of HzH is delocalized over both C-atoms and N-atoms, see Figure 5 (b). The structure of the LUMO is remarkable: the electronic density is to a large extent localized outside the molecular frame and the orbital is antibonding with respect to the NH bond (see Figure 5 (a)). The SOMO-to-LUMO excitation is accompanied by a significant shift of the electronic charge from the aromatic ring beyond the H-atom of the NH group, which results in a significant dipole moment of the $\pi\sigma^*$ excited state (10.57 Debye). The vertical excitation energies of the lowest five excited states of HzH calculated with the CASPT2 method are listed in the left column of Table Table 5.
The lowest two excited states (D_1, D_2), with excitation energies of 1.32 eV and 1.42 eV, are of

Table 5: Vertical excitation energies [eV], oscillator strengths *f* (in parentheses) and characters of the HzH, HzH$\cdots$H$_2$O and HzH$\cdots$(H$_2$O)$_4$ radicals at the CASPT2 level.

State	HzH	HzH$\cdots$H$_2$O	HzH$\cdots$(H$_2$O)$_4$
D$_1$	1.32 (0.025) [$\pi\pi^*$]	1.36 (0.053) [$\pi\pi^*$]	1.32 (0.052) [$\pi\pi^*$]
D$_2$	1.42 (0.013) [$\pi\pi^*$]	1.72 (0.018) [$\pi\pi^*$]	1.57 (0.018) [$\pi\pi^*$]
D$_3$	3.32 (0.000) [$\pi\sigma^*$]	3.36 (0.002) [$\pi\pi^*$]	3.39 (0.003) [$\pi\pi^*$]
D$_4$	3.48 (0.014) [$\pi\pi^*$]	3.50 (0.003) [$\pi\sigma^*$]	3.63 (0.001) [$\pi\sigma^*$]
D$_5$	4.13 (0.110) [$\pi\pi^*$]	4.07 (0.023) [$\pi\pi^*$]	3.93 (0.034) [$\pi\pi^*$]

$^2\pi\pi^*$ character, while the third excited state (D$_3$) is of $^2\pi\sigma^*$ character. The following two states (D$_4$, D$_5$) are again $^2\pi\pi^*$ states. The $^2\pi\pi^*$ states have non-vanishing, albeit small, oscillator strengths, while the $^2\pi\sigma^*$ state is dark due to the non-overlapping nature of SOMO and LUMO.

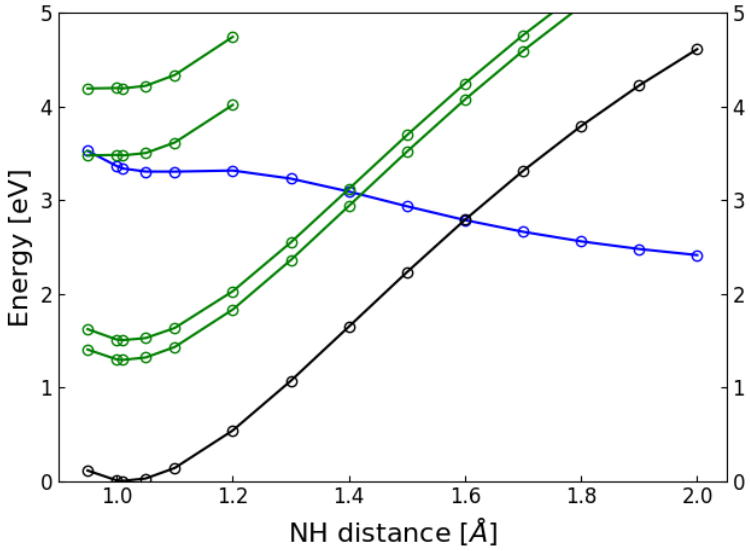

Figure 14: Cut of the PE surface (rigid scan) of the HzH radical along the NH stretching coordinate at the CASPT2 level. Black: electronic ground-state; green: $\pi\pi^*$ excited states; blue: $\pi\sigma^*$ excited state.

The potential-energy (PE) functions (calculated as rigid scan) for the H-atom abstraction reaction from HzH are shown in Figure 14. A relaxed scan yields essentially identical PE functions. While the PE functions of the $^2\pi\pi^*$ states D$_1$, D$_2$, D$_4$, D$_5$ are essentially parallel to the PE function of the electronic ground-state, the PE function of the $^2\pi\sigma^*$ state is dissociative apart from a tiny barrier near R$_{NH}$=1.2 . The $^2\pi\sigma^*$ energy intersects the energies of the D$_1$, D$_2$ excited states as well as the energy of the D$_0$ state. These curve crossings, which become conical intersections when out-of-plane vibrational modes are taken into account, provide a mechanism for predissociation of the $^2\pi\pi^*$ excited states as well as the electronic ground-state of HzH. The $^2\pi\sigma^*$ state

of HzH dissociates homolytically into Hz and a neutral hydrogen atom, whereas the ground state and the $^2\pi\pi^*$ excited states dissociate heterolytically into ion pairs, the anion of Hz and a proton. The large dipole moment of the $^2\pi\sigma^*$ state at the ground-state equilibrium geometry decreases strongly with increasing RNH, while the dipole moments of the ground state and the $^2\pi\pi^*$ excited states gradually increase with R_{NH}. This behaviour of the dipole moment functions is illustrated in Figure 15.

The dissociation energy D_e of HzH is computed as 2.22 eV at the CASPT2 level, in good agreement with the estimate of 2.0 eV at the CCSD level.[73]

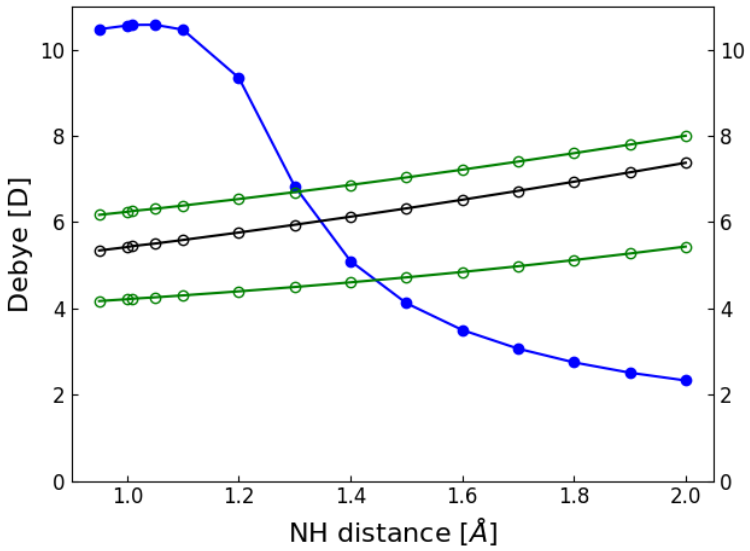

Figure 15: Dipole moment of the HzH radical along the NH stretching coordinate (rigid scan) at CASSCF level. Black: electronic ground-state; green: $\pi\pi^*$ excited states; blue: $\pi\sigma^*$ excited state.

4.3.2 The HzH$\cdots$H$_2$O Complex

The ground-state equilibrium structure of the HzH$\cdots$H$_2$O complex is shown in Figure 16 (a). The NH bond length is 1.032 Å. The length of the NH$\cdots$OH$_2$ hydrogen bond is 1.823 Å, which represents a rather strong hydrogen bond.

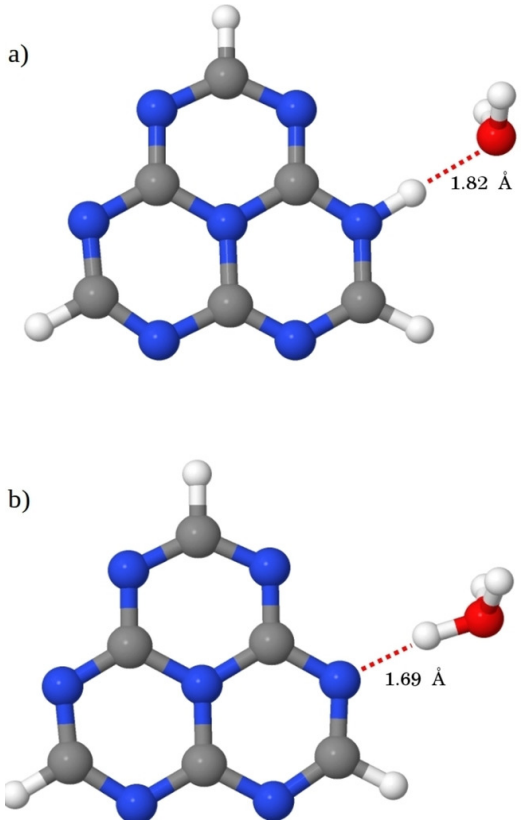

Figure 16: (a) Ground state equilibrium structure of the HzH$\cdots$H$_2$O complex. (b) Ground state equilibrium structure of the Hz$\cdots$H$_3$O complex.

The frontier molecular orbitals (SOMO and LUMO) of the HzH$\cdots$H$_2$O complex are displayed in Figure 17. Whereas the π-type SOMO is essentially unperturbed by the hydrogen bond with the H$_2$O molecule (Figure 17 (b)), the σ^*-type LUMO is strongly affected. It is pushed away from the aromatic frame and represents an external electron cloud which is solvated by the two OH bonds of the H$_2$O molecule (Figure 17 (a)). The vertical electronic excitation energies of the HzH$\cdots$H$_2$O complex are listed in the middle column of Table 5. In HzH$\cdots$H$_2$O, the D$_3$($\pi\sigma^*$) state is slightly destabilized, while the D$_4$($\pi\pi^*$) state is slightly stabilized with respect to the free HzH radical. As a result, the ordering of these closely spaced states is interchanged, see Table 5. The D$_2$($\pi\pi^*$) state exhibits the largest shift in energy (+0.30 eV) due to the hydrogen bonding of HzH with H$_2$O. The CASPT2 PE profiles of the minimum-energy path (calculated as relaxed scan at the UMP2

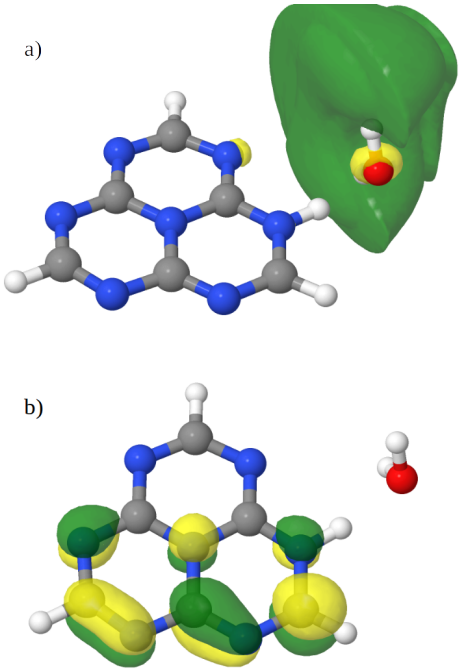

Figure 17: LUMO (a) and SOMO (b) of the HzH$\cdots$H$_2$O complex at the ground state equilibrium structure.

level, see Section **4.2**) for the excited-state PCET reaction from HzH to H_2O are shown in Figure 18. The energies of the D_0 state (black), the D_3 state of $^2\pi\sigma^*$ character (blue) and the D_1, D_2, D_4, D_5 states of $^2\pi\pi^*$ character (green) were computed with the CASPT2 method along the $^2\pi\sigma^*$-optimized reaction path. Compared with the PE functions of the H-atom detachment reaction in HzH (Figure 14), the $^2\pi\sigma^*$ PE function becomes somewhat less repulsive, while the PE profiles of the D_0 state and the $^2\pi\pi^*$ excited states become significantly less attractive. The stabilization of the energies of the D_0 state and the $^2\pi\pi^*$ states at large NH distances reflects the large energy gain by the formation of the H_3O^+ cation upon proton transfer from HzH to H_2O. While the D_0 energy of isolated HzH is about 3.5 eV at R_{NH}=1.7 Å, the D_0 energy is lowered to 1.9 eV at R_{NH}=1.7 Å in the HzH$\cdots$H$_2$O complex. The PE profile of the $^2\pi\sigma^*$ state of HzH$\cdots$H$_2$O, on the other hand, is lowered at short NH distances and raised at large NH distances and therefore flattened compared to the PE profile of HzH. This flattening in the HzH$\cdots$H$_2$O complex is due to the decrease of the dipole moment of the $^2\pi\sigma^*$ state along the H-atom transfer reaction path, see Figure 15. While the $^2\pi\sigma^*$ state is highly polar at the ground-state equilibrium geometry of HzH$\cdots$H$_2$O, it becomes nonpolar when Hz and the H_3O radical are formed at large NH distances. The intersection of the $^2\pi\sigma^*$ energy function with the D_0 energy in free HzH disappears and the intersection of the $^2\pi\sigma^*$ energy with the $D_2(\pi\pi^*)$ energy is shifted outward to 1.7 Å, see Figure 18.

As a result, there exists a barrierless reaction path for H-atom transfer in the $^2\pi\sigma^*$ state of the HzH$\cdots$H$_2$O complex which leads to a conical intersection with the $^2\pi\pi^*$ state (D$_2$) at large NH distances (Figure 18).

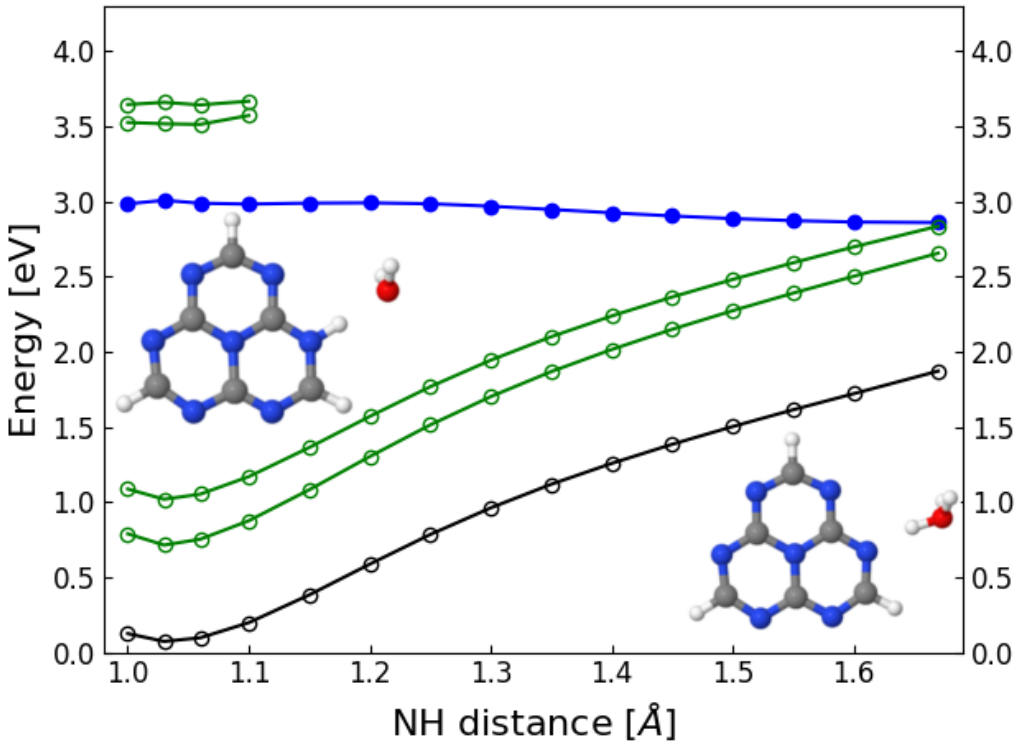

Figure 18: Energy profiles of the relaxed scan of the HzH$\cdots$H$_2$O complex along the NH-stretching coordinate. The minimum-energy path is optimized in the $\pi\sigma^*$ state at the UMP2 level. Energies are calculated with the CASPT2 method at the UMP2-optimized geometries. Black: electronic ground-state; green: $\pi\pi^*$ states; blue: $\pi\sigma^*$ state. Full circles indicate that the reaction path geometry was optimized in this state; open circles indicate that the reaction path geometry was optimized in a different state.

The $^2\pi\sigma^*$ PE surface of the HzH$\cdots$H$_2$O complex exhibits a very shallow minimum corresponding to a Hz$\cdots$H$_3$O structure which is shown in Figure 16 (b). The length of the N$\cdots$HO hydrogen bond of this complex is 1.691 Å, shorter than the hydrogen bond in the HzH$\cdots$H$_2$O complex (1.823 Å). The stabilization energy with respect to the vertical excitation energy of the $^2\pi\sigma^*$ state is 0.65 eV. The computed energy of dissociation of the Hz$\cdots$H$_3$O complex into Hz and the H$_3$O radical is 0.30 eV. Vertical excitation of the $^2\pi\sigma^*$ state in HzH$\cdots$H$_2$O complexes will therefore likely lead to H-atom transfer.

4.3.3 The HzH$\cdots(H_2O)_4$ Complex

The ground-state geometry of the HzH$\cdots(H_2O)_4$ complex was optimized at the UMP2 level with C_s symmetry constraint. While there exist a large number of possible equilibrium structures of this complex, the structure of the water cluster has been chosen such that the H_2O molecule in the first solvation shell is bonded as H-atom acceptor to the NH group of HzH. The two OH bonds of this H_2O molecule form hydrogen bonds to two H_2O molecules in the second solvation shell. The fourth H_2O molecule forms a weak hydrogen bond with the N-atom adjacent to the NH group of HzH, see Figure 19. The length of the hydrogen bond between the NH group of HzH and the closest water molecule is 1.632 Å. The significant shortening of this hydrogen bond compared to the HzH$\cdots H_2O$ complex (1.823 Å) indicates a significant strengthening of the HzH$\cdots H_2O$ hydrogen bond in the larger complex.

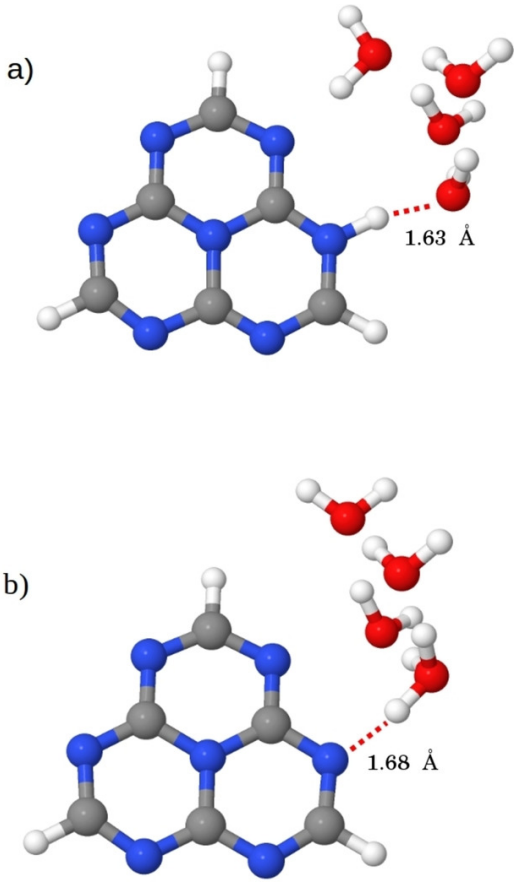

Figure 19: (a) Ground state equilibrium structure of the HzH$\cdots(H_2O)_4$ complex. (b) Ground state equilibrium structure of the Hz$\cdots H_3O(H_2O)_3$ complex.

The π-type SOMO of the HzH$\cdots(H_2O)_4$ complex at the ground-state equilibrium geometry is essentially the same as that of the free HzH radical. The LUMO of σ^* character of the HzH$\cdots(H_2O)_4$

complex is depicted in Figure 20. It is localized outside the water cluster and solvated by free OH bonds of water molecules in the second and third solvation shell. The $^2\pi\sigma^*$ state of HzH$\cdots$(H$_2$O)$_4$ is thus a spontaneously charge-separated state, consisting of a protonated Hz molecule and a finite-size solvated electron.

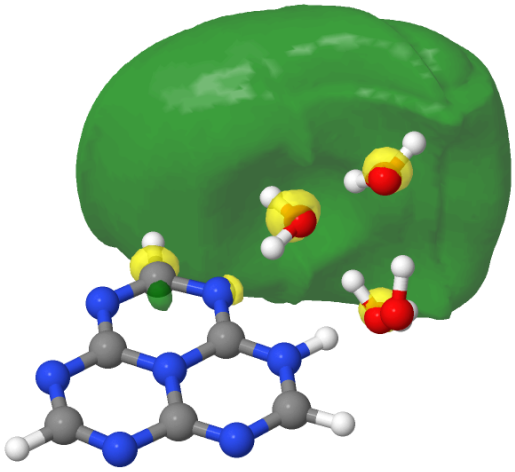

Figure 20: LUMO of the HzH$\cdots$(H$_2$O)$_4$ complex at its ground state equilibrium structure.

The vertical excitation energies of the HzH$\cdots$(H$_2$O)$_4$ complex are listed in the third column of Table 5. The $^2\pi\pi^*$ vertical excitation energies of the HzH chromophore are only weakly affected by the aqueous microenvironment. The $^2\pi\sigma^*$ excited state is blue shifted by about 0.30 eV in HzH$\cdots$(H$_2$O)$_4$ relative to HzH.

The energy profiles of the relaxed scan for H-atom transfer from HzH to the (H$_2$O)$_4$ cluster are displayed in Figure 21. The rearrangement of the nuclear geometry by minimization of the $^2\pi\sigma^*$ energy raises the energies of the D$_0$ state and the $^2\pi\pi^*$ states at short NH distances ($R_{\mathrm{NH}} \approx$ 1.0 Å). At large NH distances ($R_{\mathrm{NH}} \approx$ 1.7 Å), the energies of these states are stabilized with respect to the HzH$\cdots$H$_2$O complex by more than 0.5 eV. As a result, the PE profiles of the D$_0$ state and the $^2\pi\pi^*$ states of HzH$\cdots$(H$_2$O)$_4$ (Figure 21) are considerably flattened in comparison with HzH$\cdots$H$_2$O (Figure 18) which reflects the stabilization of the ionic D$_0$ and $^2\pi\pi^*$ states by the water cluster. The energy profile of the $^2\pi\sigma^*$ state is more repulsive in the HzH$\cdots$(H$_2$O)$_4$ complex than in the HzH$\cdots$H$_2$O complex due to a slight destabilization of the $^2\pi\sigma^*$ energy at short NH distances and a slight stabilization at large NH distances (see Figure 21). Remarkably, all crossings of the $^2\pi\sigma^*$ energy with the energies of the lower-lying states (D$_0$, D$_1$, D$_2$) have been eliminated by the larger water environment.

The formation of the Hz$\cdots$H$_3$O(H$_2$O)$_3$ complex from the $^2\pi\sigma^*$ excited state of the HzH$\cdots$(H$_2$O)$_4$ complex is found to be a barrierless adiabatic PCET reaction without perturbation by energy crossings, in remarkable contrast to the H-atom photodetachment reaction from HzH (Figure 14).

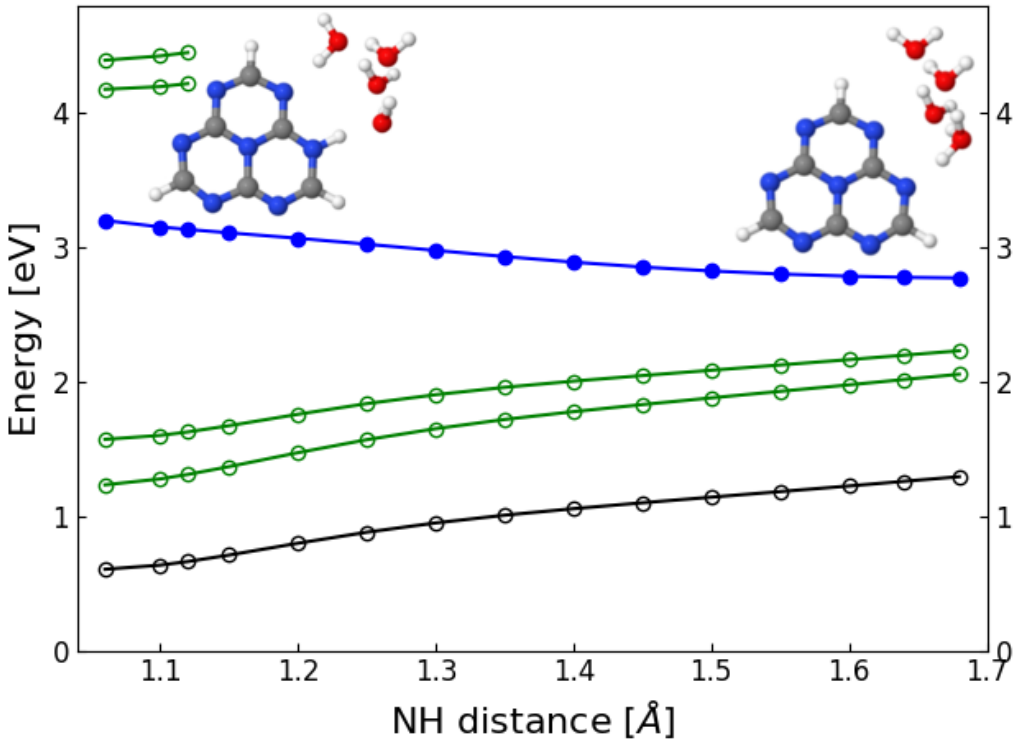

Figure 21: Energy profiles of the relaxed scan of the HzH$\cdots$$(H_2O)_4$ complex along the NH-stretching coordinate. The minimum-energy path is optimized in the $\pi\sigma^*$ state at the UMP2 level. Energies are calculated with the CASPT2 method at the UMP2-optimized geometries. Black: electronic ground-state; green: $\pi\pi^*$ states; blue: $\pi\sigma^*$ state. Full circles indicate that the reaction path geometry was optimized in this state; open circles indicate that the reaction path geometry was optimized in a different state.

Figure 22 shows the same energy profiles as in Figure 21, but with inclusion of macroscopic electronic solvation effects with the polarized continuum model. The PE functions become even flatter than in the isolated HzH$\cdots$$(H_2O)_4$ complex. The stabilization energy of the $^2\pi\sigma^*$ state due to H-atom transfer is reduced to 0.16 eV. The energy-gap between the $^2\pi\sigma^*$ state and the D_2 state increases to 1.95 eV at large NH distances.

The energy of dissociation of the Hz$\cdots$$H_3O(H_2O)_3$ complex into Hz and $H_3O\cdots(H_2O)_3$ is computed as 0.67 eV with C_s symmetry constraint. When the symmetry constraint is relaxed for the free $H_3O(H_2O)_3$ radical, the dissociation energy increases to 0.79 eV. The binding energy of the Hz$\cdots$$H_3O(H_2O)_3$ product is thus larger than the excess energy of the PCET reaction in the $^2\pi\sigma^*$ state. When the HzH$\cdots$$(H_2O)_4$ complex is excited to the D_4 or D_5 states, followed by radiationless relaxation to the D_3 ($\pi\sigma^*$) state, the excess energies of the radiationless decay and the PCET reaction in the $^2\pi\sigma^*$ state together are sufficient to allow the dissociation of the complex into Hz

and $H_3O(H_2O)_3$, that is, the formation of a free hydrated electron.

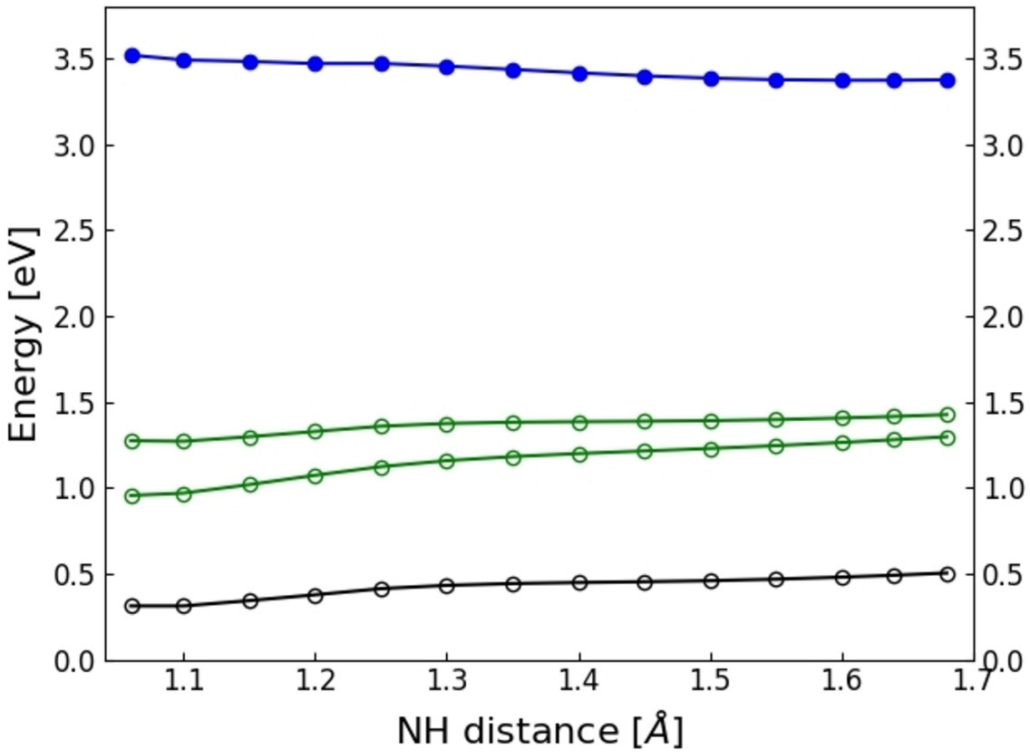

Figure 22: Energy profiles of the relaxed scan of the $HzH\cdots(H_2O)_4$ complex along the NH-stretching coordinate. The minimum-energy path is optimized in the $\pi\sigma^*$ state at the UMP2 level. Energies are calculated at the UMP2-optimized geometries with the CASPT2 method including a polarizable continuum. Black: electronic ground-state; green: $\pi\pi^*$ states; blue: $\pi\sigma^*$ state. Full circles indicate that the reaction path geometry was optimized in this state; open circles indicate that the reaction path geometry was optimized in a different state.

4.4 Discussion

It is interesting to compare the H-atom photodetachment reaction in HzH and the excited-state H-atom transfer reaction in $HzH\cdots(H_2O)_n$ complexes with the corresponding reactions in typical closed-shell photoacids and their hydrogen-bonded complexes with water molecules, because a large amount of experimental and computational data is available for closed-shell photoacids, whereas experimental data for open-shell photoacids like PyH, PmH or HzH are extremely scarce. The kinetic energy distributions of H-atoms photodetached from pyrrole, phenol, indole, thiophenol, etc., were extensively investigated with velocity map imaging, multimass ion

imaging, Rydberg tagging and femtosecond spectroscopy experiments, see [130, 143–147] for representative examples. These experimental studies were supported by *ab initio* calculations of the relevant PE surfaces and by calculations of the nonadiabatic time-dependent quantum wave-packet dynamics, e. g. [148–154] or quasi-classical trajectory surface-hopping simulations, e. g. [155–160]. For phenol$\cdots(NH_3)_n$, phenol$\cdots(H_2O)_n$ and pyrrole$\cdots(NH_3)_n$ complexes, it was experimentally established that PCET from photoexcited pyrrole or phenol to the solvent molecules is the dominant process,[161–164] rather than proton transfer, as previously thought.[165, 166]
The shape of the diffuse σ^* orbital located on the NH group of HzH is similar to the shape of the σ^* orbitals of pyrrole, phenol and indole.[127] Upon extension of the NH or OH bond of these photoacids, the σ^* orbital collapses to the compact 1s orbital of the free H-atom, which is the reason for the pronounced stabilization of the $\pi\sigma^*$ energy by NH or OH bond stretching.[127] The vertical electronic excitation spectrum of HzH exhibits similarities with the excitation spectrum of indole (two absorbing $\pi\pi^*$ states, followed by a dark $\pi\sigma^*$ state),[167] but the excitation energies of HzH are much lower, as expected for a radical. The PE crossings along the NH stretching coordinate in HzH also are qualitatively similar to indole, but are located at much lower electronic excitation energies. While the vertical excitation energies of the L_a, L_b states of indole are ≈4.5 eV, the excitation energies of the D_1, D_2 states of HzH are 1.3 -1.4 eV. The vertical excitation energy of the $\pi\sigma^*$ state of indole is about 5.0 eV, while it is about 3.3 eV in HzH. The energy of the $^1\pi\sigma^*$-S_0 energy crossing is at ≈4.6 eV in indole, while the energy of the $^2\pi\sigma^*$-D_0 crossing is at ≈2.7 eV in HzH. The photodissociation of HzH can thus be driven by near-UV photons (≈3.5 eV, the vertical excitation energy of the D_4 state), whereas the excitation threshold for photodissociation of indole is 1.5 eV higher (≈5.0 eV).
The electronic structure of the $^2\pi\sigma^*$ state of the HzH$\cdots(H_2O)_4$ complex is analogous to that found for the indole$\cdots(H_2O)_n$ or phenol$\cdots(H_2O)_n$ complexes.[168, 169] In particular, the expulsion of the σ^* orbital in the HzH$\cdots H_2O$ complex (Figure 17 (a)) is similar to that found in the indole$\cdots H_2O$ and phenol$\cdots H_2O$ complexes. The σ^* orbital of the $\pi\sigma^*$ excited state of HzH is squeezed out of the chromophore-water complex due to the strong and short hydrogen bonds between HzH and the water molecules and the electrophobic character of the H_2O molecule.[127] Compared to the $S_1(\pi\pi^*)$ state in the phenol$\cdots H_2O$ complex, the $D_1(\pi\pi^*)$ and $D_2(\pi\pi^*)$ states in the HzH$\cdots H_2O$ complex are much lower in energy and the $^2\pi\sigma^*$ - $^2\pi\pi^*$ energy crossing occurs at much larger bond distances. Like in phenol$\cdots(H_2O)_n$ complexes,[167, 169] the conical intersection of the energy of the $\pi\sigma^*$ state with the energy of the electronic ground-state along the H-atom detachment coordinate, which exists in free phenol and free HzH, is eliminated in the HzH$\cdots H_2O$ and HzH$\cdots(H_2O)_4$ complexes. Phenol and indole are known as photoacids with a comparatively high yield of hydrated electrons when excited to their S_1 or S_2 states.[170, 171] It

can be expected that the absence of crossings of the $^2\pi\sigma^*$ energy with the energies of lower-lying electronic states in the HzH$\cdots$(H$_2$O)$_4$ complex likewise may result in a relatively high branching ratio for the formation of the of H$_3$O(H$_2$O)$_3$ radical.

The $^2\pi\sigma^*$ state of HzH can be populated by near-UV light either directly (due to vibronic intensity borrowing from allowed $^2\pi\pi^*$ states) or indirectly (by radiationless decay from the dense manifold of higher $^2\pi\pi^*$ states). The photodissociation of isolated HzH involves conical intersections of the $^2\pi\sigma^*$ state with two closely spaced low-lying $^2\pi\pi^*$ states and with the D$_0$ state, see Figure 14. At these conical intersections, a bifurcation of the nuclear dynamics will occur. Diabatic passage through the intersections leads to the detachment of free H-atoms, while adiabatic passage transfers the $^2\pi\sigma^*$ population to the bound $^2\pi\pi^*$ states and the D$_0$ state, which ultimately leads to relaxation to the energy minimum of the D$_0$ state, that is, aborted photodissociation. This kind of nonadiabatic photodissociation dynamics was investigated in a reduced-dimensional *ab initio* wave-packet dynamics study for the PyH radical, in which the PE function for NH dissociation in the $^2\pi\sigma^*$ state crosses the energy of a bound low-lying $^2\pi\pi^*$ state as well as the energy of the D$_0$ state. Dissociation yields of 33-90% were predicted for this system, depending on the initial preparation of the wave packet in the $^2\pi\sigma^*$ state.[172] The conical intersections thus act as quenchers of the photodissociation yield of the PyH radical.

As discussed above, the PE functions for H-atom transfer in the HzH$\cdots$H$_2$O complex differ substantially from those for the photodetachment reaction in isolated HzH. Comparing Figure 14 and Figure 18, it is seen that the PE function of the $^2\pi\sigma^*$ state is less repulsive in the HzH$\cdots$H$_2$O complex and the energies of the $^2\pi\pi^*$ states and the D$_0$ state are substantially lowered at large NH distances due to the formation of the strongly bound H$_3$O$^+$ cation. The conical intersection of the $^2\pi\sigma^*$ state with the D$_2$($\pi\pi^*$) state is shifted from an NH distance of $\approx$1.4 Å to $\approx$1.7 Å and the conical intersection with the D$_0$ state is eliminated altogether. When three more water molecules are added, the driving force for dissociation in the $^2\pi\sigma^*$ state slightly increases and the energies of the $^2\pi\pi^*$ states and the D$_0$ state are additionally lowered by about 0.6 eV at large NH distances (see Figure 21). The approximate inclusion of the effect of a macroscopic aqueous environment results in a further significant increase of the energy-gap between the $^2\pi\sigma^*$ state and the lower-lying $^2\pi\pi^*$ and D$_0$ states at large NH distances (Figure 22). As a result, all conical intersections which are involved in the photodissociation of the free HzH radical along the NH dissociation coordinate are eliminated in the HzH$\cdots$(H$_2$O)$_4$ complex.

Although the energy of the ionic Hz$^-\cdots$H$_3$O$^+$(H$_2$O)$_n$ ground state is lower than the energy of the neutral Hz$\cdots$H$_3$O(H$_2$O)$_n$ radical, the relatively large energy gap between these states suppresses the nonadiabatic back-transfer of the electron to an extent that the separation of the H$_3$O(H$_2$O)$_n$ cluster from the Hz molecule can efficiently compete with the quenching of the excited state by

electron back-transfer, which may result in a reasonably high quantum yield of formation of the hydrated electron. This conjecture should be confirmed by *ab initio* nonadiabatic dynamics simulations which, however, are challenging because of the electronic open-shell character of the $HzH\cdots(H_2O)_n$ system. This section has, been published, see [131].

5 Reaction of CO_2 with $H_3O(H_2O)_n$ Clusters (n=0,3,6)

5.1 Introduction

In 2014, Hamers and coworkers reported the reduction of CO_2 in aqueous solution with hydrated electrons, using diamonds and diamond nanoparticles, or iodide anions as sources of the hydrated electrons.[51, 133] The formed product was CO with 90% selectivity, but neither the kinetics nor the mechanism were explored. In 2020, Rybkin performed a computational study on the mechanism of aqueous carbon dioxide reduction by the solvated electron.[173] He identified a distinct intermediate and a transition-state region in the CO_2 reduction reaction with the hydrated electron. Rybkin characterized the transition state by a displacement of the CO_2 towards the cavity of the electron. Interestingly, the energy profile of a one-dimensional relaxed scan with respect to the OCO bending angle exhibited no barrier. The reaction was reported to take place on a picosecond timescale. Bu and coworkers investigated a related problem, the time evolution of an excess electron in heterogenous CO_2-H_2O systems.[174] It was reported that the excess electron located on the CO_2 molecule within 80 fs after its addition to the CO_2-H_2O cluster. This result is in contrast to the results of Rybkin insofar as the timescale differs by more than one order of magnitude.

This study aims to contribute to the understanding of CO_2 reduction with hydrated electrons, using the hydrated H_3O radical as a finite-size model for the hydrated electron.

5.2 Computational Methods

The UMP2 method was used to determine the structure and reaction paths of the $H_3O(H_2O)_n$ and $H_3O(H_2O)_n\cdots CO_2$ clusters (n=0,3,6).[90] The inclusion of dynamic correlation by UMP2 yields more accurate results than the CASSCF method with respect to weak long-range interactions such as hydrogen-bonds.

The PCET reaction in the $H_3O(H_2O)_n\cdots CO_2$ clusters (n=0,3,6) involves the breaking and formation of multiple bonds. Further, all systems are open-shell systems, making them prone to instabilities of the UHF solution. Therefore, the CASPT2 method based on the multi-configuration CASSCF method was used to assure the accuracy of the UMP2 results. The active space of the CASSCF calculations comprised 5 electrons in 6 orbitals (5,6). The orbitals were selected based on their energy in a UHF calculation; the three highest occupied as well as the three lowest unoccupied orbitals were chosen. A compact active space is sufficient for the computation of the energy surface of the electronic ground-state.

CASPT2 energies computed at geometries optimized at the UMP2 level will be referred to as UMP2//CASPT2. UMP2 energies at UMP2 optimized geometries will analogously be refered to as UMP2//UMP2.
The UADC(2) and CASPT2 methods were employed for the calculation of vertical excitation energies of the $H_3O(H_2O)_n$ clusters (n=0,3,6). The active space for the CASSCF calculations was extended to comprise 7 electrons in 8 orbitals (7,8). The orbtials were selected based on their energy in a UHF calculation; the four highest occupied as well as the four lowest unoccupied orbitals were chosen. This extension was necessary for the accurate calculation of the energies of four states (ground state and the first three excited states). In the CASSCF calculations, the orbitals were averaged over those four states with equal weights.
Dunning's aug-cc-pVDZ basis set was employed for all atoms.[121] The augmentation is necessary to fully describe the $H_3O(H_2O)_n$ clusters as the SOMO is a diffuse Rydberg orbital. No symmetry constraints were imposed in these calculations.
One-dimensional relaxed scans of the PE surface of the electronic ground-state of the $H_3O(H_2O)_n\cdots CO_2$ clusters (n=0,3,6) were constructed. The distance between the O atom of CO_2 and its closest H atom from a water molecule was used as the reaction coordinate for these relaxed scans. For fixed OH-distances, the energy of the ground-state was optimized with respect to all other internal degrees of freedom. As was shown in Section **3**, the OCO bending angle is an essential coordinate for the CO_2 reduction reaction. Therefore, additional one-dimensional relaxed scans with respect to the OCO bending angle have been constructed. For this purpose, the OH-distance was set to its value just before the transfer of an electron to CO_2 happened. This construction of two one-dimensional relaxed scans rather than a two-dimensional scan reduces the computational cost significantly.
The TURBOMOLE program package (V 6.3.1)[140] was employed for the UMP2 and UADC(2) calculations, making use of the resolution-of-the-identity (RI) approximation. The OpenMolcas program package (V 18.09)[122] was used for the CASSCF and CASPT2 calculations.

5.3 Results

5.3.1 SOMOs and Vertical Excitation Energies of $H_3O(H_2O)_n$ Clusters (n=0,3,6)

Before discussing the excitation energies of the $H_3O(H_2O)_n$ clusters (n=0,3,6), we briefly discuss their structures. These are shown with their respective SOMO in Figure 23.
The H_3O molecule shown in Figure 23 (a) has C_{3v} symmetry and the SOMO is directly attached to the H_3O^+ cation resulting in a low dipole moment of 0.6652 D. When adding the first solvation

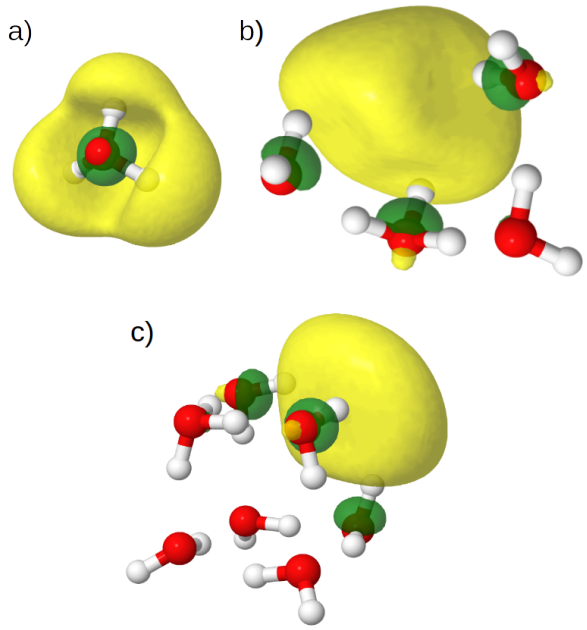

Figure 23: SOMOs of the H_3O radical (a), the $H_3O(H_2O)_3$ cluster (b) and the $H_3O(H_2O)_6$ cluster (c).

shell, ($H_3O(H_2O)_3$), multiple configurations are possible. Here a low-symmetry species (C_1 symmetry) is considered (Figure 23 (b)). The SOMO is spatially separated from the H_3O^+ cation by the three water molecules of the first solvation shell, increasing the dipole moment to 4.4137 D. By adding the second solvation shell, ($H_3O(H_2O)_6$), the number of possible configurations increases significantly. Once again, a single configuration was chosen to calculate the vertical excitation energies. The structure is shown in Figure 23 (c). This configuration is reminiscent of a cube, where each of the seven O atoms occupies a corner and the unpaired electron occupies the vacant corner. The second solvation shell further increases the spatial separation of the unpaired electron from the H_3O^+, increasing the dipole moment to 10.8632 D. This trend continues when more solvation shells are added[70] (not pursued in this work).

The vertical excitation energies and oscillator strengths of the $H_3O(H_2O)_n$ (n=0,3,6) clusters at the UADC(2) and CASPT2 levels are shown in Table 6. Overall, the calculated energies at the UADC(2) level are in good agreement with the CASPT2 results with differences below 0.1 eV. When comparing the three cluster sizes, it can be observed that the excitation energies decrease with increasing cluster-size. The oscillator strengths are also in good agreement between the two methods. Appart from the D_1 state of the $H_3O(H_2O)_6$ cluster at the UADC(2) level, all oscillator strengths are fairly high (> 0.100), indicating strong absorption. Considering that the maximum of the absorption spectrum of the hydrated electron is near 2.0 eV[52], the results for n=3 and n=6 seem to underestimate the excitation energy. However, upon placement of the $H_3O(H_2O)_n$ cluster

in bulk water, it is expected that the SOMO is compressed, causing a blue-shift of the excitation energies.

Table 6: Vertical excitation energies (in eV) and oscillator strengths (in parentheses) of $H_3O(H_2O)_n$ (n=0,3,6) clusters at the UADC(2) and CASPT2 levels.

$H_3O(H_2O)_n$	state	UADC(2)	CASPT2
$n = 0$	D_1	2.11 (0.309)	2.03 (0.317)
	D_2	2.27 (0.306)	2.34 (0.295)
	D_3	3.96 (0.185)	4.04 (0.150)
$n = 3$	D_1	1.43 (0.261)	1.48 (0.323)
	D_2	1.81 (0.205)	1.85 (0.238)
	D_3	1.88 (0.265)	1.92 (0.330)
$n = 6$	D_1	1.08 (0.070)	1.06 (0.178)
	D_2	1.46 (0.192)	1.40 (0.253)
	D_3	1.62 (0.170)	1.64 (0.231)

5.3.2 The $H_3O\cdots CO_2$ Complex

The $H_3O\cdots CO_2$ cluster is the simplest model for the investigation of the PCET reaction from H_3O to CO_2. The $H_3O\cdots CO_2$ cluster is the educt of the PCET reaction, whereas the $H_2O\cdots HOCO$ cluster is the product.

The educt geometry of the $H_3O\cdots CO_2$ cluster with its SOMO is shown in Figure 24 (a). At this geometry, a hydrogen bond exists between the H_3O radical and CO_2 molecule. The bond length of 2.52 Å indicates a weak hydrogen bond. The CO_2, the reactive H atom as well as the O atom of H_3O all lie in a plane, resulting in overall C_s symmetry for the system (no symmetry constraint was imposed), the remaining H atoms being mirror-symmetric to the plane.

The product geometry is shown in Figure 24 (b). In the product geometry, the *cis* HOCO radical is bonded to the water molecule by a strong hydrogen bond with a bond length of 1.74 Å. The SOMO is qualitatively the same as for the HOCO radical in Section **3** and explains the preference of the *cis* configuration over the otherwise more stable *trans* conformer. The free electron pair on the O atom of HOCO can form an additional hydrogen bond with the water molecule and the C atom lobe of the SOMO is located on the outside of the cluster, minimizing the repulsion with the free electron pair of the water O atom.

The PE profile of the one-dimensional relaxed scan along the OH distance at the UMP2//UMP2 level is shown in Figure 25 (a). For large OH distances, the energy does not increase significantly upon contraction of the OH distance until 1.6 Å. From 1.6 Å to 1.31 Å the energy increases by 0.5 eV and then drops nearly instantaneously to -1.25 eV at UMP2//UMP2 level. This sudden drop seems odd at first, as the PE profiles of relaxed scans usually are smooth functions. The reason for the sudden drop of the energy is the bending of the CO_2 molecule upon the transfer of the electron. As is well known, the bent configuration is more stable than the linear one for the CO_2^- anion.[123, 124] The energy profile of the one-dimensional relaxed scan along the OH distance at the UMP2//CASPT2 level is shown in Figure 25 (b). It is in very good agreement with the corresponding scan at UMP2//UMP2 level.

The energy profile of the one-dimensional relaxed scan with respect to the OCO bending angle at a fixed OH distance of 1.31 Å at the UMP2//UMP2 level is shown in Figure 26 (a). The energy profile indicates a low energy barrier along this scan. Local maxima along relaxed scans will be referred to as „apparent“ reaction barriers in the following. The profile of the corresponding one-dimensional relaxed scan at the UMP2//CASPT2 level is shown in Figure 26 (b). The UMP2//CASPT2 result indicates a small overestimation of the apparent barrier at the UMP2//UMP2 level. Taken together, the energy profiles of Figure 25 and Figure 26 suggest apparent reaction barriers of 0.74 eV and 0.61 eV at the UMP2//UMP2 and at UMP2//CASPT2 levels, respectively.

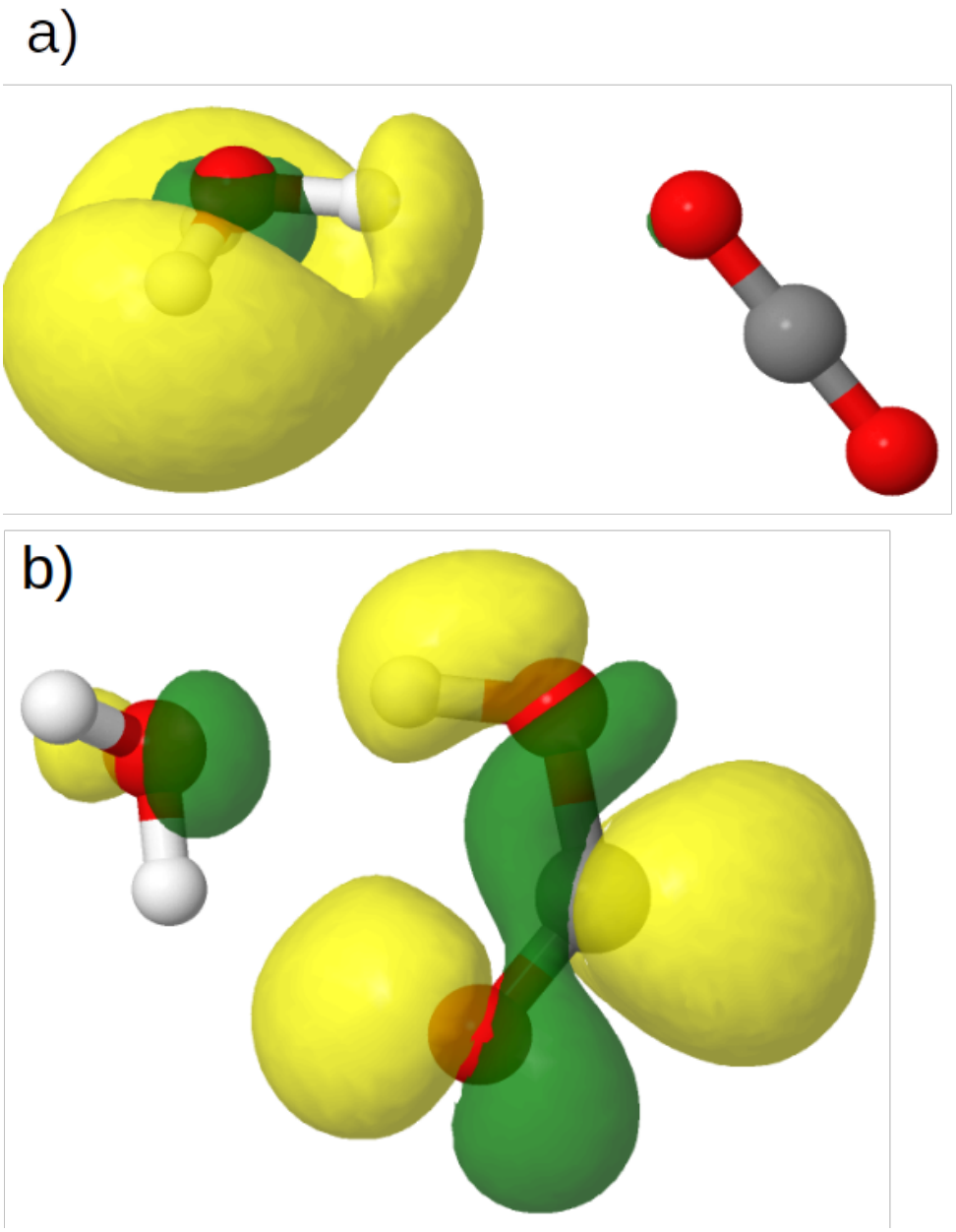

Figure 24: Educt (a) and product (b) geometry of the ground-state PCET reaction in the $H_3O\cdots CO_2$ cluster with their respective SOMO.

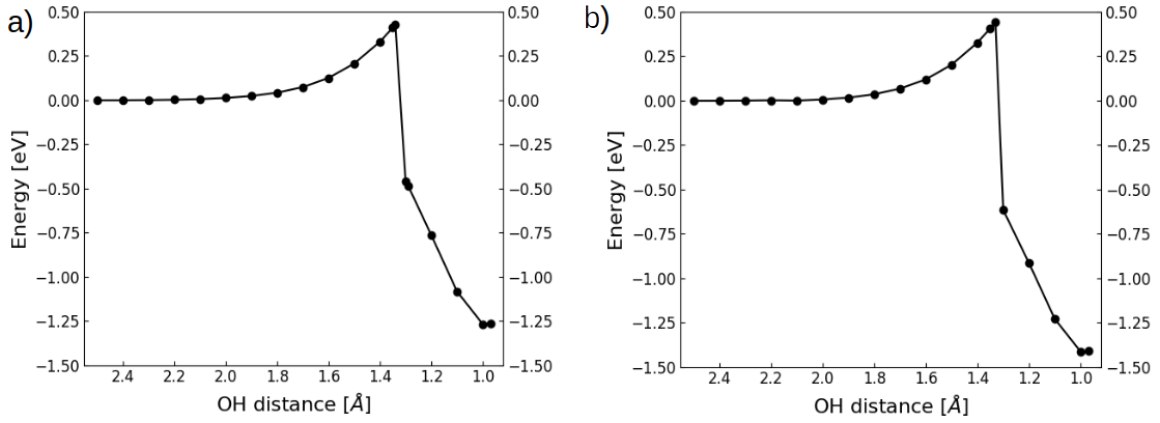

Figure 25: Energy profile of the relaxed scan along the H-atom transfer coordinate in the $H_3O\cdots CO_2$ complex at the UMP2//UMP2 (a) and UMP2//CASPT2 (b) levels. The energy is given relative to the energy of the educt geometry.

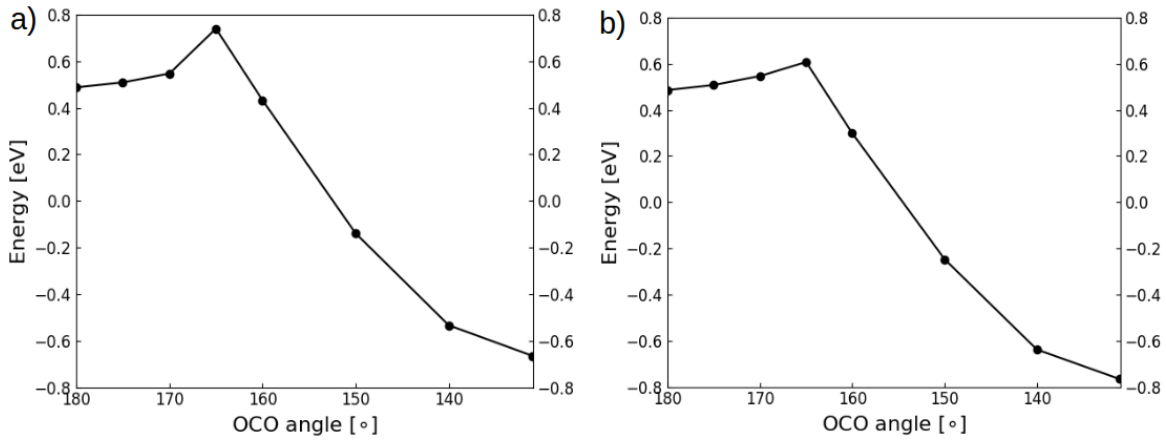

Figure 26: Energy profile of the relaxed scan of the $H_3O\cdots CO_2$ complex at UMP2//UMP2 (a) and UMP2//CASPT2 (b) level along the OCO bending angle at a fixed OH distance of 1.31 Å. The energy is given relative to the educt geometry.

5.3.3 The $H_3O(H_2O)_3\cdots CO_2$ Complex

By adding three water molecules to the $H_3O\cdots CO_2$ complex, the first solvation shell of the H_3O radical is formed. The educt geometry of the PCET reaction in the $H_3O(H_2O)_3\cdots CO_2$ complex is shown in Figure 27 (a). This geometry is reminiscent of the isolated $H_3O(H_2O)_3$ cluster in Figure 23 (b) with a CO_2 molecule added. The SOMO is enclosed by the molecules of this cluster. With a bond length of 2.00 Å, the hydrogen bond between CO_2 and the closest H atom is stronger than for the $H_3O\cdots CO_2$ complex. It should be noted that the H atom closest to CO_2 does not belong to H_3O^+, but rather to a water molecule of the solvation shell.
The product geometry, shown in Figure 27 (b), has the *trans* HOCO radical hydrogen-bonded to the $(H_2O)_4$ cluster with a very short hydrogen bond of 1.60 Å. Unlike for the $H_3O\cdots CO_2$ system, the *trans* conformer is the most stable product structure. This is explained by the electronic structure of the CO_2^- anion. The orbital lobe on the C atom is surrounded by water molecules and is stabilized by hydrogen bonds.
A one-dimensional relaxed scan along the OH bond (see Figure 27 (a)) has been constructed and the energy profile is shown in Figure 28 (a) at the UMP2//UMP2 level. The relaxed scan exhibits a significantly smaller apparent barrier than found for the $H_3O\cdots CO_2$ system. It exhibits a sudden decrease in energy at an OH distance of 1.63 Å. The OCO bending angle at this OH distance shrinks to at 173° due to the contraction of the cluster due to the reduced OH distance. The CO_2 molecule is not yet reduced at this OH distance. The sudden drop in energy for OH distances <1.63 Å is caused by the transfer of the electron to CO_2, forming the $H_3O^+(H_2O)_3\cdots CO_2^-$ complex with bent CO_2^-. Upon further reduction of the OH distance, a low secondary apparent barrier is observed before the energy decreases to a minimum at an OH distance of 1.0 Å. This secondary barrier is caused by the proton transfer from the H_3O^+ cation to the H_2O molecule donating the H atom. The relaxed scan along the OH bond length at the UMP2//CASPT2 level is shown in Figure 28 (b). It is in good agreement with the results at the UMP2//UMP2 level.
To obtain further insight, a second one-dimensional relaxed scan has been constructed at the UMP2//UMP2 level with respect to the OCO bending angle at a fixed OH distance of 1.63 Å. The energy profile is shown in Figure 29 (a). The initial slight decrease of the energy can partially be explained by the polarization of CO_2 by the water molecules, since the OCO angle before the electron transfer at an OH distance of 1.63 Å is already reduced to 173°. The further decrease of the OCO bending angle leads to the transfer of the electron and stabilization of the CO_2^- anion. No apparent barrier is observed in the energy profile of the relaxed scan with respect to the OCO bending angle. The profile of the one-dimensional relaxed scan along the OCO bending angle at the UMP2//CASPT2 level is shown in Figure 29 (b). It is in very good agreement with the results at the UMP2//UMP2 level.

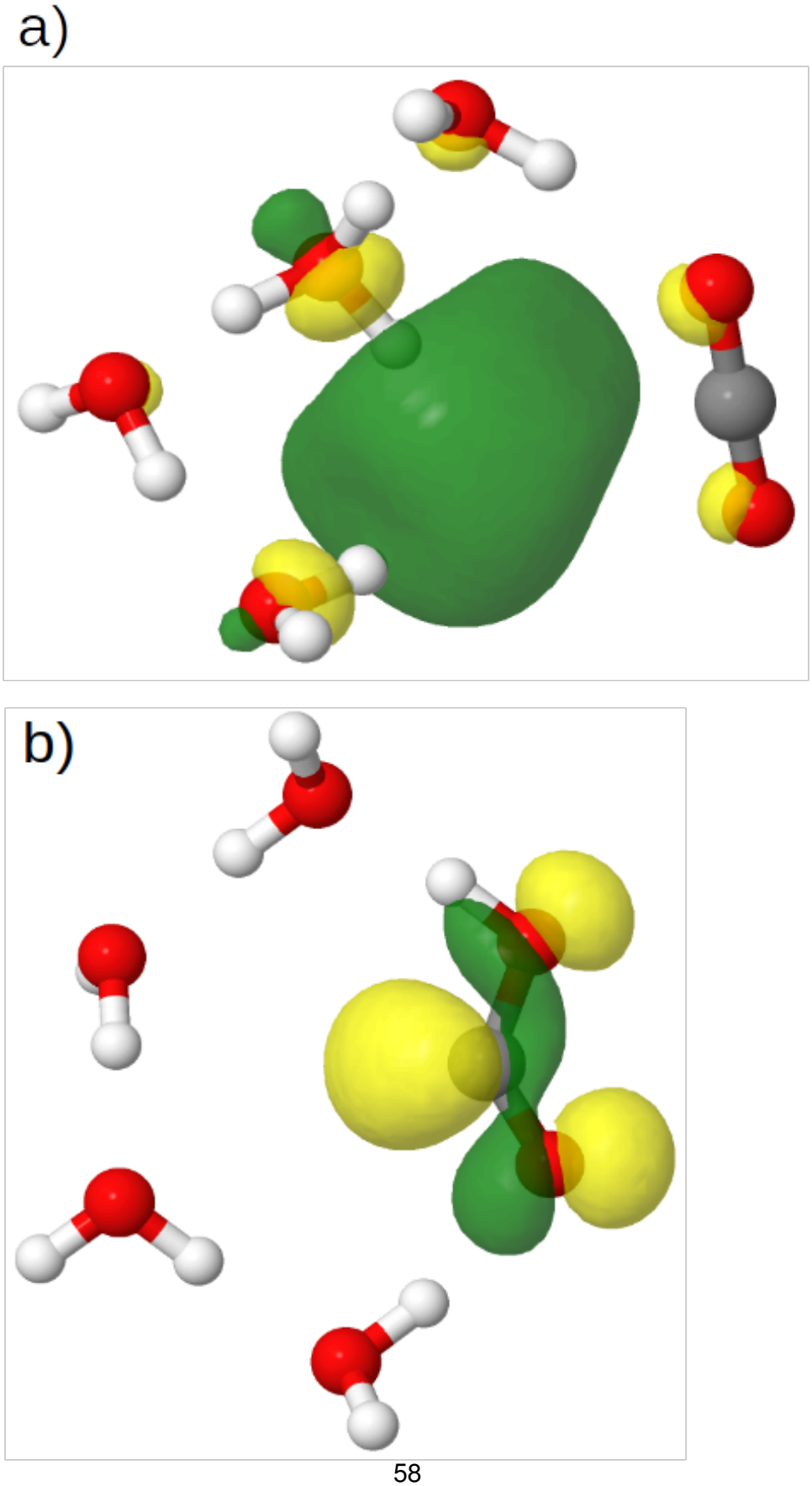

Figure 27: Educt (a) and product (b) geometry of the PCET reaction in the $H_3O(H_2O)_3 \cdots CO_2$ cluster with their respective SOMO.

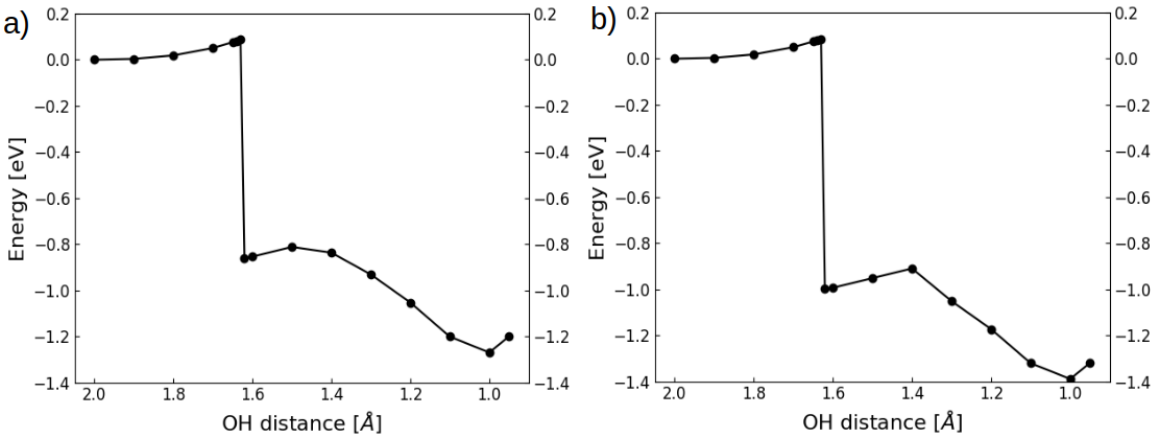

Figure 28: Energy profile of the relaxed scan along the H-atom transfer coordinate the $H_3O(H_2O)_3\cdots CO_2$ complex at UMP2//UMP2 (a) and UMP2//CASPT2 (b) level. The energy is given relative to the energy of the educt geometry.

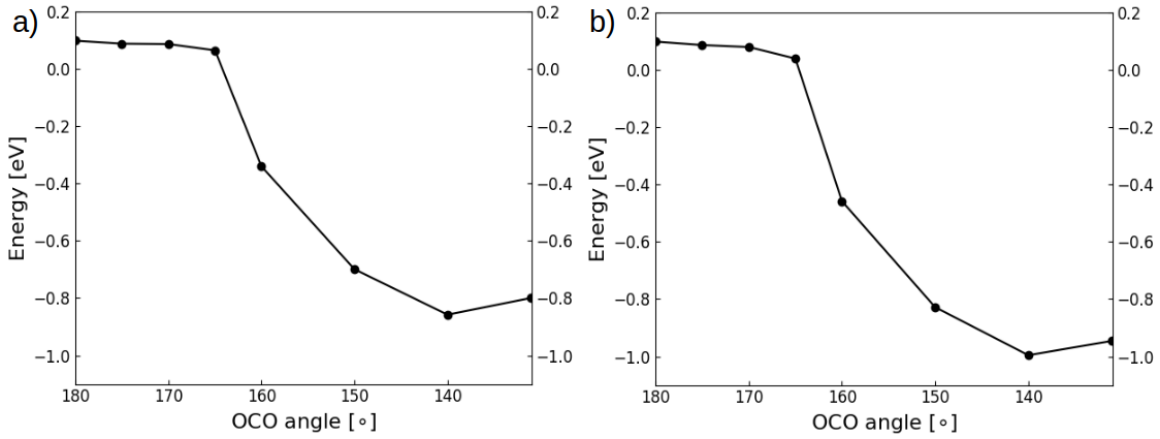

Figure 29: Energy profile of the relaxed scan along the OCO bending angle at a fixed OH distance of 1.63 Å the $H_3O(H_2O)_3\cdots CO_2$ complex at the UMP2//UMP2 (a) and the UMP2//CASPT2 (b) level along the OCO bending angle. The energy is given relative to the energy of the educt geometry.

The good agreement of the UMP2//UMP2 and UMP2//CASPT2 results in Figure 25, Figure 26 and Figure 28, Figure 29, respectively, justifies the use of the UMP2 method for this problem. Future MD simulations of the reaction of $H_3O\cdots(H_2O)_n$ clusters with CO_2 my be performed with the computationally efficient UMP2 method.
Taken together, the relaxed scans provide insight into the mechanism of the CO_2 reduction reaction in the $H_3O(H_2O)_3\cdots CO_2$ complex. With decreasing OH distance, first the electron is transferred, followed by a bending of the OCO angle. Then, a proton from H_3O^+ is transferred to the proton donating water molecule in the solvation shell. Finally, a proton from the newly formed H_3O^+ is transferred to the CO_2^- anion resulting in the $(H_2O)_4\cdots HOCO$ complex. The reaction is exothermic with an estimated reaction barrier of 0.1 eV.

5.3.4 The $H_3O(H_2O)_6\cdots CO_2$ Complex

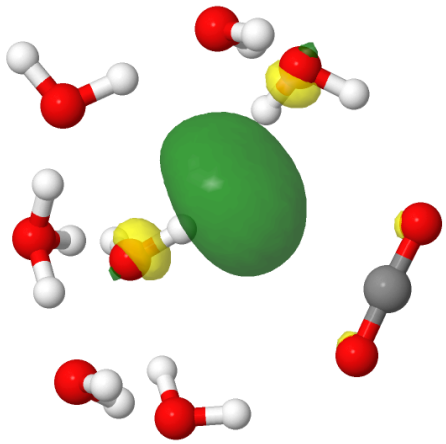

Figure 30: Educt geometry of the PCET reaction of the $H_3O(H_2O)_6\cdots CO_2$ cluster with its SOMO.

By adding three additional water molecules to the $H_3O(H_2O)_3\cdots CO_2$ complex, the second solvation shell around H_3O^+ is formed. In this work, two different starting geometries for the PCET reaction in $H_3O(H_2O)_6\cdots CO_2$ complexes were investigated which exhibit distinct features. The results for the first educt geometry are discussed in what follows. The results obtained for the second educt geometry are presented in appendix **A.2**.
The educt geometry of the $H_3O(H_2O)_6\cdots CO_2$ complex with its SOMO is shown in Figure 30. This local equilibrium geometry was selected because the SOMO is neighboring to the CO_2 molecule, which is analogous to the $H_3O\cdots CO_2$ and $H_3O(H_2O)_3\cdots CO_2$ complexes. This spatial proximity is expected to be favorable for the electron transfer. The SOMO is enclosed by water molecules and the CO_2 molecule. The SOMO is anti-bonding with respect to the OH bond of one water molecule in the first solvation shell. At first, analogous to the $H_3O(H_2O)_3\cdots CO_2$ complex, a proton from the

second solvation shell is transferred. The energy profile of the corresponding one-dimensional relaxed scan along the OH distance at the UMP2//UMP2 level is shown in Figure 31 (a). The

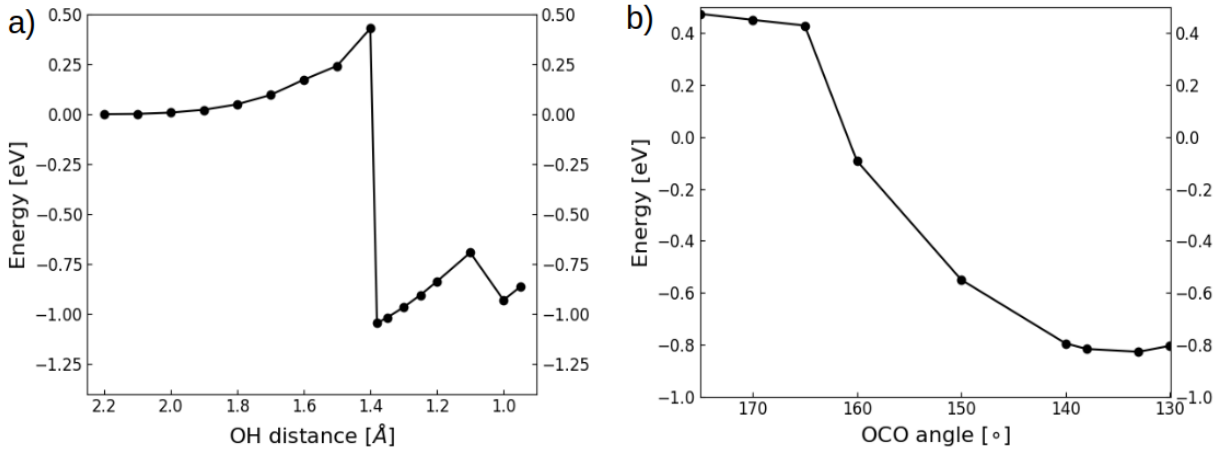

Figure 31: Energy profile of the relaxed scan of the first $H_3O(H_2O)_6\cdots CO_2$ complex at UMP2//UMP2 with respect to the OH distance (a) and the OCO bending angle at a fixed OH distance of 1.4 Å (b). The energy is given relative to the educt geometry.

left hand side of the scan represents the educt geometry, while the right hand side respresents the product geometry. As already observed for the previous systems, when the OH distance is decreased below 2.0 Å, the energy starts to increase rather steeply. At an OH distance of 1.4 Å, the characteristic sudden drop in energy is observed as the electron is transferred to the CO_2 molecule, causing it to bend which decreases the energy of the system. Further decreasing the OH distance transfers the proton while the energy of the system increases. This significant increase by around 0.3 eV can be explained by the geometry. As the proton is transferred, a $H_3O^+(H_2O)_5OH^-\cdots HOCO$ complex is formed which in total is neutral, but the proton transfer to form a $(H_2O)_7$ cluster has not yet occured. Decreasing the OH distance to values below 1.1 Å causes the proton to transfer and finally form the $(H_2O)_7\cdots HOCO$ cluster with a hydrogen bond length of 1.59 Å. The product geometry is shown in Figure 32 (b). The energy at this geometry is 0.93 eV below the energy at the educt geometry.

Notably, the local minimum in this relaxed scan is at an OH distance of 1.38 Å. At this geometry the electron has been transferred to CO_2, but the proton has not, forming a charge-separated $H_3O^+(H_2O)_6\cdots CO_2^-$ complex. The corresponding geometry and its SOMO are shown in Figure 32 (a). The SOMO is located on the CO_2^- anion but it still is rather diffuse and the largest lobe is surrounded by water molecules and „capped“ by H_3O^+ explaining the strong stabilization. At the geometry with a sucessfull H atom transfer to the CO_2 molecule, the $(H_2O)_7\cdots HOCO$ cluster, the SOMO is more contracted and the lobe on the C atom is marginally stabilized by the water molecules in the system.

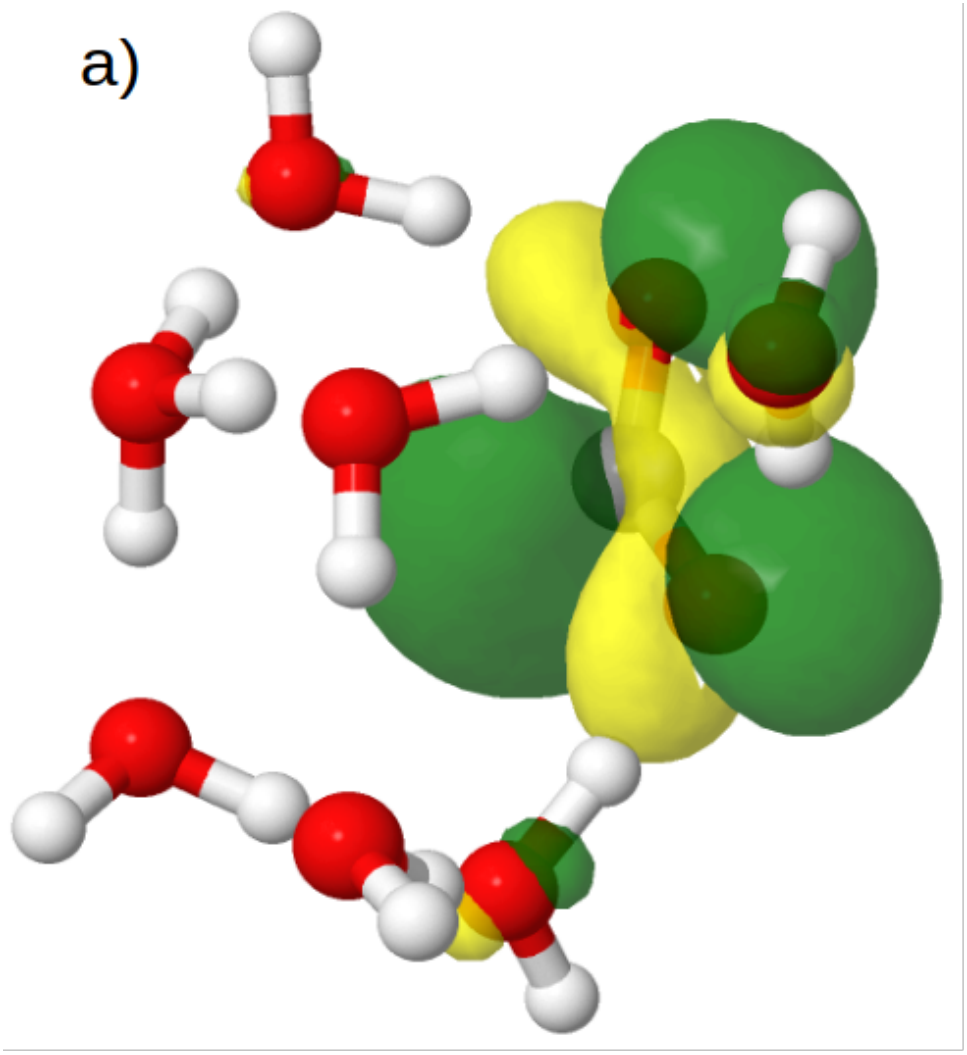
a)

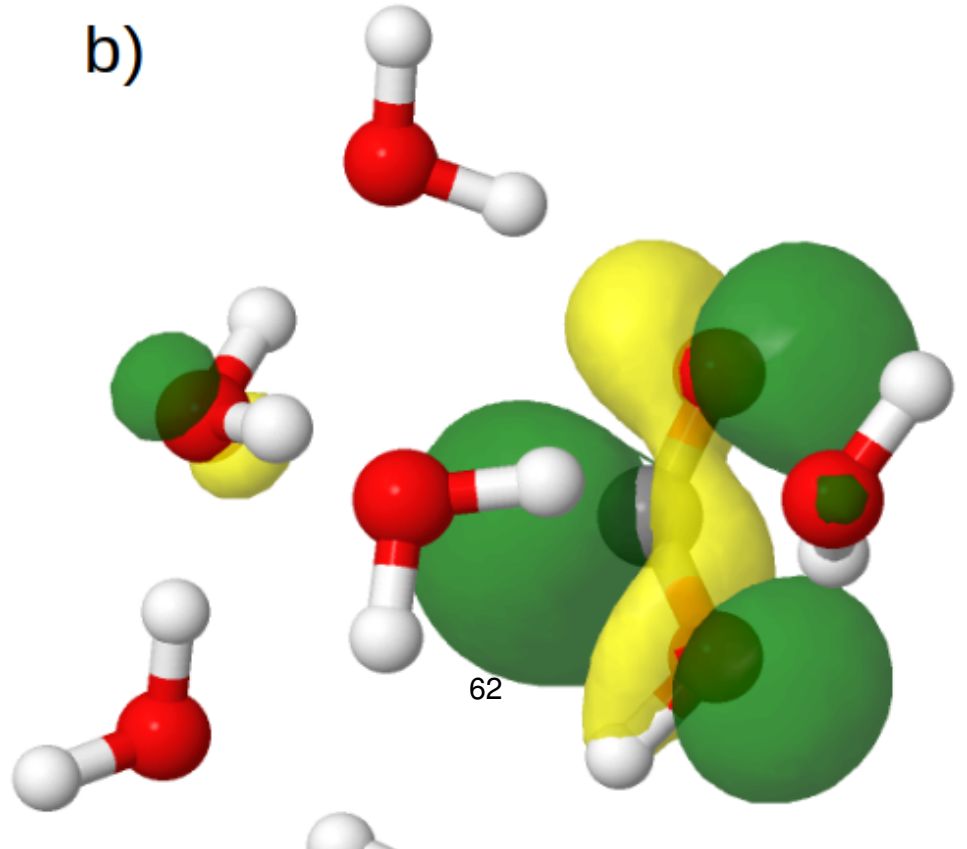
b)

Alternatively to the transfer of a proton from the second solvation shell, the transfer of a proton from the first solvation shell can occur as is shown in Figure 33 (a). In this case, the OH dis-

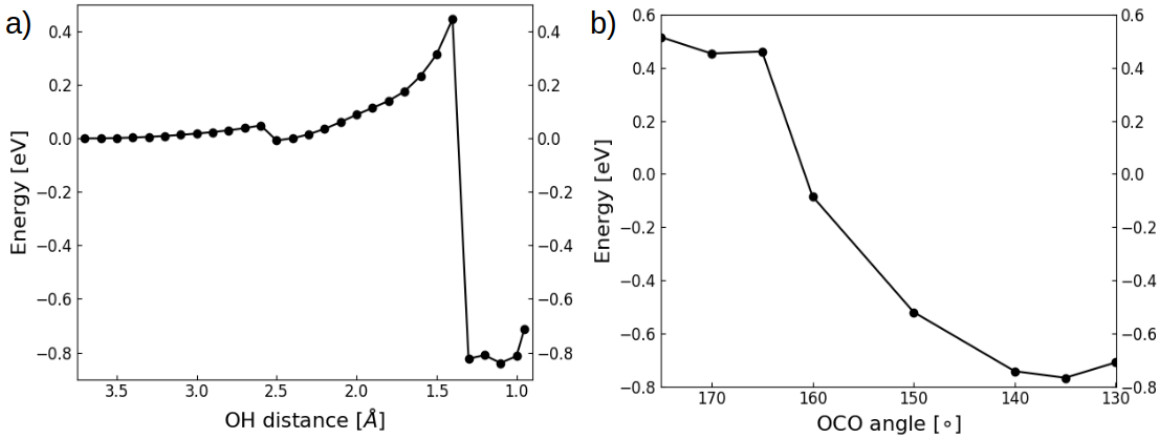

Figure 33: Energy profile of the relaxed scan of the $H_3O(H_2O)_6 \cdots CO_2$ complex at UMP2//UMP2 with respect to the OH distance (a) and the OCO bending angle at a fixed OH distance of 1.4 Å (b). The energy is given relative to the educt geometry.

tance is 3.68 Å and therefore larger at the educt geometry (left hand side Figure 33 (a)). Until an OH distance of 2.6 Å, the energy increases slightly followed by a slight dip of the energy at an OH distance of 2.5 Å. This effect is understood by an investigation of the electronic structure of the complex. The SOMO locates on the CO_2 molecule, forming the CO_2^- anion, but unlike for the previous systems, the OCO angle does not collapse to around 130°, but rather stays around 165°. Further decrease of the OH distance leads to an apparent barrier around an OH distance of 1.4 Å before the expected drop in energy occurs, where the electron fully locates on the CO_2 molecule and causes it to bend.

The energy profile of the relaxed one-dimensional scan for with respect to the OCO distance at a fixed OH distance (H atom from the first solvation shell) of 1.4 Å is shown in Figure 33 (b). At that OH distance the OCO angle is already bent at 168° which is the reason why the relaxed scan does not exhibit a local minimum at 180°. Around an angle of 168° a plateau in the energy is observed beyond which the energy strongly decreases upon further bending. In agreement with the previous results, a local minimum around an OCO bending angle of 135° is observed. The energy at this angle is 0.77 eV below the energy of the educt geometry.

The final OH distance is 1.06 Å and the energy of the product is 0.85 eV below the energy of the educt. The geometry of the product with its SOMO is shown in Figure 34. The observed maximum in the energy profile is 0.45 eV.

The comparison of the energy profiles of the two relaxed one-dimensional scans in Figure 31 (a) and Figure 33 (a) suggests that the selection of the proton which is to be transferred does not

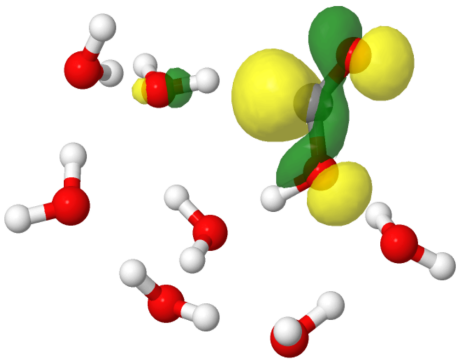

Figure 34: Geometry of the $(H_2O)_7\cdots HOCO$ cluster with its SOMO. In this reaction, the transferred proton has been taken from the first solvation shell.

make a significant difference.

5.4 Discussion

State-of-the-art electronic-structure calculations were performed to investigate the reaction of $H_3O(H_2O)_n$ clusters (n=0,3,6) with a CO_2 molecule in a finite size model of the reduction of CO_2 by hydrated electrons. The UMP2 method was used and verified in comparison with the CASPT2 method. Three different cluster sizes were selected to examine different geometric effects of the water molecules in the cluster on the reaction for these clusters. The reactions have been described by selecting two reaction coordinates and two one-dimensional scans along these reaction coordinates rather than constructing a two-dimensional relaxed map of the PE surface.
The observed mechanism follows the same scheme when the cluster size is increased. At first, the electron localises on the C atom of the CO_2 molecule. The transfer of the electron is followed by the bending of the CO_2^- anion. Next, a proton is transferred from the $H_3O^+(H_2O)_n$ cluster to the CO_2^- anion. For larger clusters, different pathways for the transfer of the proton exist.
The observed apparent barrier for the PCET reaction does not show a clear trend with respect to the system size. The apparent barrier deceases significantly from the $H_3O\cdots CO_2$ to $H_3O(H_2O)_3\cdots CO_2$ complex, but increases again in the $H_3O(H_2O)_6\cdots CO_2$ complex. The likely reason for this effect is the insufficient sampling of possible educt geometries of the clusters with two solvation shells. For the $H_3O(H_2O)_3\cdots CO_2$ and $H_3O(H_2O)_6\cdots CO_2$ complexes, the number of locally stable minima is so large that a systematic sampling was not possible in the present work. The focus of the present work is on gaining mechanistic insights and illustrating the effects for selected educt geometries, see the two different educt geometries for $H_3O(H_2O)_6\cdots CO_2$.
To judge the quality of the results for the $H_3O(H_2O)_6\cdots CO_2$ complexes (n=0,3,6), it is instructive

to compare with experimental data. One experimental approach to the investigation of the reduction of CO_2 by electrons in aqueous environments is the reaction of size-selected anionic water clusters with CO_2 molecules in a FT-ICR mass spectrometer. Beyer and coworkers[175] investigated the reaction of $(H_2O)_n^-$ clusters (n=2-61) with CO_2 using FT-ICR mass spectrometry and found a reaction enthalpy of -105$\pm$39 kJ/mol (-1.09 eV) for the CO_2 reduction recation to $CO_2^{\cdot-}$, which is in very good agreement with the results of the present work for the reaction of CO_2 with $H_3O(H_2O)_n$ clusters. The $H_3O(H_2O)_n\cdots CO_2$ complexes therefore seem to be good models for the explanation of the reaction enthalpy of the CO_2 reduction reaction.

Bartels and coworkers investigated the reduction of CO_2 by hydrated electrons generated by electron impact in water for a range of temperatures.[134] They reported that the rate constant for the reaction reaches a value of $k = 1.53 \pm 0.01 \cdot 10^{11}$ $M^{-1}s^{-1}$ at 300°C. The rate constant at room temperatur was reported to be $k = 8.91 \pm 0.11 \cdot 10^{9}$ $M^{-1}s^{-1}$. The activation energy was estimated as 15.9 kJ/mol (0.16 eV). This barrier is consistent with the low barrier predicted in the present work for the $H_3O(H_2O)_3\cdots CO_2$ complex (0.10 eV), although temperature effects were not explicitly included in the present work.

The structure of the HOCO radical product can further be compared with the structure of the HCO_2^- anion reported by Yang *et al.*[31] While the atomic composition is the same, the nuclear and electronic structure is not. The HCO_2^- anion possesses one additional electron and the H atom is bound to the C atom rather than to the O atom. Upon transfer of a second electron to the HOCO radical, it can be to the equilibrium structure of HCO_2^-.

Future extensions of the present work should improve on the sampling of educt geometries. This could be achieved with *ab initio* molecular dynamics studies at sufficiently low temperatures to avoid dissociation of the $H_3O(H_2O)_n\cdots CO_2$ complexes.

6 Dynamics Study of the Photogeneration of Hydrated H_3O Radicals in the $HzH_2\cdots(H_2O)_4$ Cluster

6.1 Introduction

In Section **4**, the PE surfaces of the $HzH\cdots(H_2O)_n$ (n=0,1,4) complexes were explored with respect to the H-atom transfer from HzH to a hydrogen bonded water cluster (H-atom detachment for n=0). This study provided a qualitative picture of the photo-induced H-atom transfer reaction in $HzH\cdots$water clusters of various sizes. However, no kinetic data about the timescale of the reaction or the quantum yield can be extracted from these results. We therefore performed nonadiabatic excited-state dynamics studies to obtain insights in these respects. The $HzH_2\cdots(H_2O)_4$ cluster has been selected as a model system for the calculations.

The dispropornation of HzH is exothermic. It can be assumed that the closed-shell HzH_2 molecule is a stable end product when HzH radicals are photogenerated. The $HzH_2\cdots(H_2O)_4$ complex is sufficiently large to allow for the formation of the first solvation shell of a H_3O radical product, increasing its stability. Further extensions of the water cluster to account for more solvation shells are computationally not feasible. The $HzH_2\cdots(H_2O)_4$ cluster therefore represents a good compromise between chemical relevance and computational effort.

6.2 Computational Methods

The MP2 and ADC(2) methods were emplyed in for this study.[91, 176–178] They are superior to the computationally less demanding DFT and TDDFT methods. In particular, TDDFT is unreliable for charge-transfer states which are crucial for this reaction.[179] The ground-state equilibrium geometry and the Hessian of the hydrogen bonded $HzH_2\cdots(H_2O)_4$ complex were determined with the MP2 method. Vertical excitation energies as well as oscillator strengths were calculated with the ADC(2) method.

Dunning's cc-pVDZ basis[121] has been employed for the HzH_2 chromophore, while the aug-cc-pVDZ basis[121] was employed for the water molecules. Benchmark calculations showed that no significant error is introduced for the excitation energies of the $HzH_2\cdots(H_2O)_4$ complex by omitting the diffuse basis functions on HzH_2. On the other hand, the diffuse basis functions are necessary for the water molecules to describe the diffuse LUMO of this complex as well as the diffuse SOMO of the $H_3O(H_2O)_3$ product. The computation time saved, on the other hand, is significant.

The MP2 and ADC(2) calculations were carried out with the TURBOMOLE program package[180] and the resolution-of-the-identity (RI) approximation[181] was applied.
The absorption spectrum was simulated with the nuclear ensemble method.[182] 1,500 phase-space points were sampled from the harmonic-oscillator Wigner distribution[183] at room temperature (298 K). Excitation energies and oscillator strenghts of the nine lowest excited electronic states were computed for these 1,500 sampling points. The resulting line spectrum is convoluted with a Gaussian function of 0.05 eV full width at half maximum (FWHM). The calculations of nuclear ensemble spectra were performed with the Newton-X package.[184]
The initial conditions for the excited-state dynamics simulations were selected from the above mentioned 1,500 points generated for the simulation of the absorption spectrum simulation by restricting the initial excitation energy to an energy window of 0.1 eV centered at the absorption band maximum at 4.54 eV. 226 trajectories were randomly selected within this window and propagated up to 100 fs with a time step of 0.5 fs. The LZSH algorithm[111, 185, 186] using the Belyaev-Lebedev formula[118] was employed with the ADC(2) electronic-structure method. The time step is reduced to 0.1 fs in the vincinity of adiabatic energy gap minima to ensure the correct calculation of the nonadiabatic transition probability.
As a single-reference based method, ADC(2) is not reliable at S_1-S_0 conical intersections. Therefore, trajectories were stopped when the S_1-S_0 gap dropped below 0.1 eV. In this case, the trajectory was attributed to the ground-state population for the remainder of the propagation time. This is a widely adopted procedure in non-adiabatic trajectory surface-hopping dynamic simulations based on single-reference methods.[112]
The reactive excited state in the $HzH_2\cdots(H_2O)_4$ complex is a diffuse $\pi\sigma^*$ state. The σ^* orbital is located outside the water-cluster. To identify the $\pi\sigma^*$ state, the spatial extension of the virtual orbital $\psi(x,y,z)$ which is occupied in the excited state has been estimated by evaluating $\int \psi^2(x,y,z)(x^2,y^2,z^2)dxdydz$. In each direction from the central N atom of the chromophore the integration is extended to 20 a.u. With this information, the adiabatic states are classified into three groups of quasi-diabatic states: compact low-lying $\pi\pi^*$ states, compact high-lying $\pi\pi^*/n\pi^*$ states and diffuse $\pi\sigma^*$ states. The latter group further can be divided into high- and low-lying states as multiple states located on the surface of the water cluster fullfill this criterion.
Dynamical maps have been constructed to visualize the geometries sampled by the trajectories with respect to the OH and NO distances which are the decisive reaction coordinates for the PCET reaction.

6.3 Results

6.3.1 Structure and Vertical Excitation Energies

The ground-state equilibrium geometry of a selected $HzH_2\cdots(H_2O)_4$ complex is shown in Figure 35. While this configuration is only one of many with respect to the positions and orientations of the water molecules, it is representative for the $HzH_2\cdots(H_2O)_4$ complexes. The OH distance of

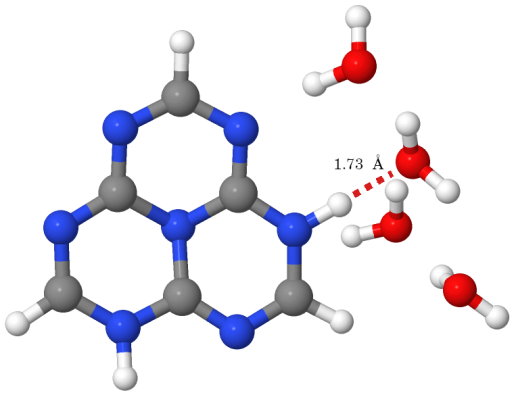

Figure 35: Ground-state equilibrium geometry of the $HzH_2\cdots(H_2O)_4$ at the MP2 level.

1.73 Å of the hydrogen bond of HzH_2 with the closest water molecule indicates a strong hydrogen bond. The O atoms of three water molecules lie more or less in a plane, while the fourth is located out of this plane. The out-of-plane displacement of the central N atom of the chromophore is in the same direction as the fourth water molecule. The MOs involved in the relevant excitations of the $HzH_2\cdots(H_2O)_4$ complex are displayed in Figure 36. These orbitals are the LUMO+3 (a), LUMO+2 (b), LUMO (c), HOMO (d) and HOMO-1 (e). The LUMO+1 is omitted in Figure 36 as it is not significantly involved in the CT state or the excited states with the highest oscillator strengths. The HOMO (d) is fully located on the HzH_2 chromophore, while the LUMO (c) is located outside of the water-cluster.

The vertical excitation energies, oscillator strengths and characters of the lowest nine singlet states of the HzH_2 molecule[187] and the $HzH_2\cdots(H_2O)_4$ complex are listed in Table 7. Although no symmetry restrictions were imposed in the calculation, the use of C_s symmetry labels is useful for a qualitative description. The vertical excitation energies of HzH_2 have already been discussed by Huang *et al.*[187] The two lowest excited states (S_1 and S_2) of the $HzH_2\cdots(H_2O)_4$ complex are local $\pi\pi^*$ excited states with low oscillator strengths. The S_2 state corresponds to the excitation from the HOMO (d) to the LUMO+2 (b) as shown in Figure 36. The S_3 state is a $\pi\sigma^*$ excited state which is anti-bonding with respect to one of the NH bonds of HzH_2. It is described by mixed HOMO-LUMO and HOMO-LUMO+3 configurations (see Figure 36 (d), (c) and (a) respectively). For the isolated HzH_2 molecule, the S_4 state is a $\pi\sigma^*$ state which is anti-bonding

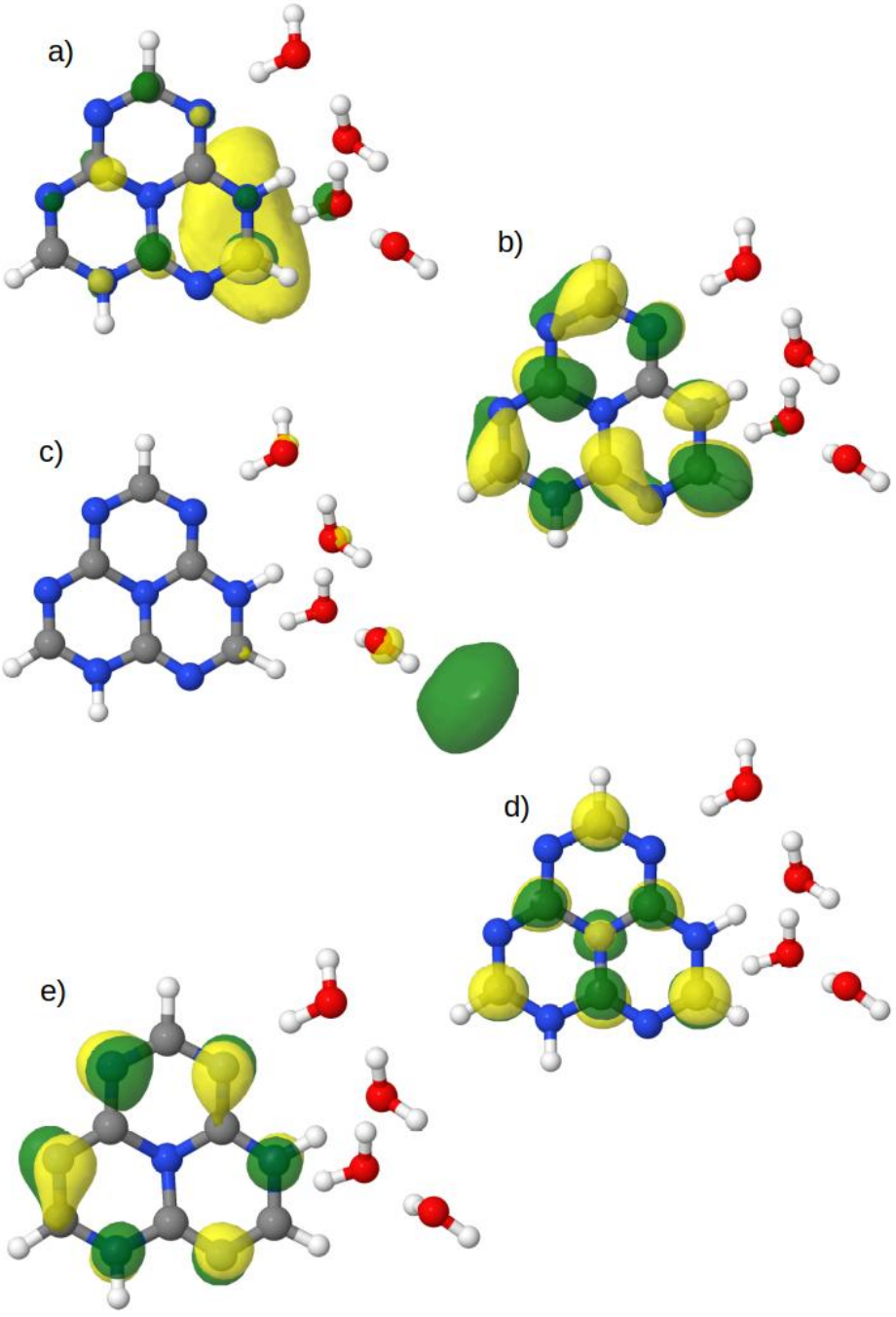

Figure 36: LUMO+3 (a), LUMO+2 (b), LUMO (c), HOMO (d) and HOMO-1 (e) of the $HzH_2\cdots(H_2O)_4$ complex at the ground-state equilibrium geometry.

Table 7: Vertical excitation energies (in eV), oscillator strengths (in parentheses) and characters (in brackets) of the lowest 10 singlet states of the HzH_2 molecule[187] and the $HzH_2\cdots(H_2O)_4$ complex at their respective ground-state equilibrium geometry at the ADC(2) level.

State	HzH_2	$HzH\cdots(H_2O)_4$
S_1	2.07 (0.071) [$\pi\pi^*$]	2.07 (0.069) [$\pi\pi^*$]
S_2	2.31 (0.113) [$\pi\pi^*$]	2.24 (0.130) [$\pi\pi^*$]
S_3	3.21 (0.002) [$\pi\sigma^*$]	3.76 (0.022) [$\pi\sigma^*$]
S_4	3.61 (0.002) [$\pi\sigma^*$]	4.05 (0.002) [$\pi\pi^*$]
S_5	4.08 (0.005) [$\pi\pi^*$]	4.24 (0.034) [$\pi\sigma^*$]
S_6	4.32 (0.002) [$n\pi^*$]	4.42 (0.010) [$\pi\sigma^*$]
S_7	4.35 (0.015) [$\pi\pi^*$]	4.49 (0.001) [$n\pi^*$]
S_8	4.66 (0.303) [$\pi\pi^*$]	4.60 (0.028) [$\pi\sigma^*$]
S_9	4.70 (0.004) [$\pi\sigma^*$]	4.72 (0.338) [$\pi\pi^*$]

with respect to the second NH bond. In the $HzH_2\cdots(H_2O)_4$ complex, the S_4 state is a $\pi\pi^*$ state which corresponds to the S_5 state of the isolated HzH_2 molecule. The S_5, S_6 and S_8 states of $HzH_2\cdots(H_2O)_4$ all correspond to $\pi\sigma^*$ states, in which different diffuse orbitals around the water cluster are populated. The S_7 state is a $n\pi^*$ state and corresponds to the S_6 state of isolated HzH_2. The S_9 state is a bright $\pi\pi^*$ state which arises from the transition from the HOMO-1 to the LUMO+2 ((e) and (b), respectively, in Figure 36). It should be noted that an additional $\pi\sigma^*$ state, which is anti-bonding with respect to the second NH bond in the $HzH_2\cdots(H_2O)_4$ complex, has been eliminated in the present calculations by the choice of the basis set.

The simulated absorption spectrum of the $HzH_2\cdots(H_2O)_4$ complex is shown in Figure 37. The spectrum exhibits two distinct peaks at 2.09 eV and 4.54 eV, respectively. The first peak can be attributed to the two low-lying $^1\pi\pi^*$ states. The absorption is red-shifted by about 0.15 eV with respect to the vertical excitation energies at the ground-state equilibrium geometry. Higher-lying $^1\pi\pi^*$ and $^1n\pi^*$ states give rise to the second absorption peak. The energy of this peak is red-shifted by 0.18 eV with respect to the vertical excitation energy of the S_9 state. Due to their low oscillator strengths, the $^1\pi\sigma^*$ states contribute only marginally to the absorption spectrum.

6.3.2 Nonadiabatic Excited-State Dynamics of HzH_2

Before investigating the nonadiabatic excited-state dynamics of the $HzH_2\cdots(H_2O)_4$ complex, it is instructive to have a look on the excited-state dynamics of isolated HzH_2. This was studied by Huang *et al.*[187] and therefore will be only briefly summarized in this section. For a more detailed discussion, the reader is referred to [187].

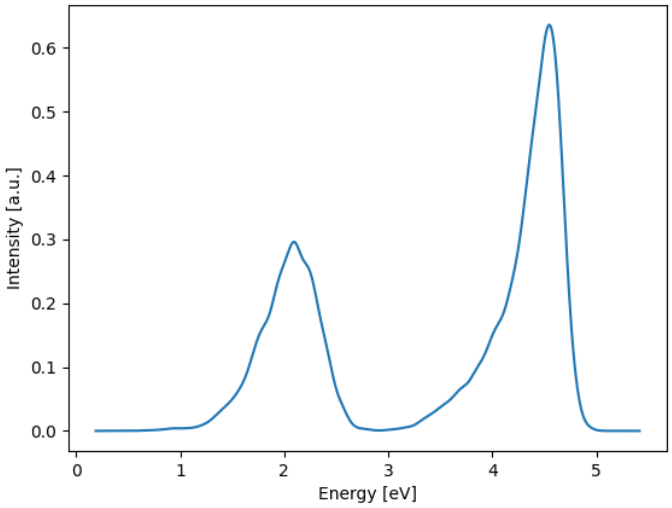

Figure 37: Simulated absorption spectrum of the $HzH_2\cdots(H_2O)_4$ complex. At each of the 1,500 phase-space points sampled from the Wigner distribution at 298K, the vertical excitation energies and oscillator strengths of the lowest nine electronic states were calculated. The envelope is obtained by convolution with a Gaussian of 0.05 eV FWHM.

The time evolution of the population probabilities of the adiabatic electronic states S_0-S_8 up to 150 fs is shown in Figure 38 (a). At t = 0 fs, the majority of the population is in the photoexcited S_7 and S_8 states. Within 10 fs the electronic population is distributed over lower-lying excited states. About 90% of trajectories encounter a conical intersection with the electronic ground-state within 100 fs of the simulation.
Using the excitation energy and the spatial extension of the occupied virtual orbital as criteria, the adiabatic states have been assigned to the categories „low-lying $\pi\pi^*$ states“, „$\pi\sigma^*$ states“, „high-lying $\pi\pi^*/n\pi^*$ states“ and electronic ground-state. The population evolution among these groups of electronic states is shown in Figure 38 (b). The vast majority of trajecotries start in high-lying $\pi\pi^*/n\pi^*$ states. The $\pi\sigma^*$ states begin to be populated around 5 fs and their populations reach a maximum of 45% at 18 fs. Around 20% of trajectories populate transiently low-lying $\pi\pi^*$ states. Encounters of trajectories with S_1-S_0 conical intersections occur after about 20 fs. The histogram of these S_1-S_0 conical intersection encounters is shown in Figure 38 (c).

6.3.3 Nonadiabatic Excited-State Dynamics of $HzH_2\cdots(H_2O)_4$ complexes

The time-dependent population probabilities of the adiabatic electronic states S_0-S_9 of the $HzH_2\cdots(H_2O)_4$ complex are shown in Figure 39 (top) over a time evolution of 100 fs. The initial

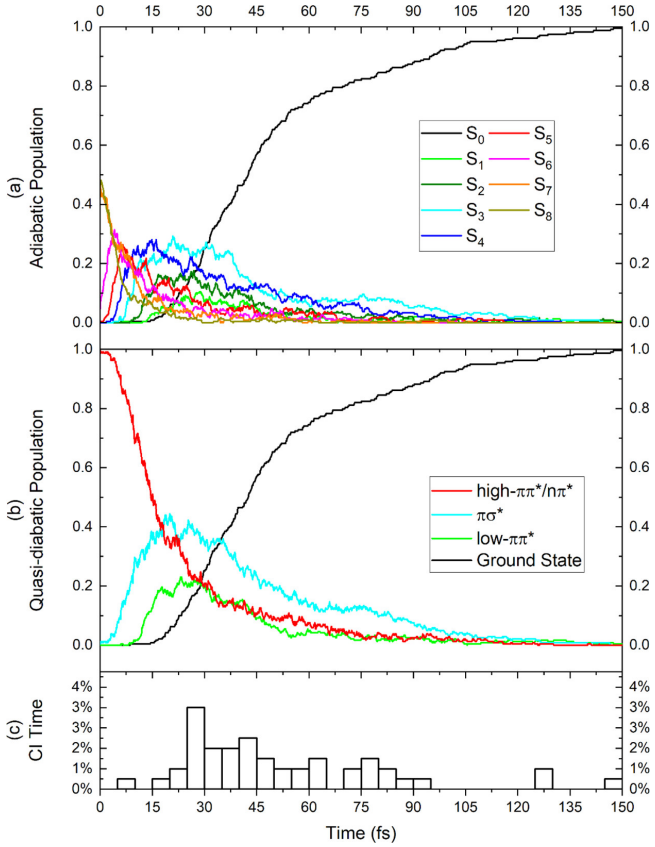

Figure 38: (a) Time evolution of the population of adiabatic electronic states in HzH_2. (b) Time evolution of the population of the quasidiabatic $\pi\sigma^*$ state and groups of locally excited states. The group of high-lying locally excited states is marked red, the $\pi\sigma^*$state blue, the S_1 state green, and the ground state black. (c) Histogram of encounters of trajectories in the $\pi\sigma^*$ state with an S_1-S_0 conical intersection, approximated by an energy gap of less than 0.2 eV. For all trajectories, the value of R_{OH} at the time of encounter of the conical intersection was larger than 1.4 Å. Adapted from [187].

conditions were selected as described in Section **6.2**. At t = 0 fs, the largest fractions of the population are in the S_9 and S_8 states which are the main absorbing states. Smaller fractions are in the S_7 and S_6 states. On a timescale of about 10 fs, the S_8 and S_9 adiabatic states depopulate via non-adiabatic transitions. An enlarged version of Figure 39 with focus on the first 10 fs is given in Figure A.6. The depopulation of the initially excited states gives rise to a distribution of populations of the lower adiabatic states. The transient population of the S_3 state (blue) is eye-catching. After about 15 fs it has the largest share of the population among the excited states. Over the 100 fs of the simulation, 90% of the trajectories encounter a S_1-S_0 energy gap which is lower than 0.1 eV.

Figure 39 (top) gives insight into the time evolution of the populations of the adiabatic states, but

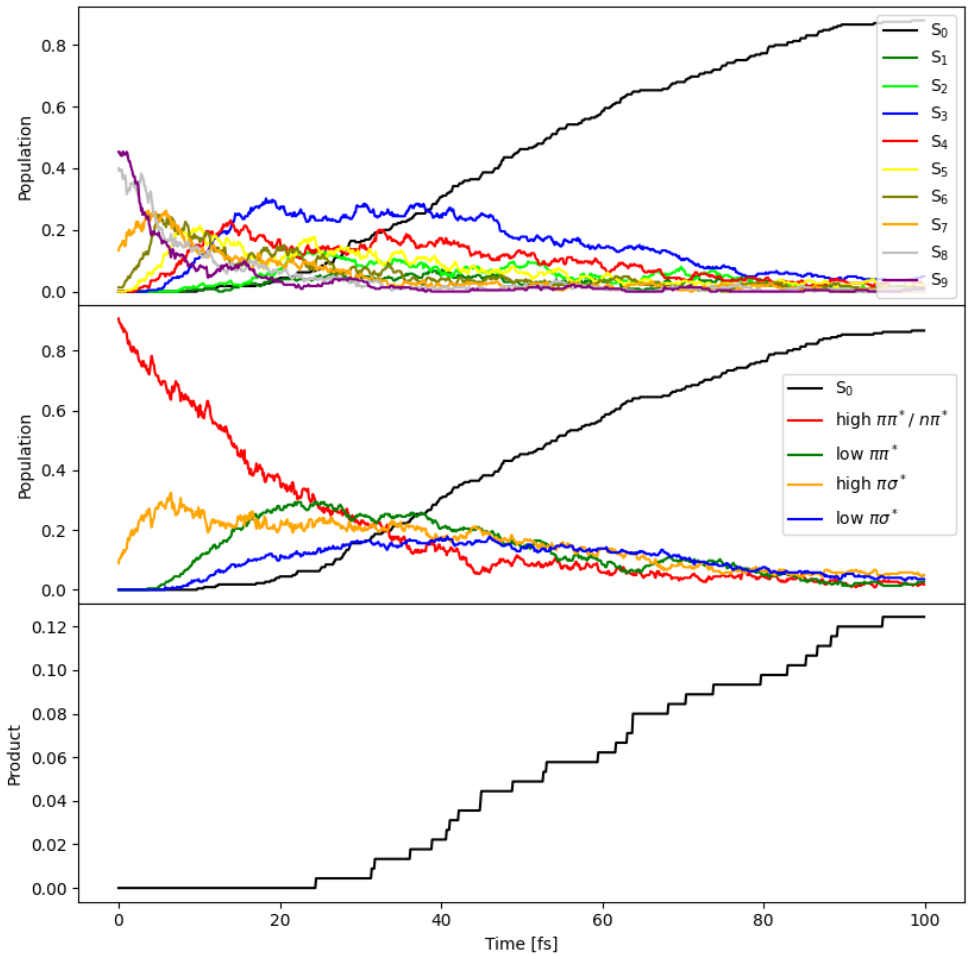

Figure 39: Top: Time evolution of the populations probabilities of the adiabatic electronic states of the $HzH_2\cdots(H_2O)_4$ complex. The color code is given in the legend. Middle: Time evolution of the population of quasi-diabatic states of the $HzH_2\cdots(H_2O)_4$ complex. The color code is given in the legend. Bottom: The cumulative reaction probability for H-atom transfer.

does not provide information about the electronic character of these states. For this purpose, the adiabatic states have been assigned to groups as explained in Section **6.2**. The population evolution of these quasi-diabatic states of the $HzH_2\cdots(H_2O)_4$ complex is shown in Figure 39 (middle). At t = 0 fs, 91% of trajectories populate a high-lying $^1\pi\pi^*$ or $^1n\pi^*$ state. 9% of the trajectories are attributed to high-lying $^1\pi\sigma^*$ states. Low-lying $^1\pi\sigma^*$ and $^1\pi\pi^*$ states are not populated. Over 40 fs, most of the population of high-lying $^1\pi\pi^*$ states is transferred first to high-lying $^1\pi\sigma^*$ states and from there to low-lying $^1\pi\pi^*$ and $^1\pi\sigma^*$ states. After an increase during the first 10 fs of the simulation, the population of high-lying $^1\pi\sigma^*$ states slowly decays until the end of the simulation. Low-lying $^1\pi\pi^*$ states are populated after around 4 fs. At t = 6 fs, low-lying $^1\pi\sigma^*$ states are also populated. After 17 fs, the high- and low-lying $^1\pi\pi^*$ have the largest share of the population of

the excited states until 33 fs and 45 fs, respectively. At t = 54 fs, both, high- and low-lying, $^1\pi\sigma^*$ states have the highest share of the population until the end of the simulation.

The fraction of $HzH\cdots H_3O(H_2O)_3$ product complexes formed at the moment of an encounter of a S_1-S_0 energy gap below 0.1 eV is shown in Figure 39 (bottom). The formation of H_3O at a conical intersection with the ground state exhibits a slow increase with time. After t = 25 fs the share of reactive trajectories increases in a near-linear fashion and reaches 13% at the end of the simulation.

While giving insights into the non-adiabatic population dynamics after photoexcitation of the $HzH_2\cdots(H_2O)_4$ complex, Figure 39 (top and middle) provide no structural information. For this purpose, dynamical maps of the trajectories with respect to the NO and OH distances have been constructed. The OH distance is the reporter of the formation of H_3O radicals. The NO distance represents the donor-acceptor distance of the PCET reaction. OH distances of 1.3 Å and below indicate the formation of an H_3O radical. These geometries will in the following be referred to as product region. Regions with an OH distance around 1.7 Å and a NO distance around 2.8 Å will be referred to as educt region.

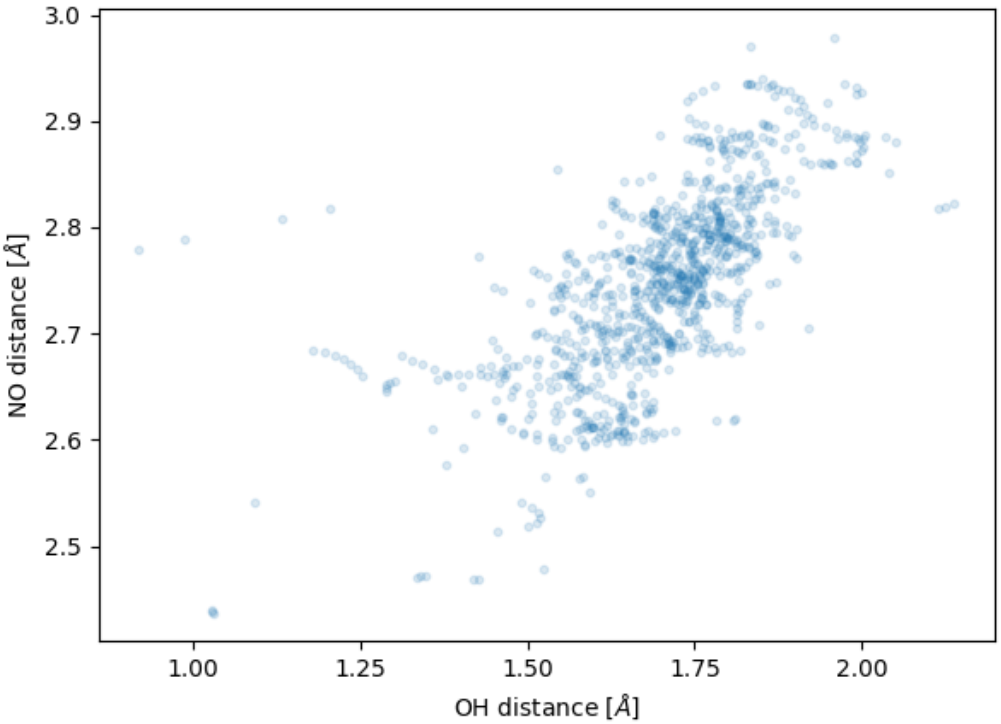

Figure 40: Dynamic map of the adiabatic S_9 state of the $HzH_2\cdots(H_2O)_4$ complex with respect to the NO and OH distances. Each point represents a geometry during the simulation.

The dynamic map of trajectories in the adiabatic S_9 state is shown in Figure 40. This state has the largest share of the population at t = 0 fs. Each blue point represents a geometry sampled in the S_9 state. Most of the encountered geometries in the S_9 state exhibit OH distances between 1.6 Å and 1.9 Å and NO distances between 2.7 Å and 2.9 Å and are therefore in the educt region. Apart from a couple of outliers, no geometries in the product area are encountered in the S_9 state.

The dynamic map of trajectories in the adiabatic S_3 state with respect to the NO and OH distances is shown in Figure 41. This adiabatic state is of interest due to its large share of the population between 10 fs and 50 fs as shown in Figure 39 (top). Due to the large fraction of trajectories in the

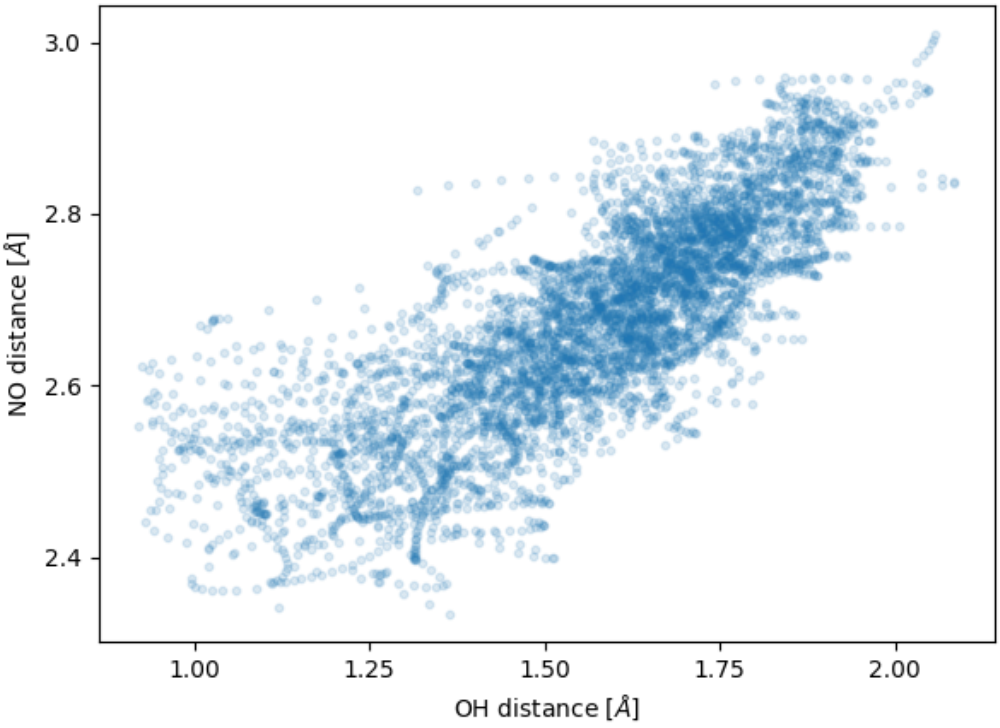

Figure 41: Dynamic map of the adiabatic S_3 state of the $HzH_2 \cdots (H_2O)_4$ complex with respect to the NO and OH distances. Each point represents a geometry during the simulation.

S_3 state over a long timespan, significantly more geometries were sampled than for the S_9 state. Unlike for the S_9 state, the dynamic map for the S_3 state exhibits geometries with OH distances from 1.0 Å to 2.0 Å and NO distances from 2.4 Å to 3.0 Å. Although the majority of geometries do not represent products, a significant portion of geometries are located in the product region.

The dynamic map of the S_1 state is shown in Figure 42. A significant fraction of the trajectories is encountered in the product region. In comparison with the dynamic map for the S_3 state (Fig-

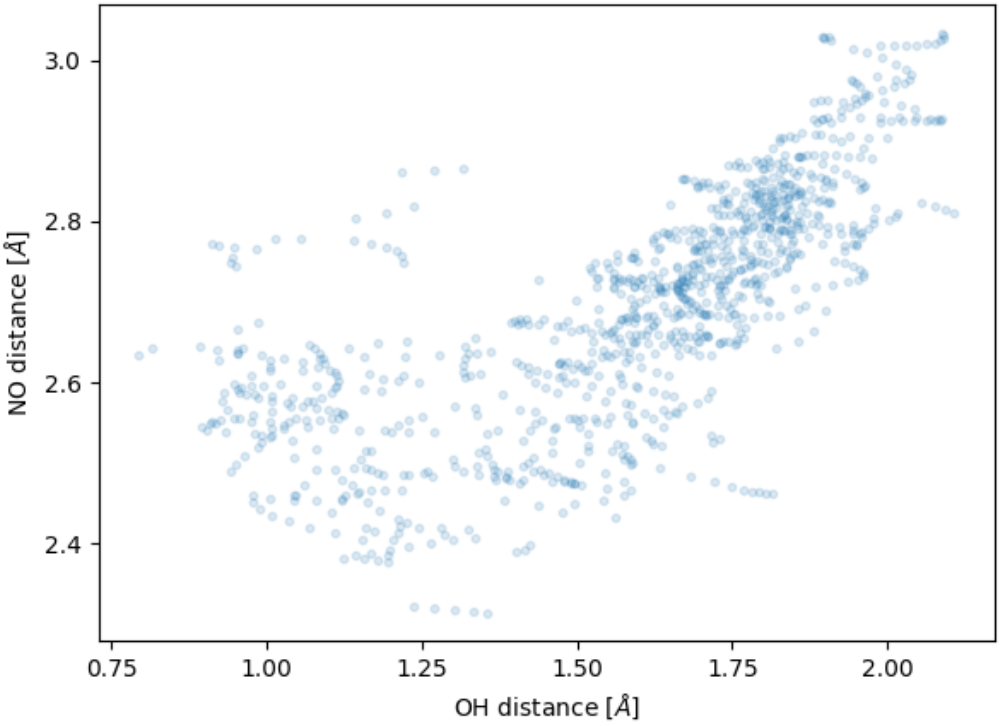

Figure 42: Dynamic map of the adiabatic S_1 state of the $HzH_2\cdots(H_2O)_4$ complex with respect to the NO and OH distances. Each point represents a geometry during the simulation.

ure 41), significantly less geometries are sampled. This is due to the fact that trajectories stay only briefly in the S_1 state.

In combination, the dynamical maps of the adiabatic states (Figure 40, Figure 41, Figure 42) provide a spatially resolved picture of the relaxation from the excitation to the S_9 state through the S_3 state to the S_1 state. The majority of geometries in the S_9 state are located in the educt region. After reaching the S_3 state (Figure 41), the trajectories sample significantly more geometries in the product region, while also being more spread out than in the dynamic map of the S_9 state (Figure 40).

The determination of an accurate quantum yield of the PCET reaction requires the use of multi-reference methods to correctly describe S_1-S_0 conical intersections. Since multi-reference methods pose considerable technical challenges in dynamics simulations and are computationally very expensive, such simulations are beyond the scope of this work. Therefore, only an approximate upper limit of the quantum yield of the PCET reaction can be given, which is 13%.

6.4 Discussion

State-of-the-art computational methods were employed to investigate the non-adiabatic nuclear dynamics of the photoinduced PCET reaction from HzH_2 to H_2O in the hydrogen-bonded $HzH_2\cdots(H_2O)_4$ cluster. The ADC(2) method and the LZSH algorithm were employed as robust and efficient computational protocols. The dynamics is initiated by photoexcitation at 4.54$\pm$0.05 eV and trajectories were propagated for 100 fs or until an S_1-S_0 energy gap lower than 0.1 eV is encountered. The estimated upper limit of 13% for the quantum yield of the PCET reaction can be expected to increase when the second excess H atom of HzH_2 is included in the dynamics. The addition of a larger water cluster would also have the consequence of exhibiting additional $^1\pi\sigma^*$ states below the absorbing $^1\pi\pi^*$ and $^1n\pi^*$ states. An extension of the size of the water cluster is expected to further elongate the lifetime of the lowest $^1\pi\sigma^*$ state. Substitution of the C-H bonds also may be a way to manipulate the quantum yield.

The results of this dynamics study can be related to the findings and conclusions of the static computational study of Section **4**. First, the prediction that $H_3O(H_2O)_3$ radicals can be generated from the HzH radical within a hydrogen-bonded $(H_2O)_4$ cluster has been confirmed. The assumption of the existence of a long lived CT state (the lowest $\pi\sigma^*$ state) also has been confirmed. In comparison with the H-atom photodetachment from HzH_2[187], the lowest $\pi\sigma^*$ stays populated for significantly longer time in the $HzH_2\cdots(H_2O)_4$ complex. This dynamics study explored the kinetics and the underlying mechanism of the reaction. The reaction is found to take place on a timescale of around 100 fs, as the majority (>90%) of the trajectories encounter an S_1-S_0 energy gap minimum within this time interval. The mechanism is illustrated by the dynamic maps which show the donor-acceptor distance (NO distance) and the transfer coordiante (OH distance) of the PCET reaction. It is seen that the formation of $H_3O(H_2O)_3$ clusters (decrease of the OH distance below 1.3 Å) goes hand in hand with a decrease of the donor-acceptor distance. The abstraction of the $H_3O(H_2O)_3$ cluster from the HzH radical (increase of the NO distance, OH distance stays below 1.3 Å) cannot be evaluated, because a conical intersection with the electronic ground-state would be encountered, which cannot be treated with the methods chosen for this study.

In the future, multi-reference methods should be applied to investigate the questions that were not answered in the static and dynamics studies of the present work.

7 Summary and Conclusion

In previous work of Domcke and coworkers, several possibilities of the photooxidation of water with organic photooxidants were explored with computational methods.[76, 188–191] In particular, it has been shown that the heptazine (Hz) molecule, which is one of the strongest known photooxidants in organic chemistry,[192] is able to abstract hydrogen atoms from water molecules upon excitation to the lowest bright $^1\pi\pi^*$ state, resulting in the formation of heptazinyl (HzH) and OH radicals.[73] This theoretical prediction was experimentally confirmed with a chemically and photochemically stable derivative of Hz, trianisole-heptatine (TAHz), by Schlenker and coworkers.[74] It has furthermore been shown by computational studies that photoexcitation of the HzH radical results in a rapid (nonstatistical) photodissociation reaction which recovers the Hz molecule and generates a free hydrogen radical.[73] The Pt-catalyzed recombination of the H-atoms to H_2 results in the evolution of molecular hydrogen, as observed in countless studies with polymeric carbon nitride (PCN) materials in recent years.[44, 45, 74]

The recombination of the photochemically generated free H-atom radicals to H_2 implies a considerable waste of energy. While the technology for the thermal reduction of CO_2 with H_2 to formic acid or methanol exists, these highly endothermic reactions require high temperatures and pressures and therefore are energy-intensive.[6–9] The direct light-driven reduction of CO_2 to liquid fuels, avoiding the intermediate formation of H_2, would therefore be of great interest for future energy conversion technologies. While the thermal (ground-state) reaction of HzH with CO_2 is sluggish due to a high energy barrier, photoexcitation of HzH may result in efficient transfer of an H-atom from HzH to CO_2, recovering the Hz molecule and yielding the hydroxyformyl (HOCO) radical as energy carrier. In this integrated concept of water oxidation and CO_2 reduction, the conversion of CO_2 to HOCO is purely driven by light without any input of thermal energy. The exploration of the detailed photochemical mechanisms by which HOCO radicals can directly be generated from water and carbon dioxide with the Hz molecule as photocatalyst has been the subject of the present work.

The direct photoinduced transfer of an H-atom from the HzH radical to CO_2 is described by Eq. 2 of the introduction, which is reproduced here for the convenience of the reader.

$$\mathrm{HzH} + \mathrm{CO_2} \xrightarrow{h\nu} \mathrm{Hz} + \mathrm{HOCO} \tag{2}$$

This reaction is an example of an excited-state proton-coupled electron transfer (PCET) reaction.[125] It is studied in the present work in the hydrogen-bonded $\mathrm{HzH}\cdots\mathrm{OCO}$ complex. In previous work, Ehrmaier *et al.* studied this type of PCET reaction in the hydrogen-bonded complex of the pyridinyl radical (PyH) with CO_2.[193] The drawback of the photocatalyst pyridine is that its

lowest absorption band is in the far UV. The much larger size of the Hz chromophore results in an absorption band close to the upper edge of the visible spectrum, which can further be lowered by suitable substituents.[78] In both $PyH\cdots CO_2$ and $HzH\cdots CO_2$ complexes, it is found that the ground-state reaction exhibits a high barrier ($\approx$ 2.0 eV), while the barrier of the PCET reaction in the $^2\pi\sigma^*$ excited state is either absent or very low. Photoexcitation thus converts a barrier-dominated reaction to an essentially barrierless reaction. The PE surfaces of the $HzH\cdots CO_2$ complex were characterized in the present work by the calculation of relaxed one-dimensional cuts and relaxed two-dimensional surfaces with multi-configuration multi-reference methods as described in Section **3**. On the other hand, conical intersections of the reactive PE surfaces with the PE surfaces of nonreactive electronic states exist along the PCET reaction path. The yield of the HOCO product is controlled by the nonadiabatic dynamics at these conical intersections. The open-shell character of the $HzH\cdots CO_2$ system represents a currently unsurmountable challenge for *ab initio* simulations of the nonadiabatic dynamics. The theoretical determination of the quantum yield of the photoinduced HzH + CO_2 reaction therefore remains an open problem.

The photocatalytic reduction of CO_2 with Hz-based PCNs and certain co-catalysts is an active area of research. Maeda and coworkers, for example, reported the formation of formic acid from CO_2 and water with a PCN catalyst and a ruthenium complex.[46] Lin *et al.* reported the reduction of CO_2 to CO with a PCN catalyst and a cobalt complex.[48] It is likely that the photochemical mechanisms discussed in the present work play a role in these experiments, but no spectroscopic or kinetic data are available and the role played by PCN and the co-catalysts in these experiments is unknown.

The second reaction mechanism explored in the present work with computational methods is the photoinduced and water-catalyzed transfer of an H-atom from the HzH radical to CO_2. This reaction mechanism is described by Eq. 3 and Eq. 4 of the introduction, which are reproduced here for the convenience of the reader.

$$HzH + (H_2O)_n \xrightarrow{h\nu} Hz + H_3O(H_2O)_{n-1} \tag{3}$$

$$H_3O(H_2O)_{n-1} + CO_2 \rightarrow HOCO + (H_2O)_n \tag{4}$$

In this scenario, the excess H-atom of HzH is first transferred in a photoinduced reaction to the aqueous environment, forming a so-called hydrated electron (Eq. 3). The aqueous environment is modelled by a finite water cluster in the present work. The $H_3O(H_2O)_n$ complex is a finite-size model of the hydrated electron in liquid water. As shown in earlier work by Sobolewski and Domcke, the hydrated H_3O radical exhibits the characteristic features of the hydrated electron in bulk water, such as the strong absorption at 720 nm, a finite lifetime ($\approx$ 1 μs) and an exception-

ally high reduction potential.[70, 194, 195] Due to its high reduction potential, the hydrated H_3O radical can reduce the CO_2 molecule to the HOCO radical in a ground-state reaction at ambient temperature.

The photoinduced generation of hydrated H_3O radicals in $HzH\cdots(H_2O)_n$ complexes has been studied by the calculation of minimum-energy paths and energy profiles as described in Section **4**. The essential result of this work is the prediction of a barrierless excited-state reaction path for the generation of the $H_3O(H_2O)_{n-1}$ product. While the photodetachment of the H-atom from the HzH radical requires the passing of three conical intersections along the reaction path, the reaction path for the formation of the H_3O radical is free from conical intersections, which is favourable for the quantum yield of this reaction. The dynamics of the photogeneration of hydrated H_3O radicals has been studied for the complex of doubly reduced Hz (HzH_2) with four water molecules, which is an electronic closed-shell system (Section **6**). While the formation of hydrated electrons via photodetachment from organic chromophores with acidic groups, such as pyrrole, phenol, indole or aniline, has been investigated since decades[130, 143–147] and is theoretically well understood,[148–154] the calculations of Section **4** are the first of their kind for hydrated electron formation from an open-shell precursor.

The exothermic reaction of hydrated H_3O radicals with CO_2 in the electronic ground state (Eq. 4) has been investigated in Section **5**. The mechanistic aspects of the transfer of an electron and a proton from $H_3O(H_2O)_n$ complexes to CO_2 were explored with zero, one and two hydration shells of the H_3O radical. While a quantitative estimate of the reaction barrier could not be given due to the incomplete sampling of cluster structures, the results indicate a rather low reaction barrier of the order of 0.1 eV (9.6 kJ/mol). For this reaction, a comparison of the computational results with experimental data is possible. Hamers and coworkers reported the reduction of CO_2 to CO by hydrated electrons which were generated by UV irradiation of diamond in liquid water. No kinetic information was obtained in these experiments. In a very different experiment, Beyer and coworkers investigated the reactivity of anionic water clusters, $(H_2O)_n^-$ (n=2-61), with CO_2 molecules in the gas phase with FT-ICR mass spectrometry.[175] The reported reaction enthalpy of -105$\pm$39 kJ/mol (-1.09 eV) is in excellent agreement with the results obtained in the present work, albeit $(H_2O)_n^-$ clusters are not exactly the same as $H_3O(H_2O)_n$ clusters. Very recently, Lisovskaya and Bartels determined the barrier for the reaction of hydrated electrons with CO_2 in liquid water as 15.9 kJ/mol (0.16 eV),[134] which is consistent with the present findings.

Our computational results suggest that the direct reduction of CO_2 by photoexcited HzH radicals (Eq. 2) as well as the water-catalyzed photoreaction via intermediate hydrated H_3O radicals (Eqs. 3, 4) are feasible reactions. For the thermal reaction of Eq. 4, we find good agreement of our computational results with experimental data. For the photoreaction of the HzH radical with CO_2

and H_2O, on the other hand, no experimental data exist so far, since radicals are transient species in photocatalysis.
In this work, only the first step in the reduction of CO_2 to clean fuels, namely the activation of CO_2 to the HOCO radical, has been investigated. This step is the most challenging step in the conversion of CO_2 to fuels, since a double bond of the extremely stable CO_2 molecule has to be broken. The HOCO radical can be further reduced by sequential H-atom transfer reactions to formic acid, formaldehyde or methanol. These subsequent reactions are thermoneutral or exothermic and mostly barrierless[26] and therefore are less challenging.

References

(1) Styring, P.; Quadrelli, E. A.; Armstrong, K., *Carbon dioxide utilisation: closing the carbon cycle*; Elsevier: 2014; Vol. 1.

(2) Aresta, M.; Karimi, I.; Kawi, S., *An economy based on carbon dioxide and water*; Springer: 2019.

(3) Meylan, F. D.; Moreau, V.; Erkman, S. *Journal of CO_2 Utilization* **2015**, *12*, 101–108.

(4) Arakawa, H.; Aresta, M.; Armor, J. N.; Barteau, M. A.; Beckman, E. J.; Bell, A. T.; Bercaw, J. E.; Creutz, C.; Dinjus, E.; Dixon, D. A., et al. *Chemical Reviews* **2001**, *101*, 953–996.

(5) Sordakis, K.; Tang, C.; Vogt, L. K.; Junge, H.; Dyson, P. J.; Beller, M.; Laurenczy, G. *Chemical Reviews* **2018**, *118*, 372–433.

(6) Wang, W.-H.; Himeda, Y.; Muckerman, J. T.; Manbeck, G. F.; Fujita, E. *Chemical Reviews* **2015**, *115*, 12936–12973.

(7) Álvarez, A.; Bansode, A.; Urakawa, A.; Bavykina, A. V.; Wezendonk, T. A.; Makkee, M.; Gascon, J.; Kapteijn, F. *Chemical Reviews* **2017**, *117*, 9804–9838.

(8) Ye, R.-P.; Ding, J.; Gong, W.; Argyle, M. D.; Zhong, Q.; Wang, Y.; Russell, C. K.; Xu, Z.; Russell, A. G.; Li, Q., et al. *Nature Communications* **2019**, *10*, 1–15.

(9) Newsome, D. S. *Catalysis Reviews Science and Engineering* **1980**, *21*, 275–318.

(10) Anderson, R. B., *Fischer-Tropsch Synthesis*, 1984.

(11) Fisher, I. A.; Bell, A. T. *Journal of Catalysis* **1997**, *172*, 222–237.

(12) Hutschka, F.; Dedieu, A.; Eichberger, M.; Fornika, R.; Leitner, W. *Journal of the American Chemical Society* **1997**, *119*, 4432–4443.

(13) Kusama, H.; Okabe, K.; Sayama, K.; Arakawa, H. *Catalysis Today* **1996**, *28*, 261–266.

(14) Jessop, P. G.; Hsiao, Y.; Ikariya, T.; Noyori, R. *Journal of the American Chemical Society* **1996**, *118*, 344–355.

(15) Eggins, B. R.; McNeill, J. *Journal of Electroanalytical Chemistry and Interfacial Electrochemistry* **1983**, *148*, 17–24.

(16) Gattrell, M.; Gupta, N.; Co, A. *Journal of Electroanalytical Chemistry* **2006**, *594*, 1–19.

(17) Whipple, D. T.; Kenis, P. J. *The Journal of Physical Chemistry Letters* **2010**, *1*, 3451–3458.

(18) Hori, Y.; Kikuchi, K.; Murata, A.; Suzuki, S. *Chemistry Letters* **1986**, *15*, 897–898.

(19) Beley, M.; Collin, J. P.; Ruppert, R.; Sauvage, J. P. *Journal of the American Chemical Society* **1986**, *108*, 7461–7467.

(20) Bernatis, P. R.; Miedaner, A.; Haltiwanger, R. C.; DuBois, D. L. *Organometallics* **1994**, *13*, 4835–4843.

(21) Sanchez-Sanchez, C.; Montiel, V.; Tryk, D.; Aldaz, A.; Fujishima, A. *Pure and Applied Chemistry* **2001**, *73*, 1917–1927.

(22) Azuma, M.; Hashimoto, K.; Hiramoto, M.; Watanabe, M.; Sakata, T. *Journal of the Electrochemical Society* **1990**, *137*, 1772.

(23) Keith, J. A.; Carter, E. A. *The Journal of Physical Chemistry Letters* **2013**, *4*, 4058–4063.

(24) Keith, J. A.; Carter, E. A. *Chemical Science* **2013**, *4*, 1490–1496.

(25) Keith, J. A.; Carter, E. A. *Journal of the American Chemical Society* **2012**, *134*, 7580–7583.

(26) Barton Cole, E.; Lakkaraju, P. S.; Rampulla, D. M.; Morris, A. J.; Abelev, E.; Bocarsly, A. B. *Journal of the American Chemical Society* **2010**, *132*, 11539–11551.

(27) Morris, A. J.; McGibbon, R. T.; Bocarsly, A. B. *ChemSusChem* **2011**, *4*, 191–196.

(28) Yan, Y.; Zeitler, E. L.; Gu, J.; Hu, Y.; Bocarsly, A. B. *Journal of the American Chemical Society* **2013**, *135*, 14020–14023.

(29) Ertem, M. Z.; Konezny, S. J.; Araujo, C. M.; Batista, V. S. *The Journal of Physical Chemistry Letters* **2013**, *4*, 745–748.

(30) Yan, Y.; Gu, J.; Bocarsly, A. B., et al. *Aerosol and Air Quality Research* **2014**, *14*, 515–521.

(31) Yang, J. Y.; Kerr, T. A.; Wang, X. S.; Barlow, J. M. *Journal of the American Chemical Society* **2020**, *142*, 19438–19445.

(32) Weerasooriya, R. B.; Gesiorski, J. L.; Alherz, A.; Ilic, S.; Hargenrader, G. N.; Musgrave, C. B.; Glusac, K. D. *The Journal of Physical Chemistry Letters* **2021**, *12*, 2306–2311.

(33) Morris, A. J.; Meyer, G. J.; Fujita, E. *Accounts of Chemical Research* **2009**, *42*, 1983–1994.

(34) Mikkelsen, M.; Jørgensen, M.; Krebs, F. C. *Energy & Environmental Science* **2010**, *3*, 43–81.

(35) Takeda, H.; Ishitani, O. *Coordination Chemistry Reviews* **2010**, *254*, 346–354.

(36) Roy, S. C.; Varghese, O. K.; Paulose, M.; Grimes, C. A. *ACS Nano* **2010**, *4*, 1259–1278.

(37) Appel, A. M.; Bercaw, J. E.; Bocarsly, A. B.; Dobbek, H.; DuBois, D. L.; Dupuis, M.; Ferry, J. G.; Fujita, E.; Hille, R.; Kenis, P. J., et al. *Chemical Reviews* **2013**, *113*, 6621–6658.

(38) Habisreutinger, S. N.; Schmidt-Mende, L.; Stolarczyk, J. K. *Angewandte Chemie International Edition* **2013**, *52*, 7372–7408.

(39) Yamazaki, Y.; Takeda, H.; Ishitani, O. *Journal of Photochemistry and Photobiology C: Photochemistry Reviews* **2015**, *25*, 106–137.

(40) Li, X.; Yu, J.; Jaroniec, M.; Chen, X. *Chemical Reviews* **2019**, *119*, 3962–4179.

(41) Thompson, W. A.; Sanchez Fernandez, E.; Maroto-Valer, M. M. *ACS Sustainable Chemistry & Engineering* **2020**, *8*, 4677–4692.

(42) Halmann, M. *Nature* **1978**, *275*, 115–116.

(43) Inoue, T.; Fujishima, A.; Konishi, S.; Honda, K. *Nature* **1979**, *277*, 637–638.

(44) Wang, X.; Maeda, K.; Thomas, A.; Takanabe, K.; Xin, G.; Carlsson, J. M.; Domen, K.; Antonietti, M. *Nature materials* **2009**, *8*, 76–80.

(45) Wang, Y.; Wang, X.; Antonietti, M. *Angewandte Chemie International Edition* **2012**, *51*, 68–89.

(46) Maeda, K.; Sekizawa, K.; Ishitani, O. *Chemical Communications* **2013**, *49*, 10127–10129.

(47) Kuriki, R.; Sekizawa, K.; Ishitani, O.; Maeda, K. *Angewandte Chemie International Edition* **2015**, *54*, 2406–2409.

(48) Lin, J.; Pan, Z.; Wang, X. *ACS Sustainable Chemistry & Engineering* **2014**, *2*, 353–358.

(49) Kuriki, R.; Matsunaga, H.; Nakashima, T.; Wada, K.; Yamakata, A.; Ishitani, O.; Maeda, K. *Journal of the American Chemical Society* **2016**, *138*, 5159–5170.

(50) Walsh, J. J.; Jiang, C.; Tang, J.; Cowan, A. J. *Physical Chemistry Chemical Physics* **2016**, *18*, 24825–24829.

(51) Zhang, L.; Zhu, D.; Nathanson, G. M.; Hamers, R. J. *Angewandte Chemie International Edition* **2014**, *53*, 9746–9750.

(52) Hart, E. J.; Boag, J. W. *Journal of the American Chemical Society* **1962**, *84*, 4090–4095.

(53) Hart, E. J.; Anbar, M., *Hydrated Electron*; Wiley: 1970.

(54) Buxton, G. V.; Greenstock, C. L.; Helman, W. P.; Ross, A. B. *Journal of Physical and Chemical Reference Data* **1988**, *17*, 513–886.

(55) Abel, B.; Buck, U.; Sobolewski, A. L.; Domcke, W. *Physical Chemistry Chemical Physics* **2012**, *14*, 22–34.

(56) Herbert, J. M.; Coons, M. P. *Annual Review of Physical Chemistry* **2017**, *68*, 447–472.

(57) Herbert, J. M. *Physical Chemistry Chemical Physics* **2019**, *21*, 20538–20565.

(58) Feng, D.-F.; Kevan, L. *Chemical Reviews* **1980**, *80*, 1–20.

(59) Rossky, P. J.; Schnitker, J. *The Journal of Physical Chemistry* **1988**, *92*, 4277–4285.

(60) Larsen, R. E.; Glover, W. J.; Schwartz, B. J. *Science* **2010**, *329*, 65–69.

(61) Herbert, J. M.; Jacobson, L. D. *The Journal of Physical Chemistry A* **2011**, *115*, 14470–14483.

(62) Ludwig, R.; Paschek, D. *ChemPhysChem* **2011**, *12*, 75–77.

(63) Turi, L.; Rossky, P. J. *Chemical Reviews* **2012**, *112*, PMID: 22954423, 5641–5674.

(64) Uhlig, F.; Marsalek, O.; Jungwirth, P. *The Journal of Physical Chemistry Letters* **2012**, *3*, 3071–3075.

(65) Casey, J. R.; Kahros, A.; Schwartz, B. J. *The Journal of Physical Chemistry B* **2013**, *117*, 14173–14182.

(66) Wilhelm, J.; VandeVondele, J.; Rybkin, V. V. *Angewandte Chemie International Edition* **2019**, *58*, 3890–3893.

(67) Dasgupta, S.; Rana, B.; Herbert, J. M. *The Journal of Physical Chemistry B* **2019**, *123*, 8074–8085.

(68) Hameka, H.; Robinson, G.; Marsden, C. *Journal of Physical Chemistry* **1987**, *91*, 3150–3157.

(69) Tuttle Jr., T. R.; Golden, S. *The Journal of Physical Chemistry* **1991**, *95*, 5725–5736.

(70) Sobolewski, A. L.; Domcke, W. *Physical Chemistry Chemical Physics* **2002**, *4*, 4–10.

(71) Uhlig, F.; Marsalek, O.; Jungwirth, P. *Physical Chemistry Chemical Physics* **2011**, *13*, 14003–14009.

(72) Svoboda, V.; Michiels, R.; LaForge, A. C.; Stienkemeier, F.; Slavíček, P.; Wörner, H. J. *Science Advances* **2020**, *6*.

(73) Ehrmaier, J.; Karsili, T. N. V.; Sobolewski, A. L.; Domcke, W. *The Journal of Physical Chemistry A* **2017**, *121*, 4754–4764.

(74) Rabe, E. J.; Corp, K. L.; Sobolewski, A. L.; Domcke, W.; Schlenker, C. W. *The Journal of Physical Chemistry Letters* **2018**, *9*, 6257–6261.

(75) Hwang, D.; Wrigley, L. M.; Lee, M.; Sobolewski, A. L.; Domcke, W.; Schlenker, C. W. *to be published* **2022**.

(76) Liu, X.; Sobolewski, A. L.; Borrelli, R.; Domcke, W. *Physical Chemistry Chemical Physics* **2013**, *15*, 5957–5966.

(77) Huang, X.; Aranguren, J.-P.; Ehrmaier, J.; Noble, J. A.; Xie, W.; Sobolewski, A. L.; Dedonder-Lardeux, C.; Jouvet, C.; Domcke, W. *Physical Chemistry Chemical Physics* **2020**, *22*, 12502–12514.

(78) Ehrmaier, J.; Huang, X.; Rabe, E. J.; Corp, K. L.; Schlenker, C. W.; Sobolewski, A. L.; Domcke, W. *The Journal of Physical Chemistry A* **2020**, *124*, 3698–3710.

(79) Diamond, L. W.; Akinfiev, N. N. *Fluid Phase Equilibria* **2003**, *208*, 265–290.

(80) Hartree, D. R. *Mathematical Proceedings of the Cambridge Philosophical Society* **1928**, *24*, 111–132.

(81) Fock, V. *Zeitschrift für Physik* **1930**, *61*, 126–148.

(82) Hartree, D. R.; Hartree, W. *Proceedings of the Royal Society of London. Series A - Mathematical and Physical Sciences* **1935**, *150*, 9–33.

(83) Szabo, A.; Ostlund, N. S., *Modern quantum chemistry: Introduction to Advanced Electronic Structure Theory*; Courier Corporation: 2012.

(84) Koopmans, T. *Physica* **1934**, *1*, 104–113.

(85) Roothaan, C. C. J. *Rev. Mod. Phys.* **1951**, *23*, 69–89.

(86) Hall, G. *Proceedings of the Royal Society of London. Series A. Mathematical and Physical Sciences* **1951**, *205*, 541–552.

(87) Pople, J. A.; Nesbet, R. K. *The Journal of Chemical Physics* **1954**, *22*, 571–572.

(88) Brillouin, L., *Les champs 'self-consistents' de Hartree et de Fock*; 159; Paris: 1934.

(89) Jensen, F., *Introduction to Computational Chemistry*; John Wiley & Sons: 2017.

(90) Binkley, J.; Pople, J. *International Journal of Quantum Chemistry* **1975**, *9*, 229–236.

(91) Schirmer, J. *Physical Review A* **1982**, *26*, 2395.

(92) Danovich, D. *Wiley Interdisciplinary Reviews: Computational Molecular Science* **2011**, *1*, 377–387.

(93) Schirmer, J. *Physical Review A* **1991**, *43*, 4647.

(94) Knippenberg, S.; Rehn, D.; Wormit, M.; Starcke, J.; Rusakova, I.; Trofimov, A.; Dreuw, A. *The Journal of Chemical Physics* **2012**, *136*, 064107.

(95) Roos, B. O. In *Advances in Chemical Physics*; John Wiley & Sons, Ltd: 1987, pp 399–445.

(96) Helgaker, T.; Jorgensen, P.; Olsen, J., *Molecular Electronic-Structure Theory*; John Wiley & Sons: 2014.

(97) Davydov, A. S., *Quantum Mechanics: International Series in Natural Philosophy*; Elsevier: 2013; Vol. 1.

(98) Born, M.; Oppenheimer, R. *Annalen der Physik* **1927**, *389*, 457–484.

(99) Quapp, W. In *The Reaction Path in Chemistry: Current Approaches and Perspectives*; Springer: 1995, pp 95–107.

(100) Barbatti, M. *Wiley Interdisciplinary Reviews: Computational Molecular Science* **2011**, *1*, 620–633.

(101) Truhlar, D. G.; Gordon, M. S. *Science* **1990**, *249*, 491–498.

(102) Born, M.; Huang, K. *Oxford University Press* **1954**.

(103) Domcke, W.; Yarkony, D.; Köppel, H., *Conical intersections: Electronic Structure, Dynamics & Spectroscopy*; World Scientific: 2004; Vol. 15.

(104) Pacher, T.; Cederbaum, L.; Köppel, H. *Advances in Chemical Physics* **1993**, *84*, 293–392.

(105) Ballhausen, C. J.; Hansen, A. E. *Annual Review of Physical Chemistry* **1972**, *23*, 15–38.

(106) Köppel, H.; Domcke, W.; Cederbaum, L. S. *Advances in Chemical Physics* **1984**, 59–246.

(107) Domcke, W.; Yarkony, D. R.; Köppel, H., *Conical Intersections: Theory, Computation and Experiment*; World Scientific: 2011; Vol. 17.

(108) Nakamura, H., *Nonadiabatic Transition: Concepts, Basic Theories and Applications*; World Scientific: 2012.

(109) Yarkony, D. R. *Chemical Reviews* **2012**, *112*, 481–498.

(110) Domcke, W.; Yarkony, D. R. *Annual Review of Physical Chemistry* **2012**, *63*, 325–352.

(111) Xie, W.; Sapunar, M.; Došlić, N.; Sala, M.; Domcke, W. *The Journal of Chemical Physics* **2019**, *150*, 154119.

(112) Crespo-Otero, R.; Barbatti, M. *Chemical Reviews* **2018**, *118*, 7026–7068.

(113) Meyer, H.-D.; Gatti, F.; Worth, G. A., *Multidimensional Quantum Dynamics: MCTDH Theory and Applications*; John Wiley & Sons: 2009.

(114) Martinez, T. J.; Levine, R. D. *The Journal of Chemical Physics* **1996**, *105*, 6334–6341.

(115) Ben-Nun, M.; Martínez, T. J. *Advances in Chemical Physics* **2002**, *121*, 439–512.

(116) Mignolet, B.; Curchod, B. F. *The Journal of Chemical Physics* **2018**, *148*, 134110.

(117) Tully, J. C. *The Journal of Chemical Physics* **1990**, *93*, 1061–1071.

(118) Belyaev, A. K.; Lebedev, O. V. *Physical Review A* **2011**, *84*, 014701.

(119) Wu, H.-Z.; Bandaru, S.; Huang, X.-L.; Liu, J.; Li, L.-L.; Wang, Z. *Physical Chemistry Chemical Physics* **2019**, *21*, 1514–1520.

(120) Andersson, K.; Malmqvist, P.-Å.; Roos, B. O. *The Journal of Chemical Physics* **1992**, *96*, 1218–1226.

(121) Dunning Jr., T. H. *The Journal of chemical physics* **1989**, *90*, 1007–1023.

(122) Fdez. Galván, I.; Vacher, M.; Alavi, A.; Angeli, C.; Aquilante, F.; Autschbach, J.; Bao, J. J.; Bokarev, S. I.; Bogdanov, N. A.; Carlson, R. K., et al. *Journal of Chemical Theory and Computation* **2019**, *15*, 5925–5964.

(123) Sommerfeld, T.; Meyer, H.-D.; Cederbaum, L. S. *Physical Chemistry Chemical Physics* **2004**, *6*, 42–45.

(124) Janik, I.; Tripathi, G. *The Journal of Chemical Physics* **2016**, *144*, 154307.

(125) Weinberg, D. R.; Gagliardi, C. J.; Hull, J. F.; Murphy, C. F.; Kent, C. A.; Westlake, B. C.; Paul, A.; Ess, D. H.; McCafferty, D. G.; Meyer, T. J. *Chemical Reviews* **2012**, *112*, 4016–4093.

(126) Hayashi, T.; Mukamel, S. *The Journal of Physical Chemistry A* **2003**, *107*, 9113–9131.

(127) Sobolewski, A. L.; Domcke, W.; Dedonder-Lardeux, C.; Jouvet, C. *Physical Chemistry Chemical Physics* **2002**, *4*, 1093–1100.

(128) Ashfold, M.; Cronin, B.; Devine, A.; Dixon, R.; Nix, M. *Science* **2006**, *312*, 1637–1640.

(129) Ashfold, M. N.; King, G. A.; Murdock, D.; Nix, M. G.; Oliver, T. A.; Sage, A. G. *Physical Chemistry Chemical Physics* **2010**, *12*, 1218–1238.

(130) Roberts, G. M.; Stavros, V. G. *Chemical Science* **2014**, *5*, 1698–1722.

(131) Pios, S.; Huang, X.; Domcke, W. *ChemPhotoChem* **2021**, *5*, 680–690.

(132) Neta, P.; Huie, R. E.; Ross, A. B. *Journal of Physical and Chemical Reference Data* **1988**, *17*, 1027–1284.

(133) Zhang, L.; Hamers, R. J. *Diamond and Related Materials* **2017**, *78*, 24–30.

(134) Lisovskaya, A.; Bartels, D. M. *Radiation Physics and Chemistry* **2019**, *158*, 61–63.

(135) Pios, S.; Domcke, W. *The Journal of Physical Chemistry A* **2022**.

(136) Hosmane, R. S.; Rossman, M. A.; Leonard, N. J. *Journal of the American Chemical Society* **1982**, *104*, 5497–5499.

(137) Leupin, W.; Wirz, J. *Journal of the American Chemical Society* **1980**, *102*, 6068–6075.

(138) Roos, B. O. *Accounts of Chemical Research* **1999**, *32*, 137–144.

(139) Ghigo, G.; Roos, B. O.; Malmqvist, P.-Å. *Chemical Physics Letters* **2004**, *396*, 142–149.

(140) TURBOMOLE V6.3.1 2007, a development of University of Karlsruhe and Forschungszentrum Karlsruhe GmbH, 1989-2007, TURBOMOLE GmbH, since 2007; available from http://www.turbomole.com.

(141) Barone, V.; Cossi, M. *The Journal of Physical Chemistry A* **1998**, *102*, 1995–2001.

(142) Cossi, M.; Rega, N.; Scalmani, G.; Barone, V. *The Journal of Chemical Physics* **2001**, *114*, 5691–5701.

(143) Wei, J.; Kuczmann, A.; Riedel, J.; Renth, F.; Temps, F. *Physical Chemistry Chemical Physics* **2003**, *5*, 315–320.

(144) Tseng, C.-M.; Lee, Y. T.; Ni, C.-K. *The Journal of Chemical Physics* **2004**, *121*, 2459–2461.

(145) Cronin, B.; Nix, M. G.; Qadiri, R. H.; Ashfold, M. N. *Physical Chemistry Chemical Physics* **2004**, *6*, 5031–5041.

(146) Nix, M.; Devine, A.; Cronin, B.; Ashfold, M. *Physical Chemistry Chemical Physics* **2006**, *8*, 2610–2618.

(147) Nix, M. G.; Devine, A. L.; Cronin, B.; Dixon, R. N.; Ashfold, M. N. *The Journal of Chemical Physics* **2006**, *125*, 133318.

(148) Lan, Z.; Domcke, W.; Vallet, V.; Sobolewski, A. L.; Mahapatra, S. *The Journal of Chemical Physics* **2005**, *122*, 224315.

(149) Vallet, V.; Lan, Z.; Mahapatra, S.; Sobolewski, A. L.; Domcke, W. *The Journal of Chemical Physics* **2005**, *123*, 144307.

(150) An, H.; Baeck, K. K. *The Journal of Physical Chemistry A* **2011**, *115*, 13309–13315.

(151) Faraji, S.; Vazdar, M.; Reddy, V. S.; Eckert-Maksic, M.; Lischka, H.; Köppel, H. *The Journal of Chemical Physics* **2011**, *135*, 154310.

(152) Xie, C.; Ma, J.; Zhu, X.; Yarkony, D. R.; Xie, D.; Guo, H. *Journal of the American Chemical Society* **2016**, *138*, 7828–7831.

(153) Picconi, D.; Grebenshchikov, S. Y. *The Journal of Chemical Physics* **2018**, *148*, 104104.

(154) Xie, C.; Zhao, B.; Malbon, C. L.; Yarkony, D. R.; Xie, D.; Guo, H. *The Journal of Physical Chemistry Letters* **2019**, *11*, 191–198.

(155) Barbatti, M.; Vazdar, M.; Aquino, A. J.; Eckert-Maksić, M.; Lischka, H. *The Journal of Chemical Physics* **2006**, *125*, 164323.

(156) Barbatti, M.; Pittner, J.; Pederzoli, M.; Werner, U.; Mitrić, R.; Bonačić-Koutecký, V.; Lischka, H. *Chemical Physics* **2010**, *375*, 26–34.

(157) Saita, K.; Nix, M. G.; Shalashilin, D. V. *Physical Chemistry Chemical Physics* **2013**, *15*, 16227–16235.

(158) Yang, K. R.; Xu, X.; Zheng, J.; Truhlar, D. G. *Chemical Science* **2014**, *5*, 4661–4680.

(159) Sapunar, M.; Ponzi, A.; Chaiwongwattana, S.; Mališ, M.; Prlj, A.; Decleva, P.; Došlić, N. *Physical Chemistry Chemical Physics* **2015**, *17*, 19012–19020.

(160) Heindl, M.; González, L. *Computational and Theoretical Chemistry* **2019**, *1155*, 38–46.

(161) Gregoire, G.; Dedonder-Lardeux, C.; Jouvet, C.; Martrenchard, S.; Solgadi, D. *The Journal of Physical Chemistry A* **2001**, *105*, 5971–5976.

(162) Rubio-Lago, L.; Amaral, G.; Oldani, A. N.; Rodríguez, J.; González, M.; Pino, G. A.; Bañares, L. *Physical Chemistry Chemical Physics* **2011**, *13*, 1082–1091.

(163) Miyazaki, M.; Washio, N.; Fujii, M. *Chemical Physics* **2018**, *515*, 580–585.

(164) Ishiuchi, S.-i.; Kamizori, J.; Tsuji, N.; Sakai, M.; Miyazaki, M.; Dedonder, C.; Jouvet, C.; Fujii, M. *Physical Chemistry Chemical Physics* **2020**, *22*, 5740–5748.

(165) Syage, J. A. *The Journal of Physical Chemistry* **1995**, *99*, 5772–5786.

(166) David, O.; Dedonder-Lardeux, C.; Jouvet, C. *International Reviews in Physical Chemistry* **2002**, *21*, 499–523.

(167) Sobolewski, A. L.; Domcke, W. *Chemical Physics Letters* **1999**, *315*, 293–298.

(168) Sobolewski, A. L.; Domcke, W. *Chemical Physics Letters* **2000**, *329*, 130–137.

(169) Sobolewski, A. L.; Domcke, W. *The Journal of Physical Chemistry A* **2001**, *105*, 9275–9283.

(170) Bent, D.; Hayon, E. *Journal of the American Chemical Society* **1975**, *97*, 2606–2612.

(171) Bent, D.; Hayon, E. *Journal of the American Chemical Society* **1975**, *97*, 2599–2606.

(172) Ehrmaier, J.; Picconi, D.; Karsili, T. N.; Domcke, W. *The Journal of Chemical Physics* **2017**, *146*, 124304.

(173) Rybkin, V. V. *The Journal of Physical Chemistry B* **2020**, *124*, 10435–10441.

(174) Liu, P.; Zhao, J.; Liu, J.; Zhang, M.; Bu, Y. *The Journal of Chemical Physics* **2014**, *140*, 044318.

(175) Akhgarnusch, A.; Tang, W. K.; Zhang, H.; Siu, C.-K.; Beyer, M. K. *Physical Chemistry Chemical Physics* **2016**, *18*, 23528–23537.

(176) Møller, C.; Plesset, M. S. *Physical Review* **1934**, *46*, 618.

(177) Trofimov, A.; Schirmer, J. *Journal of Physics B: Atomic, Molecular and Optical Physics* **1995**, *28*, 2299.

(178) Dreuw, A.; Wormit, M. *Wiley Interdisciplinary Reviews: Computational Molecular Science* **2015**, *5*, 82–95.

(179) Steinmann, S. N.; Piemontesi, C.; Delachat, A.; Corminboeuf, C. *Journal of Chemical Theory and Computation* **2012**, *8*, 1629–1640.

(180) TURBOMOLE V7.4 2017, a development of University of Karlsruhe and Forschungszentrum Karlsruhe GmbH, 1989-2007, TURBOMOLE GmbH, since 2007;
available from http://www.turbomole.com.

(181) Hättig, C.; Weigend, F. *The Journal of Chemical Physics* **2000**, *113*, 5154–5161.

(182) Crespo-Otero, R.; Barbatti, M. In *Marco Antonio Chaer Nascimento*; Springer: 2014, pp 89–102.

(183) Hillery, M.; O'Connell, R. F.; Scully, M. O.; Wigner, E. P. *Physics Reports* **1984**, *106*, 121–167.

(184) Barbatti, M.; Ruckenbauer, M.; Plasser, F.; Pittner, J.; Granucci, G.; Persico, M.; Lischka, H. *Wiley Interdisciplinary Reviews: Computational Molecular Science* **2014**, *4*, 26–33.

(185) Belyaev, A. K.; Lasser, C.; Trigila, G. *The Journal of Chemical Physics* **2014**, *140*, 224108.

(186) Belyaev, A. K.; Domcke, W.; Lasser, C.; Trigila, G. *The Journal of Chemical Physics* **2015**, *142*, 104307.

(187) Huang, X.; Domcke, W. *The Journal of Physical Chemistry A* **2021**, *125*, 9917–9931.

(188) Liu, X.; Sobolewski, A. L.; Domcke, W. *The Journal of Physical Chemistry A* **2014**, *118*, 7788–7795.

(189) Liu, X.; Karsili, T. N.; Sobolewski, A. L.; Domcke, W. *The Journal of Physical Chemistry B* **2015**, *119*, 10664–10672.

(190) Liu, X.; Karsili, T. N.; Sobolewski, A. L.; Domcke, W. *Chemical Physics* **2016**, *464*, 78–85.

(191) Bi, J.; Fang, W.; Li, L.; Wang, J.; Liang, S.; He, Y.; Liu, M.; Wu, L. *Macromolecular Rapid Communications* **2015**, *36*, 1799–1805.

(192) Audebert, P.; Kroke, E.; Posern, C.; Lee, S.-H. *Chemical Reviews* **2021**, *121*, 2515–2544.

(193) Ehrmaier, J.; Sobolewski, A. L.; Domcke, W. *The Journal of Physical Chemistry A* **2019**, *123*, 3678–3684.

(194) Sobolewski, A. L.; Domcke, W. *The Journal of Physical Chemistry A* **2002**, *106*, 4158–4167.

(195) Sobolewski, A. L.; Domcke, W. *Physical Chemistry Chemical Physics* **2007**, *9*, 3818–3829.

8 Appendix

A.1 HzH$\cdots$OCO - The *cis* HOCO Product

The calculations described in the main text for the *trans* conformer of HOCO (Figure 3 (a)) were repeated for the *cis* conformer shown in Figure 3 (b). The ground-state equilibrium geometry of the *cis* conformer of Hz$\cdots$HOCO determined with the constraint of collinear C, N and O atoms (Figure 1) is shown in Figure 3 (b). The hydrogen bond length of 2.11 Å indicates a relatively weak hydrogen bond. The two-dimensional relaxed scan of the PE surface of the electronic state

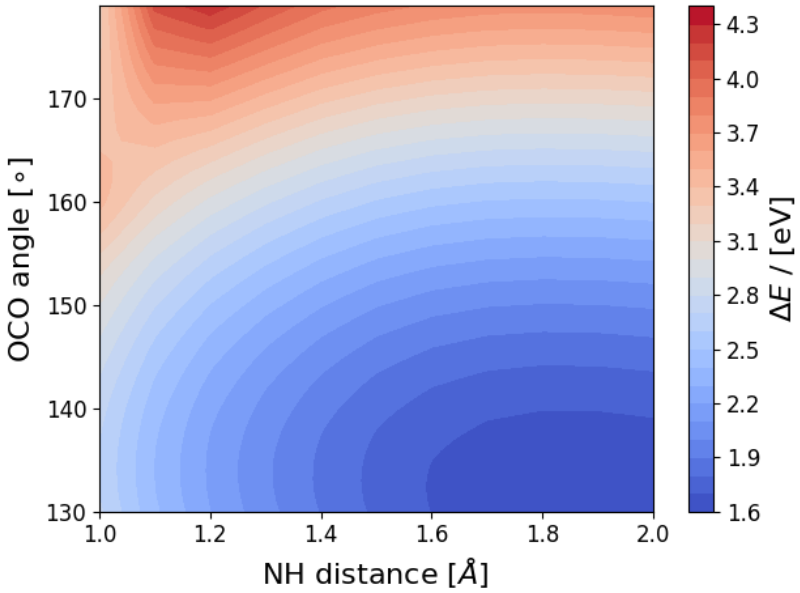

Figure A.1: Two-dimensional relaxed PE surface of the $^2\pi\sigma^*$ excited state of the HzH$\cdots$OCO complex calculated at the CASSCF//CASPT2 level. The reaction coordinates are the NH distance of the HzH fragment and the OCO bending angle of CO_2. The color code gives the energy (in eV) relative to the energy minimum of the electronic ground-state of the HzH$\cdots$OCO complex.

of A′ symmetry ($^2\pi\sigma^*$ excited state at the educt geometry, ground state at the product geometry) calculated at the CASSCF//CASPT2 level as function of the OCO-angle and the NH-distance is shown in Figure A.1. The educt geometry (Figure 2 (a)) corresponds to the upper left corner. The bottom right area corresponds to the product geometry shown in Figure 3 (b). The cut along the NH distance for an OCO angle of 180° (upper rim of Figure A.1) reveals a barrier near an NH distance of 1.2 Å. The cut along the OCO angle for an NH distance of 1.0 Å (left rim of Figure A.1) exhibits a low barrier near an OCO angle of 162.5°. For OCO-angles larger than about 165°, the CO_2 molecule remains neutral and protonation is energetically unfavorable. For OCO-

angles below 165°, the electron in the σ^* orbital is spontaneously transferred from HzH to the CO_2 molecule forming the CO_2^- anion. Protonation of this anion is energetically favorable, which causes the deep well around the OCO angle of 130° and NH distance of 1.9 Å, see Figure A.1. It can be seen in Figure A.1 that a low-barrier reaction path starting at the upper left corner exists which initially involves bending for fixed NH distance, followed by concerted bending and NH stretching towards the deep minimum at the product geometry. The saddle point along this path is located at an OCO angle of 165° and an NH distance of 1.05 Å. The barrier along the minimum-energy reaction path is estimated as 0.1 eV from Figure A.1.

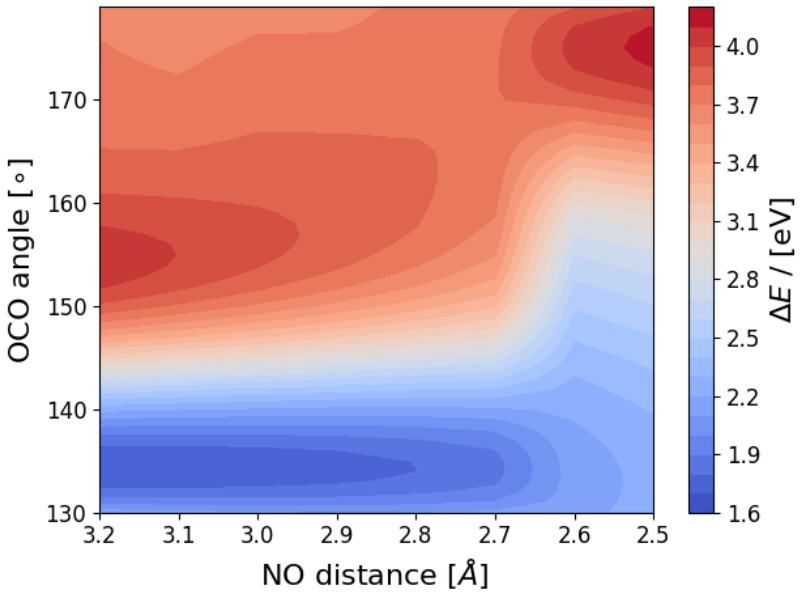

Figure A.2: Two-dimensional relaxed PE surface of the ${}^2\pi\sigma^*$ excited state of the HzH$\cdots$OCO complex calculated at the CASSCF//CASPT2 level. The reaction coordinates are the NO distance of the HzH$\cdots$OCO and the OCO bending angle of CO_2. The color code gives the energy (in eV) relative to the energy minimum of the electronic ground-state of the HzH$\cdots$OCO complex.

The two-dimensional relaxed PE surface of the A′ state of the HzH$\cdots$OCO complex as function of the OCO angle and the NO distance, calculated at the CASSCF//CASPT2 level, is displayed in Figure A.2. The top left corner corresponds to the educt geometry (Figure 2 (a)). The stretched well in the bottom region of Figure A.2 corresponds to the product geometry shown in Figure 3 (b). The energy profile of the cut along the upper rim (linear CO_2) is initially flat and then steeply rising, revealing the weak attraction of linear CO_2 by HzH along the NO distance, followed by strong repulsion at short distances. The energy profile of the cut along the left rim (fixed NO distance of 3.2 Å) exhibits a pronounced barrier near an OCO angle of 155°. The two-dimensional

surface shows that a low-barrier reaction path exists which initially involves mainly a decrease of the NO distance, followed by bending for nearly fixed NO distance. The saddle point corresponds to an OCO-angle of 168° and an NO-distance of 2.76 Å. The height of the barrier along this path is estimated as 0.1 eV. Figure A.2 reveals that the contraction of the donor-acceptor distance plays an important role for the initiation of the reaction, as is typical for PCET reactions. Along

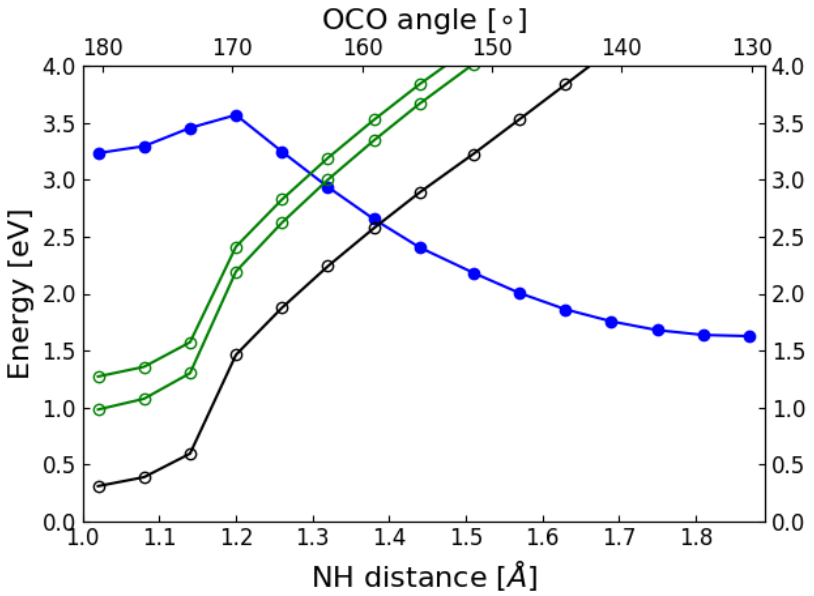

Figure A.3: Energy profiles of the electronic ground-state of the HzH···OCO complex (black), of four $^2\pi\pi^*$ excited states (green), and of the $^2\pi\sigma^*$ excited state (blue) along a linear cut from the ground-state equilibrium geometry of the HzH···OCO educt complex to the equilibrium geometry of the *cis* Hz···HOCO product complex.

the reaction path from the educt geometry to the product geometry, the energy profile of the $^2\pi\sigma^*$ state intersects the energy profiles of two low-lying $^2\pi\pi^*$ states and the energy profile of the D_0 ground state of the HzH···OCO complex. This is illustrated by Figure A.3, which shows the energy profiles along a linear cut from the upper left corner to the lower right corner of Figure A.1. The variation of the OCO angle and the NH distance along this cut is shown at the top and the bottom of Figure A.3, respectively. The left hand side of Figure A.3 corresponds to the educt configuration (linear CO_2 which is hydrogen-bonded to HzH), the right hand side to the product configuration (*cis* HOCO radical which is hydrogen-bonded to Hz). The filled blue circles represent the energy of the $^2\pi\sigma^*$ state of HzH···OCO, the energy of which was minimized for the construction of the relaxed surface of Figure A.1. The green open circles represent the energy of the two low-lying $^2\pi\pi^*$ states and the black open circles represent the energy of the ground state of the HzH···OCO complex at the same geometries. It is seen that the energy of the $^2\pi\sigma^*$

excited state of the HzH$\cdots$OCO complex is diabatically connected to the electronic ground-state of the Hz$\cdots$HOCO complex. The $^2\pi\sigma^*$ energy profile exhibits a maximum about 0.34 eV above the energy of the educt near an NH distance of 1.2 Å. The energies of the $^2\pi\pi^*$ states as well as of the ground state increase in a nearly parallel manner. The steep increase of these energies near an NH distance of 1.2 Å is caused by a strong decrease of the NO distance (and implicitly the OH distance).

Qualitatively, the results for the *cis* conformer of the Hz$\cdots$HOCO complex are similar to those of the *trans* conformer. Apart from small topographical differences of the PE surfaces, the difference between these two reaction products is the energy at the product geometry. The *trans* conformer of the Hz$\cdots$HOCO complex 0.2 eV lower in energy than the *cis* conformer.

A.2 The $H_3O(H_2O)_6\cdots CO_2$ Complex - Second Geometry

The educt (a) and product (b) geometry of the $H_3O(H_2O)_6\cdots CO_2$ cluster with their respective SOMO is shown in Figure A.4. The educt geoemtry is remeniscent of the $H_3O(H_2O)_6$ cluster shown in Figure 23 (c) with a CO_2 added to the side. It is important to note the location of the SOMO relative to the CO_2. Unlike for the systems discussed in Section **5** is is spatially separated from the CO_2 by the $H_3O(H_2O)_6$ cluster. It is fractionally more stable than its counter-part in Section **5.3.4** by around 0.02 eV. The hydrogen bond length at the educt geometry is 2.81 Å and is therefore weak.
At the product geometry the O atoms of the water molecules once again resemble a slightly distorted cube. The HOCO radical in its *trans* conformer is formed allowing for the formation of an additional hydorgen bond between the SOMO and a water molecule. The hydrogen bond from the HOCO to the $(H_2O)_7$ cluster is 1.65 Å and therefore significantly stronger than at the educt geometry.
The one-dimensional relaxed scan of the $H_3O(H_2O)_6\cdots CO_2$ cluster along the OH distance (a) and OCO bending angle at a fixed OH distance of 1.3 Å (b) at UMP2//UMP2 level is shown in Figure A.5. Along the OH distance the PE surface is flat until 2.00 Å are reached. Afterwards the energy increases with decreasing OH distance until 1.3 Å. At smaller OH distances the electron is transferred from the $H_3O(H_2O)_6$ cluster to the CO_2 molecule, causing it to bend an significantly decrease the energy as was already observed for the smaller clusters in Section **5**. The local minimum is at an OH distance of 1.0 Å and 1.07 eV below the energy of the educt geometry.
To verify that the drop in energy in Figure A.5 (a) is caused by the OCO bending angle, a second one-dimension relaxed scan with respect to the OCO bending angle has been constructed and is shown in Figure A.5 (b). This scan exhibits a local maximum around an OCO bending angle of 170°. The apparent barrier for this reaction can therefore be estimated to be around 0.85 eV. For OCO bending angles smaller than 170° the energy decreases in an orderly fashion with the local minimum being at an OCO angle of 135°.

Overall the apparent barrier of 0.85 eV is very high in comparison to the results for the $H_3O(H_2O)_3\cdots CO_2$ cluster and even the $H_3O\cdots CO_2$ system. A reasonable explanation for this is the relative location of the SOMO to the CO_2 molecule. In the previous systems the proximity of both allowed for the transfer of the electron by „squeezing“ the cluster while this does not work for this educt geometry.

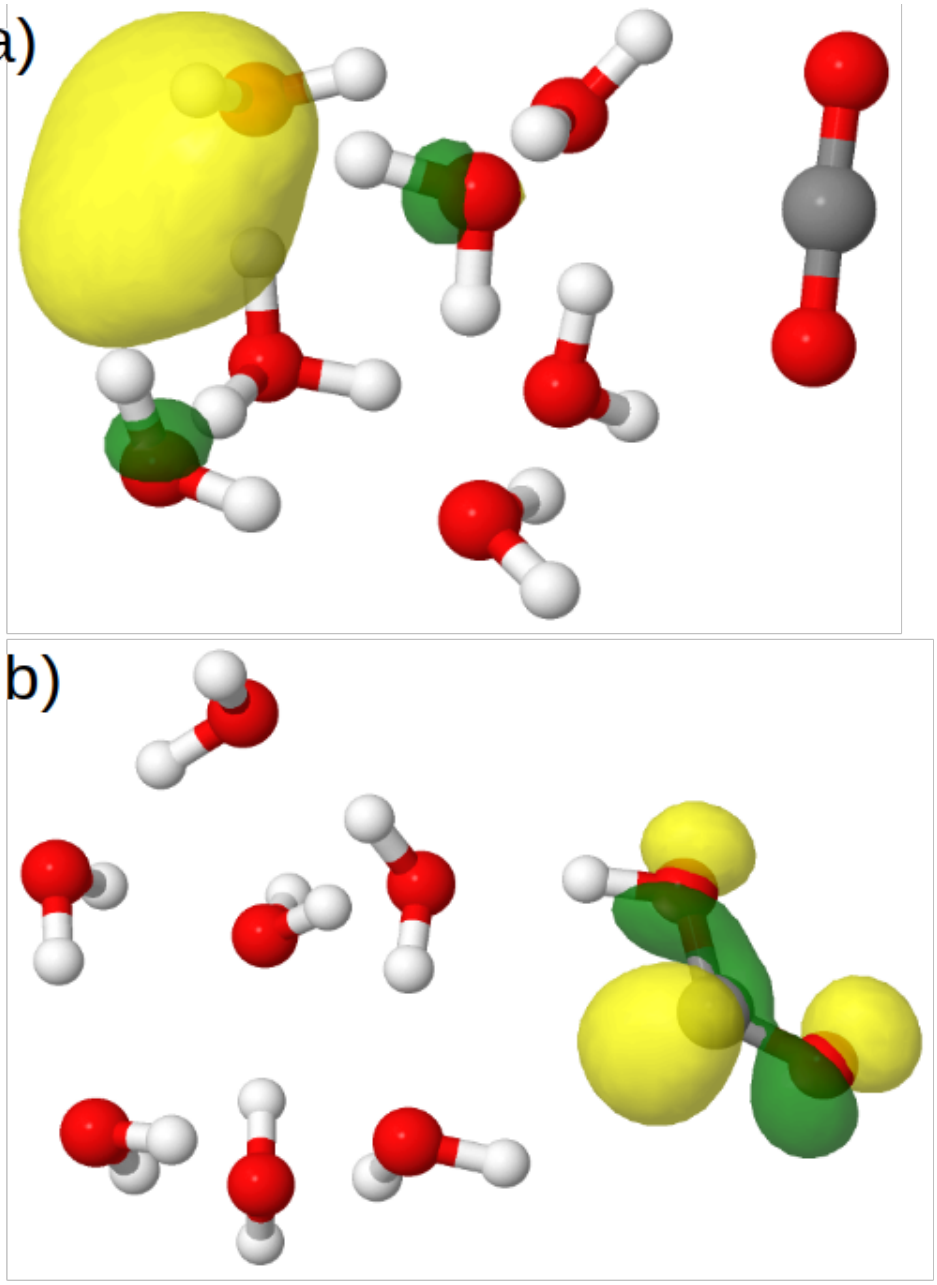

Figure A.4: Educt (a) and product (b) geometry of the $H_3O(H_2O)_6 \cdots CO_2$ cluster with their respective SOMO.

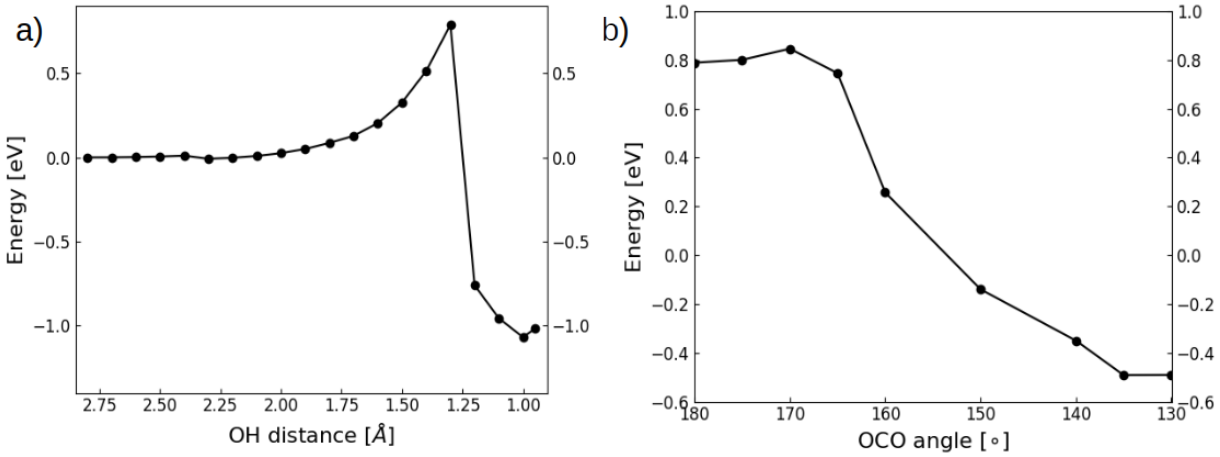

Figure A.5: Energy profile of the relaxed scan of the $H_3O(H_2O)_6 \cdots CO_2$ complex at UMP2//UMP2 with respect to the OH distance (a) and the OCO bending angle at a fixed OH distance of 1.3 Å (b). The energy is given relative to the educt geometry.

A.3 Time evolution of the populations probabilities of the adiabatic electronic states of the $HzH_2 \cdots (H_2O)_4$ complex for the first 10 fs.

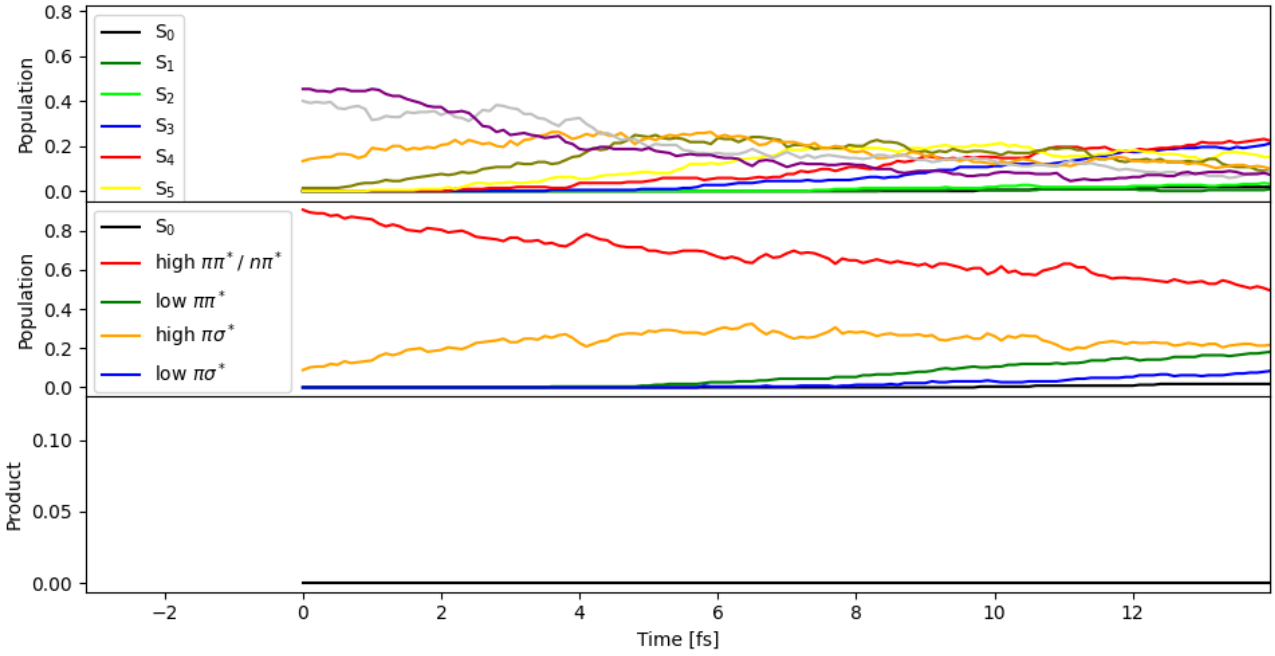

Figure A.6: Top: Time evolution of the populations probabilities of the adiabatic electronic states of the $HzH_2\cdots(H_2O)_4$ complex for the first 10 fs. The color code is given in the legend. Middle: Time evolution of the population of quasi-diabatic states of the $HzH_2\cdots(H_2O)_4$ complex for the first 10 fs. The color code is given in the legend. Bottom: The cumulative reaction probability for H-atom transfer for the first 10 fs.